Large Scale Computation of the Rotating Stall in a Pump-Turbine using an Overset Finite Element Large Eddy Simulation Numerical Code

THÈSE N^O 6183 (2014)

ÉCOLE POLYTECHNIQUE FÉDÉRALE DE LAUSANNE

POUR L'OBTENTION DU GRADE DE DOCTEUR ÈS SCIENCES

PAR

Olivier PACOT

acceptée sur proposition du jury:

Prof. I. Botsis, président du jury
Prof. F. Avellan, Prof. C. Kato, directeurs de thèse
Dr J.-B. Houdeline, rapporteur
Prof. O. Métais, rapporteur
Prof. L. Villard, rapporteur

EPFL

ÉCOLE POLYTECHNIQUE
FÉDÉRALE DE LAUSANNE

Suisse
2014

If you can't fly then run,
if you can't run then walk,
if you can't walk then crawl,
but whatever you do,
you have to keep moving forward.

Martin Luther King Jr.

Acknowledgements

First and most important, I would like to express my sincere gratitude to my thesis directors Prof. François Avellan and Prof. Chisachi Kato for their motivation, enthusiasm, patience and immense knowledge. Their guidance helped me all along my research work and the writing of the thesis.

Besides my advisors, I would like to thank the rest of my thesis committee: Prof. Ioannis Botsis, Dr. Jean-Bernard Houdeline, Prof. Olivier Métais and Prof. Laurent Villard, for their encouragement, insightful comments, and hard questions.

For some people, the choice to do a PhD is made quite early into their studies. For others, it is the result of personal experiences, meetings and opportunities. In my case, the latter is true, firstly thanks to coniglietto (Steven) who introduced me to the laboratory, located in the downtown of Lausanne. Secondly, I should thank Cécile who introduced me to the Large Eddy Simulation and both of them motivated me to go further. Even if during the last year I wondered several time why I decided to do a PhD, now I can be nothing else than grateful, because it gave me the opportunity to meet many interesting people, to learn a lot of exciting things and finally to explore a part of the world which was totally unknown to me!

In view of the importance of computing ressources in my numerical research, and the many trips between Geneva and Tokyo, I would like to thank Philippe Cerrutti and Isabelle for their availability and constant support with my technical and administrative needs.

My research wouldn't have been possible without all the work done by my predecessor Olivier Braun. I would like to thank him for all his support and the advise he gave me in order for me to pursue the investigation under the best conditions.

A PhD is also a long adventure shared among many people and not only between PhD students. At LMH we have the opportunity to interact with other groups as the mechanical group at the workshop, the design group or the test bed group. All together, it was great to share raclettes and bbq parties, weekends at Ovronnaz and volley during the EPFL championship. A special thank to Viktor, for making me suffer during our jogging and to Max for helping me with all my big problems: shoes, door,... and for the nice time we had during our weekly *apéro* on Friday evenings.

The length of the list of former and present PhD students is quite frightening. I hope I will not forget anybody! Olivier: you were the first to leave and I won't forget the nice samba show after your public presentation. Philippe Ausoni: you showed me the effect that the writing has on PhD students and I won't forget the wonderful and hilarious lunch together, during that period. Ruch: even if you are a snowboarder and a windsurfer (nobody is perfect héhé) our ski trip by night and kite/windsurf sessions were very nice. Sebounet, Cécile and your two wonderful daughters: Your are the best family and a model for me!! Thanks for all the time we spent together and I'm already looking forward to our next kitesurf and ski sessions. What about Brazil 2015? Vlad: how to forget our enjoyable discussions drinking Munich's beer after our nice experience of the German highway. Coniglieto: the list is too long! From our Thursday nights during the master to now, passing by our flat in Renens, there is too much to say and most cannot be written here. Let's remember what good viewers we were during the winter Olympic games 2010... Ebrahim: I won't forget your impressive knowledge and thanks to introduce to me the SPH method. Vessaz: for sure I will miss your incredible local stories you told us. Good luck with your remarkable SPH videos. Big body our preferred scapegoat: For sure being from the low-Wallis is not easy..., but thanks to your constant and appreciable good mood. Tthieuma: too much to say but I will remember how you loved the "glouglouglou" at the ABL lecture! Recla the king: you were not supposed to finish your PhD that early! But thanks for our telemark trips! It was awesome, so next time in Hokkaido. Arthur: be the force with you. You recalled me some stuff of my past. Good luck and do better than me!! Dr. Tinguely: still now I'm amazed by the Marc during the day and the Marc by night. Don't change! Boby: your name is always present at the lab. We try to maintain your spirit and to honor the beer as you do. Finally, I would like to make a special thank to the known Herr Müller (HM)! Thanks for all the support during these past months and for welcoming me at your place once I'm back in Lausanne. For sure, our trips to Okinawa and Hokkaido while tasting nice whiskies will stay in my mind for long.

Two years ago, I went to Tokyo for the first time to work at the laboratory of Prof. Kato. I would like to express my gratitude to Yamade-san, Guo-san, Nishimura-san, Suzuki-san, Tsubuki-san, Takekoshi-san and all the others students for their help and their warm welcome. They were always available and ready to help me either with my research, or with my acclimation to the lifestyle in Japan. These two years were wonderful! Besides the lab, I should thank my dinner mates Adrian, Aldo and Mike who supported me especially these past months when I was writing. Also, a special thank to Nathalie and Pauline who helped me when I had no place to go and to Pierre, Hélène, Nico, Mehul, Alia, Koko-san, Jean-Pierre and Albert for all the nice activities we had together. Again thanks to HM, Tthieuma, Mr. Tinguely, Max and the M&M's for coming to visit me. It was great to see you there.

During my stay in Tokyo, several people arrived at the laboratory to do a PhD or a postDoc. I would like then to wish you Elena, Simon, Keita, Quentin, Philippe Kobel and Loïc all the best with your research. I hope you will appreciate the lifestyle of the lab and of Lausanne. Good luck!

Finally, I would like to thank my family, who always supported me and encouraged me to go further.

Résumé

Suite aux nouveaux besoins énergétiques et économiques, de plus en plus de pompe-turbines sont utilisées dans les centrales de pompage turbinage, utilisées pour garantir la stabilité du réseau électrique d'une part et pour stocker l'excédent d'énergie électrique d'autre part. Pour cela, les pompe-turbines doivent pouvoir être manoeuvrées efficacement dans une large plage de fonctionnement, c'est-à-dire pouvoir oeuvrer sans problème significatif à des points de fonctionnement éloignés de celui pour lequel elles sont conçues. Cependant, lorsque l'on s'éloigne trop du point de fonctionnement optimal, l'écoulement peut devenir instable ce qui engendre du bruit, des vibrations et une chute du rendement. Un exemple est l'utilisation d'une pompe-turbine en mode pompe à charge partielle où une instabilité du nom *décollement tournant* apparaît. Dans ce cas de figure, l'écoulement passant autour de certaines directrices décolle et perturbe l'écoulement du diffuseur. L'endroit où l'écoulement décolle change avec le temps, ce qui engendre une perturbation locale et temporelle de l'écoulement, d'où la propagation de cette perturbation d'une directrice à sa voisine.

L'étude de ce phénomène à ce jour est restée très limitée due à sa localisation dans la machine qui est difficilement accessible. Pour une approche expérimentale, il faut trouver des solutions pour s'affranchir des différentes parois qui obstruent la visualisation de l'écoulement. Pour une approche numérique, il faut en trouver de nouvelles, car l'approche RANS - traditionnellement utilisée - a montré ses limites. Une alternative numérique serait l'approche par la simulation des grandes échelles (SGE) qui est connue pour sa capacité à calculer précisément de tels écoulements, mais dont les besoins en puissance de calcul ont été trop contraignants dans le passé, pour que cette approche soit utilisée. Aujourd'hui, suite au développement constant des supercalculateurs, la puissance de calcul accessible offre de nouvelles perspectives pour étudier des phénomènes physiques par l'approche SGE. L'objectif de ce travail de recherche est donc de démontrer que le décollement tournant peut être reproduit précisément par une simulation des grandes échelles, afin d'élargir les connaissances de ce phénomène. Pour cela, la pompe-turbine HYDRODYNA a été choisie et l'écoulement calculé est celui en mode pompe à charge partielle, φ=0.026 (76% BEP). En effet, une étude expérimentale a démontré la présence du décollement tournant pour ce point de fonctionnement.

La complexité dans la simulation des grandes échelles réside principalement dans la génération du domaine de calcul que l'on appelle maillage. Ce maillage est prédominant, car il gouverne la séparation entre les grandes et les petites structures présentes dans l'écoulement. Sachant que l'approche SGE calcule explicitement les grandes structures et modélise l'influence des petites, il est donc essentiel que le maillage soit suffisamment fin afin de capturer toutes les structures principales de l'écoulement pour assurer un résultat de bonne précision. Dans le cadre de cette recherche, une étude de faisabilité

a démontré que le décollement tournant peut être simulé en utilisant un maillage de 600 milliards d'éléments pour un nombre de Reynolds identique à l'étude expérimentale, ce qui n'est pas envisageable. Cependant, si le nombre de Reynolds est réduit d'un facteur 5 comparé à l'expérimental (Re/5), le maillage nécessaire se réduit à 7 milliards d'éléments, ce qui devient acceptable. De la même façon, si le nombre de Reynolds est réduit d'un facteur 25, le maillage nécessaire se réduit à 80 millions d'éléments (Re/25). En conséquence, un maillage de 85 millions d'éléments a été généré en vue d'initialiser l'écoulement et pour cela, le supercalculateur PRIMEHPC-FX10 de l'université de Tokyo - qui possède un peu moins de 80,000 coeurs de calcul - a été utilisé. Concernant le software, le code FrontFlow/blue, développé par la même institution, a été sélectionné. Ce code est parallélisé ce qui a permis d'effectuer les calculs en utilisant 2,048 coeurs de calcul, soit le calcul d'un tour de roue en moins de 7 heures. Par ailleurs, ce code est basé sur la méthode des éléments finis pour l'intégration des équations régissant le mouvement des fluides Newtoniens (équations de Navier-Stokes), il utilise le modèle de Smagorinsky dynamique pour fermer le système d'équations propre à l'approche SGE et il utilise une méthode de recouvrement des maillages comme interface entre la partie tournante et les parties fixes.

L'initialisation de l'écoulement pour le cas Re/5 avec le maillage de 85 millions d'éléments a montré que le phénomène est déjà capturé après le calcul de 10 tours de roue. Ainsi, le décollement de l'écoulement en 4 régions du diffuseur, appelé ultérieurement cellule de décollement, est observable, correspondant à ce qui a été rapporté expérimentalement. De plus, l'énergie Ψ calculée est proche de la valeur expérimentale, soit 3.35% supérieure. Cependant, la vitesse de propagation des cellules est environ 60% plus lente que celle escomptée, ce qui s'explique par le manque de résolution de l'écoulement étant donné qu'un maillage de 7 milliards d'éléments est nécessaire pour un tel nombre de Reynolds.

Le calcul de l'écoulement pour le cas Re/25, avec le même maillage de 85 millions d'éléments, a permis de capturer précisément le phénomène du décollement tournant dans la pompe-turbine. L'énergie calculée Ψ est 0.36% plus élevée que la valeur expérimentale, le nombre de cellules de décollement est identique et la vitesse de propagation des cellules de décollement est seulement 3.4% plus lente que la valeur expérimentale. Ceci confirme la qualité du calcul et démontre la possibilité de traiter des problèmes de type industriel par cette approche.

En utilisant l'écoulement obtenu dans le cas Re/25, le mécanisme de propagation des cellules a pu être étudié. Pour le point de fonctionnement sélectionné, certains passages du diffuseur sont affectés par un décollement de l'écoulement sur la directrice amont, ce qui engendre un blocage du passage. De plus, l'endroit où le décollement s'opère change avec le temps, ce qui est observable par la succession de phases croissantes et décroissantes du blocage d'un passage. La conséquence d'un tel blocage d'un passage est la déviation de l'écoulement vers le passage voisin en aval. En fonction de l'intensité de cette déviation, l'écoulement dans le passage aval va également décoller et bloquer ainsi passage, d'où la rotation de ces cellules de décollement.

Mots-clés: SGE, Pompe-turbine, Décollement Tournant, Mécanisme de Propagation, Mode de Pompage, Charge Partielle

Abstract

The increasing need of pump-turbines in today's and tomorrow's electrical power storage and grid stability requires new approaches to develop the knowledge of the structure of the internal flow of pump-turbines to improve their efficiency and to widen their range of operation. The main issue encountered when operating the pump-turbine in pumping mode at part load condition is the development of an instability in the diffuser known as the *rotating stall*. This instability consists in the development of recirculation zones, called stall cell, which result from a stall of the flow on a guide vane. Such a stall cell propagates from one guide vane channel to the neighboring downstream channel, which locally can be seen as the grow and decay of a recirculation zone.

As the stall cells are located in the diffuser, their investigation proves to be a complex task. Therefore, only a few studies exist up to this day. Experimentally, the visualization of the flow field is difficult because of the components (guide vanes, stay vanes,...) constituting the diffuser. Numerically, because of the high Reynolds number involved and the low computing power ressources, only the RANS approach could be used and showed the limits to accurately compute such a phenomenon with this approach. Thanks to the constant development of supercomputers, new perspectives are opened up and more elaborated numerical approach as the Large Eddy Simulation (LES) can be selected. Thus, the objective of this thesis is to perform a resolved Large Eddy Simulation to demonstrate that the rotating stall can be accurately computed by the LES approach to shed light on the physical mechanism behind the rotating stall phenomenon. To do this, the HYDRO-DYNA pump-turbine was selected and the computed flow is the one in pumping mode at part load condition, φ=0.026 (76% BEP). At such an operating condition, experimental investigation reported the presence of the rotating stall phenomenon.

To perform a resolved LES of a full pump-turbine, a sufficiently fine mesh has to be generated, as the size of the mesh governs the split between the large and the small structures in the flow. Since the LES approach computes explicitly the large structures and models the effect of the small ones, it is essential to capture all the main structures of the flow in order to accurately simulate the rotating stall phenomenon. In the present study, a feasibility study showed that the phenomenon could be captured using a mesh composed of 600 billions elements for a computation similar to the experiment, which is not feasible. However, if the Reynolds number is reduced by a factor 5 (Re/5), the required mesh is composed of 7 billions elements, which is today acceptable. If the Reynolds number is further reduced by a factor 5 (Re/25) the required mesh size decreases to 80 millions elements. Therefore, a mesh featuring 85 millions hexahedral elements was generated and used to initiate the flow field in the pump-turbine. The computation of the rotating stall requires the computation of several revolutions of the impeller and the fine spatial and temporal discretizations induce time consuming computations. Therefore, it

is mandatory to use a powerful supercomputer featuring a large number of cores. For the present computation, the PRIMEHPC-FX10 supercomputer of the University of Tokyo, which features approximately 80,000 cores, is used with an overset finite element large eddy simulation numerical code named FrontFlow/blue, which is developed at the same institution. Using 2,048 cores and the dynamic Smagorinsky model to close the system of equations, the computation of one impeller revolution can be performed within 7 hours.

The initialization of the flow field for the Re/5 case using the 85 millions elements mesh showed that the phenomenon could be captured after the computation of 10 impeller revolutions, i.e. four propagating stall cells are present in the diffuser. The computed energy coefficient Ψ is close to the experiment and is 3.35% higher compared to the experimental data. However, the computed propagation speed was approximately 60% slower compared to that of the experiment. This difference is due to insufficient resolution of the structure of the flow, as a 7 billions elements mesh would be required.

The flow computation for the Re/25 case, using the same 85 millions elements mesh, accurately reproduced the flow field in the pump-turbine. The resulting energy coefficient Ψ is only 0.36% higher compared to the experimental data. The same number of stall cells is predicted and the propagation speed of the stall cells is 3.4% slower than that of the experiment. Therefore, it is concluded that the rotating stall phenomenon is accurately reproduced.

Based on the accurate computation, the stall mechanism could be studied. It was shown that this instability involves the development of a recirculation zone near the trailing edge of the guide vanes on the suction side. The size of this recirculation zone almost periodically fluctuates and influences the surrounding flow field. Because of the geometry of the guide vane diffuser, it appeared that the recirculation possesses a strong influence and has the capability to nearly block the guide vane channel, which forces the flow to deviate to the neighboring channel. This deviation induces a modification of the flow in the downstream channel and results in favorable conditions for the flow to separate.

Contents

List of Figures

List of Tables

Notations

Latin

b	channel width	[m]
f_n	rotational frequency	[s^{-1}]
g	gravitational acceleration: $g \simeq 9.81$	[m·s^{-2}]
k	turbulent kinetic energy	[m^2·s^{-2}]
p	pressure	[Pa]
s	curvilinear coordinate	[-]
t	time	[s]
x, y, z	Cartesian coordinates	[m]
y^+	non-dimensional wall distance: $y^+ = \frac{C_\tau y}{\nu}$	[-]
z	number of blades, number of channels	[-]
A	surface area	[m^2]
$\boldsymbol{C}$	absolute velocity	[m·s^{-1}]
C	bulk velocity	[m·s^{-1}]
C_m	meridional velocity component	[m·s^{-1}]
C_n	velocity component normal to surface	[m·s^{-1}]
C_o	characteristic velocity	[m·s^{-1}]
C_r	radial velocity component	[m·s^{-1}]
C_s	Smagorinsky constant	[-]
C_t	velocity component tangential to surface	[m·s^{-1}]
C_u	circumferential velocity component	[m·s^{-1}]
C_τ	friction velocity: $C_\tau = \sqrt{\frac{\tau_\mathrm{w}}{\rho}}$	[m·s^{-1}]
E	pump specific hydraulic energy: $E = gH_I - gH_{\bar{I}}$	[J·kg^{-1}]
H	Head: $H = E/g$	[m]
L	length	[m]
L_o	characteristic length	[m]
N	rotational speed	[min^{-1}]
Q	flow rate	[m^3·s^{-1}]
R	radius	[m]
U	peripheral velocity	[m·s^{-1}]

Greek

α	absolute flow angle	[-]
β	relative flow angle	[-]
ϵ	turbulent dissipation rate	[m^2·s^{-3}]
τ	stress tensor	[Pa]
θ	angular coordinate	[-]
μ	viscosity	[Pa·s]
ν	kinematic viscosity ($\nu=\mu/\rho$)	[m^2·s^{-1}]
ϕ	stall phase	[-]
ρ	density	[kg·m^{-3}]
ω	impeller angular velocity	[rad·s^{-1}]
ω	specific dissipation rate	[s^{-1}]
ω_s	stall propagation velocity	[rad·s^{-1}]

Subscripts

1	reference to the circumference formed by the outer impeller diameter
2	reference to the circumference formed by the guide vane leading edge
e	reference to the shroud or element
n	normal to section
o	reference for non-dimensional numbers or nominal value
r	radial
ref	reference value
s	stall
t	throat
u	peripheral
w	wall
τ	shear

Superscripts

$*$	normalized quantity
$'$	fluctuating or modeled quantity
$^-$	resolved quantity
$\hat{\ }$	test-filtered quantity
$\sim$	low-pass filtered quantity

Dimensionless Numbers

c_{f}	skin friction coefficient	$c_{\mathrm{f}} = \dfrac{\tau}{\frac{1}{2}\rho U_{1\mathrm{e}}^2}$
C_{p}	pressure coefficient	$C_{\mathrm{p}} = \dfrac{p - p_{\mathrm{ref}}}{\frac{1}{2}\rho U_{1\mathrm{e}}^2}$
Re	Reynolds number	$Re = \dfrac{C_{\mathrm{o}}L_{\mathrm{o}}}{\nu}$
φ	flow rate coefficient (Pump-turbine)	$\varphi = \dfrac{Q}{\pi\omega R^3}$
ψ	specific energy coefficient	$\psi = \dfrac{2E}{\omega^2 R^2}$

Abbreviations

AOA	Angle Of Attack
EPFL	École polytechnique fédérale de Lausanne
BEP	Best Efficiency Point
BPF	Blade Passing Frequency
CFD	Computational Fluid Dynamics
CPU	Central Processing Units
DDR	Double Data Rate
DFT	Discrete Fourier Transform
DNS	Direct Numerical Simulation
FFB	FrontFlow/blue
GV	Guide Vane
LDV	Laser Doppler Velocimetry
LES	Large Eddy Simulation
LMH	Laboratoire de Machines Hydrauliques
MIC	Mass Imbalance Correction
RANS	Reynolds Averaged Navier-Stokes
RSI	Rotor Stator Interaction
SGS	Subgrid Scale
SP	Sampling Point
SV	Stay Vane

Part I

Introduction

Chapter 1

Problem Overview

1.1 Pumped-storage Power Plants

During these past decades, the energy demand has increased drastically requiring to improve the existing power stations and to find new sources of energy. Indeed, the world consumption of energy has increased by 180% during these past 30 years and has reached in 2010 150 quadrillion (10^{15}) Watt hour, see Fig. 1.1 a). Besides, the environmental concerns, regarding the present usage of the energy resources, push to reduce or even to abandon the use of some existing non-renewable resources such as nuclear, coal, oil or natural gas. However, a glance at Fig. 1.1 b) clearly shows the energetics dependence on the oil, coal and gas resources, as they are by far the main energetics contribution. Therefore, to reduce this energetics dependence, new resources with high electrical capacity should be found and hydropower is one of them. The hydropower generation can provide a large quantity of electricity and at the same time it has a lower impact on the environment, which makes it very popular nowadays. Furthermore, thanks to different technologies, a hydropower plant can be built in different places with different geographical topology to generate electricity: along a river, thanks to the high flow rate, or in mountainous area, thanks to the difference of height.

As mentioned above, the configuration of a hydropower plant is not unique and different approaches exist. The common approach is to use a dam to store and accumulate water. In terms of energy, this consists in storing water as potential energy. In a lower altitude than the dam, one or several water turbines are connected to the dam through a penstock. Released from the dam, the potential energy of the water is converted to kinematic energy, which is finally converted into electrical energy through the water turbine connected to a generator. Therefore, the difference of altitude and the flow rate passing through the water turbine determine the amount of power that can be generated. The drawback of this approach is that the available resources depend on the volume of water retained from the dam. Another approach is quite similar as the previous one as it also uses a dam, but with a low or no reservoir capacity. Such technology is known as "run-of-the-river" and it uses the flow rate of the river to generate electricity. The advantage of this approach is that it produces an almost constant amount of electricity provided by a constant river flow. There are other approaches that exist and which are under development, such as the ones using the tide (tidal power), the ocean currents (marine current power) or some small river (micro hydro).
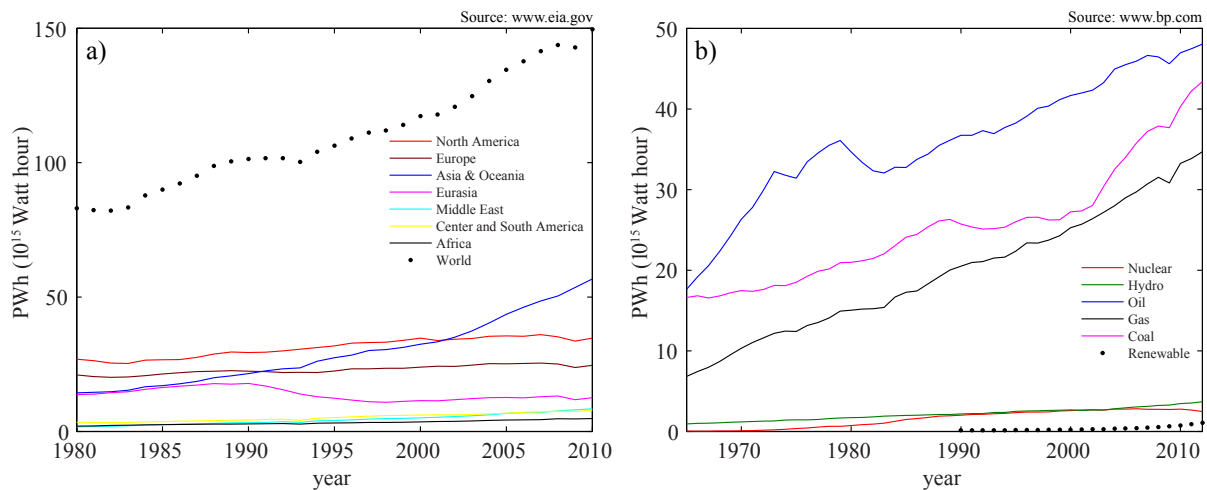
Figure 1.1: Evolution of the energy consumption in the world: a) per region, b) per resources.

Another energy issue encountered nowadays concerns the stability of the grids used to transport the electricity. On the one hand, these present grids are used near their limits and the variation between the supply and the demand induces electrical fluctuation on the grid, which cannot be avoided. Indeed, typical examples of the drop of the supply arise when the clouds decrease the radiant light and heat from the sun or when the intensity of the wind decreases and makes the wind turbines stop. On the other hand, the main variation of the demand is identifiable by the industry operating time, as well as by the short and large residential demand early in the morning and around noon. Therefore, it is primordial to have the technology able to respond to these variations of the supply and the demand. This means that the technology has to provide energy when the supply is lower than the demand, and that the technology has to store the energy when the demand is lower than the supply. In that context, the pumped-storage power plants are the best technology. Indeed, only a few minutes are required to start the machine and to synchronise it with the grid. Furthermore, by adjusting the flow rate, it is possible to control precisely the electrical power generated, making that technology very attractive. To respond to the supply excess, pumps are installed to pump water from a lower reservoir to an upper reservoir. Such pumped water will be used later to generate electricity when the demand exceeds the supply. Finally, another reason that makes this approach attractive is that it is economically viable. The price of the kilowatt hour (kWh) during the day is not constant and it fluctuates regarding the demand. Therefore, the pumped-storage power plants generate electricity during the peak of demand and sell the electricity when the price of the kWh is high. Inversely, the plants buy the electricity to pump the water when, as already mentioned, the demand is lower than the supply and, therefore, the price of the kWh is low. Originally, such a plant was equipped with a water turbine, a pump and an electrical engine or generator, and it runs the engine or the generator depending on whether the plant is in pumping or generating mode. However, for economical reason, it is advantageous to merge the water turbine and the pump which results in the so called reversible pump-turbine.

The reversible pump-turbines are devoted to a specific implementation and are, therefore, designed for a fixed flow rate Q and a fixed net hydraulic head H. However, the

present requirements make the pump-turbines to be used at off-design conditions. Therefore, there is a need to expand the operating range of such a machine and at the same time to ensure the safety of the machine for that range. So far, two main problems have been reported: at full load condition ($Q > Q_{\mathrm{BEP}}$) cavitation may occur, and at part load condition ($Q < Q_{\mathrm{BEP}}$) the rotating stall phenomenon may occur. These phenomena have to be studied because they can have a dramatic issue on the machine. In a weak occurrence of these phenomena, noise and vibration are perceptible and the efficiency of the machine decreases. However, if the intensity of these phenomena are high, it can result in severe damage to the machine, which in the worst case, can destroy the machine within a few hours of operation. Therefore, there is a necessity to understand these phenomena in order to expand the operating range of the machine. So far, the rotating stall is still an unclear phenomenon and needs to be more detailed, especially for the hydraulic machine for which almost no study exists.

1.2   Rotating Stall

The rotating stall is a generic name to describe a particular phenomenon appearing in a rotating machine. This phenomenon can be seen as a local modification of the flow by the presence of a single or multiple recirculation zones. As these zones are located near walls and they imply a reverse flow, such zones are often referred to as *stall* or as *flow separation* [29]. Besides, depending on the location of the recirculation zones, the stall phenomenon can be referred to as *forward/backward rotating stall, alternate blade stall* or *asymmetric stall*.

The problem of the presence of the so called rotating or alternate stall phenomenon in a centrifugal pump is now well known. However, the onset and the mechanism of this phenomenon are still poorly understood. The first time that this phenomenon was reported was by Emmons in 1959 when he explained the phenomena using cascade theory, [14], and was intensively studied numerically and experimentally in the case of compressors, [18], [9]. However, much longer time was required to get similar studies for centrifugal pump experiencing rotating stall. Indeed, one of the first experimental studies on radial machine was performed by Krain, [33], and Inoue et al., [23], where focus was put on impeller blade pressure and flow field investigation in centrifugal impeller for radial turbomachinery. Deeper investigations followed with the studies of the rotor stator interaction performed by Arndt et al., [2], [1]. They showed that the pressure fluctuation appears to be larger on the vane suction side near the trailing edge and that the magnitude of the pressure fluctuation is strongly dependent on the radial gap (distance between the impeller discharge and the diffuser vane leading edge). The importance of such gap will be later emphasized by Sano et al., [51].

Finally, the first experimental investigation of the so called rotating stall in centrifugal pump took place only during these last ten years. Indeed, Sinha et al., [54], [55], [56] were the first to investigate this phenomenon in a vaned diffuser of a centrifugal pump with the Particle Image Velocimetry (PIV). In the same time, new details on the importance of the narrow clearance and its impact on the rotating stall were demonstrated by Sano et al., [51]. The clearance, also refered to as gap, is the distance between the trailing edge of the impeller blade and the leading edge of the diffuser vane. Finally, almost all experimental studies were performed with the PIV method to investigate the structure of the flow or

the influence of the flow rate on the rotating stall, [64], [45], [34]. Numerical research on the rotating stall phenomenon started once again for an axial type vaned diffuser coupled with a centrifugal impeller performed by Torbergsen [59]. This simulation was performed using the Reynolds Averaged Navier Stokes (RANS) method. Another study was carried out by Sano, [52] where the interest was on the onset of the rotating stall and to assess the accuracy of the computation by comparison with their experimental data [51]. Finally, 3D numerical simulation was performed by Braun, [3] for a complete centrifugal pump. Recently, other simulations on the rotating stall were performed by Lucius [38] in order to compare the performance of the SAS and the SST turbulence models.

Concerning the Large Eddy Simulation (LES) method the first simulation was performed by Kato, [27] in the case of a mixed-flow pump and the first LES simulation in a centrifugal pump with the interest in the rotating stall was performed by Byskov, [4].

1.3 High Performance Computing

The term High Performance Computing (HPC) refers to the use of supercomputers or clusters of computers to solve difficult computational problems. Concretely, it consists in assembling a large amount of processors to increase the size of the memory and to decrease the operating time by using a large number of cores. Looking at the last fifty years, one can see that a drastic change has occurred. Indeed, although the first "supercomputer" featured only a few number of cores, the latest supercomputers feature up to million of cores. This change comes from the capacity to reduce the size of the transistors, to make them faster and to assemble them in a way to produce massively parallel computers. Interestingly, this change in the computing power was approximately predicted in the 1960s by Gordon Moore, who is the designer of one of the first supercomputers. At that time, while working on integrated circuit, which is the basis for computers, he made the estimation that the number of transistors per square inch on integrated circuits would roughly double every year [42]. However, in 1975, this estimation had to be changed and the new estimation moved from 12 to 24 months [43]. Following this previous estimation, we can see that it got verified for the evolution of the computing power. Figure 1.2 shows the computing power evolution from 1971 to 2011 in a logarithmic representation. The straight line corresponds to the trend for doubling the number of transistors every two years, which corresponds well to the computing power evolution. To achieve this power evolution, the size of the transistor was constantly scaled down following the Dennard scaling down to 130 nm [11]. This allowed to increase the power density and meanwhile to increase the performance. However, to decrease the transistor size below 130 nm, a new approach had to be found as the Dennard scaling was not sufficient enough to increase the performance. To reach from the 90 nm transistors to the 32 nm transistors, work was done on the material, which permitted the size decrease with the performance increase. However, the transistor size will not become infinitely small and, therefore, one can wonder what will be the size limit of a transistor?

Since 1993, a project named Top500[1] has compiled twice a year (June and November) a list indexing the 500 fastest supercomputers based on the standardized LINPACK benchmark developed by Jack Dongarra [13]. Basically, the LINPACK benchmark solves a

---

1. `http://www.top500.org/`
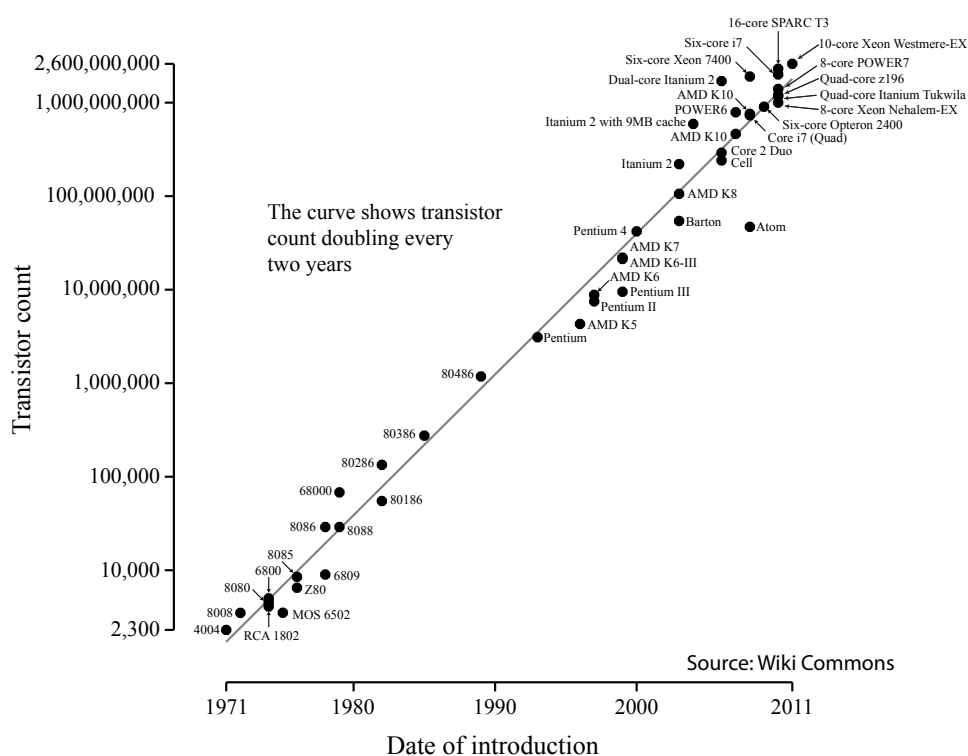
Figure 1.2: Microprocessor transistor counts from 1971 to 2011. The straight line shows the Moore's law.

dense n by n system of linear equations $Ax=b$ to measure the number of floating point operations per second. The authors of these lists are Hans Meuer (University of Mannheim, Germany), Erich Strohmaier (currently at Lawrence Berkeley National University, but previously at the University of Mannheim), Jack Dongarra (University of Tennessee and ORNL) and since 2000, Horst Simon (Lawrence Berkeley National University). These lists also permit to index the location of the supercomputers and to describe the kind of applications for which a supercomputer is used. Table 1.1 gives the top 10 supercomputer elaborated in November 2013. As it can be seen, the fastest computer (Tianhe-2) is located in China and features 3.12 millions of cores. Furthermore, Japan's "K computer" was the first in November 2011 to achieve a performance level of 10 PFLOPS (10^{15} calculations per second). Since then, all the effort is done to reach the EFLOPS (10^{18} calculations per second) level by 2020. Last december, RIKEN (in Japanese: Rikagaku Kenkyuujo and in English: Institute of Physical and Chemical Research) was selected to develop an exascale supercomputer, which should start operating by 2020.

1.4 Numerical Simulation Specification

1.4.1 RANS, LES and DNS Tradeoffs

Since the development of computers and CFD software, numerical simulation has been extensively used, both in academia and industries. Such an approach has the advantage that it can be a cheaper approach compared to the experiment and can, for a specific case study, provide more accurate and more detailed data. However, this approach also faces

Table 1.1: Supercomputer top 10 of the Top500 list, as of November 2013.

Rank	Country	Name	Manufacturer	Nb of cores	Linpack Perf. TFLOPS
1	China	Tianhe-2	NUDT	3,120,000	33,862.7
2	United States	Titan	Cray Inc.	560,640	17,590.0
3	United States	Sequoia	IBM	1,572,864	17,173.2
4	Japan	K computer	Fujitsu	705,024	10,510.0
5	United States	Mira	IBM	786,432	8,586.7
6	Switzerland	Piz Daint	Cray Inc	115,984	6,271.0
7	United States	Stampede	Dell	462,462	5,168.1
8	Germany	JUQUEEN	IBM	458,752	5,008.9
9	United States	Vulcan	IBM	393,216	4,293.3
10	Germany	SuperMUC	IBM	147,456	2,897.0

its inherent limitations, which induce different ways in performing numerical simulation known as Reynolds Averaged Navier-Stokes (RANS), Large Eddy Simulation (LES) and Direct Numerical Simulation (DNS).

DNS is the most constraining approach as it explicitly computes all the turbulence scales using the unsteady Navier-Stokes equations, but it provides the most accurate solution as long as the space-time discretization is sufficiently fine. To estimate the spatial discretization, one can use the work performed by Kolmogorov [31], [47], which provides an estimation on the ratio of the biggest to the smallest eddies present in a flow with regard to the Reynolds number. Using such an estimation, the space discretization requirement is of the order $L/\eta=\mathrm{O}(\mathrm{Re}^{3/4})$, where L characterizes the largest scales and η the smallest ones. Re is the Reynolds number, which expresses the ratio of the inertial force to the viscous force. The definition of the Reynolds number is as follows: Re=$C_0 L_0/\nu$, where C_0 is a characteristic velocity, L_0 a characteristic length and ν the kinematic viscosity. For 3D cases, such space requirement becomes $\mathrm{O}(\mathrm{Re}^{9/4})$ in terms of number of the computational grids, which is considerable. Knowing that the typical range of the Reynolds number for industrial applications is 10^6-10^8, it implies that the number of the computational grids is of the order of 10^{13}-10^{18}, which is not feasible today and neither is for the next decades. Furthermore, accurate computation also requires a fine temporal discretization, which makes DNS a difficult approach. Therefore, DNS is mainly used for computation of a low Re flow with a simple geometry.

RANS can be seen as the opposite of DNS as it is the most economical and the most popular approach for engineering applications. RANS approach computes flows using the Navier-Stokes equation, where the pressure and the velocity are decomposed into the statistical average quantity and the fluctuating quantity. Therefore, RANS computation provides only statistical average solution, and no information regarding the fluctuation is available. The fluctuation term arising from the decomposition is thus unknown and has to be modeled. Furthermore, such a fluctuation is flow dependent and is therefore complicated to model. Since the above decomposition was introduced by O. Reynolds, many models were developed aiming at reproducing correctly the influence of the fluctuation on the statistical average quantities. Nowadays, one of the most popular RANS turbulence models used is the one developed by Menter [40],[41], called $k-\omega$ SST. This

model combines the two known models for $k - \epsilon$, [24], [35] and $k - \omega$, [62], [63], in order to take advantage of both models, and gives satisfactory results most of the time. However, regarding the phenomena of interest, it was shown by the study of O. Braun [3] that the RANS approach with the $k - \omega$ SST model faces difficulties in accurately simulating the rotating stall. Therefore, another approach should be considered.

LES stands between the RANS and DNS approaches. As DNS does, LES explicitly computes the different scales, but only to a specific size dictated by a filter width. Similarly to RANS, the influence of the small scales on the big ones is modeled through the so called subgrid scale (SGS) model. The challenge with this approach is to find the appropriate balance between time-space resolution and accuracy, or in other words to have a sufficiently fine grid resolution in order to dissipate all the energy produced. The turbulent production arises from the large scales, whereas the dissipation occurs in the small scales. Therefore, if the grid is too coarse to accurately represent the small scales, the energy accumulates within the flow leading to nonphysical solutions. As the LES grid is not fine enough to resolve all the turbulence scales, the task of the subgrid scale model is to mimic the effect of the scales smaller than the filter width on the scales bigger than the filter width. However, such a modeling is not trivial because it requires the knowledge of the turbulence structures, which is flow dependant. Furthermore, another main difficulty encountered by the LES approach is the computation of boundary layers. This requires a fine discretization near walls in order to represent accurately the boundary layer up to the viscous sublayer, increasing drastically the need in spatial resolution [46]. These resolution requirements are thus the limiting reason to use such an approach. However, the constant increase of the computing power during these past decades makes the LES approach more and more feasible. Meanwhile, the work performed on the development of numerical codes in order to have a good scalability to accommodate tens of thousand cores also increased the opportunity to perform LES computation. The use of such an amount of cores provides a large amount of available memory with a relatively weak core load, resulting in computations that can be carried out in a relatively short amount of time. Nevertheless, despite all these improvements some industrial investigations can not be numerically performed yet. Therefore, a feasibility study on the mesh size and the computing resources requirements is mandatory.

The process of the feasibility study can be decomposed into three parts. The first part consists in a short analysis to estimate what are the physics involved in the research of interest. Such estimation is primordial, as it indicates the size of the smallest structures present in the flow to be computed. The second part consists in estimating the size of the spatial discretization requirement with regards to the small scales to be computed. Finally, the third part consists in the estimation of the computing resources requirement to perform the computation of interest. In the following, a feasibility study is carried out to determine the requirement to compute the rotating stall in a full pump-turbine scaled model by the LES approach.

1.4.2 The smallest eddies to be computed

The present research focuses on the rotating stall appearing in a pump-turbine being operated in pumping mode and at part load condition (76% BEP). The rotating stall phenomena is an instability recognizable by the presence of stall cells in the pump-turbine diffuser, which propagate, at a low ratio of the impeller frequency, from one diffuser

Table 1.2: Sizes of streamwise vortices expressed in wall unit: $y^+=yC_\tau/\nu$.

Length	300
Diameter	30
Spanwise spacing	150

channel to the neighboring diffuser channel in the same direction as the impeller rotation. Their presence is the result of part load condition, which induces a misalignment of the incoming flow to the diffuser guide vanes and induces favorable condition for flow separation. The physics to be computed involve mainly the flow exiting the impeller and the flow around the guide vanes, which can be regarded as a hydrofoil. Because the phenomena of interest is unsteady, the time and spatial evolutions of the boundary layer around these hydrofoils have to be computed. Regarding the Reynolds number considered, the nature of the boundary layer is turbulent. Based on extensive former researches [21],[30],[48],[53], it is known that a turbulent boundary layer can be characterized by the presence of coherent structures, which are long streamwise vortices. For the present research, it is assumed that capturing such structures should be sufficient to compute the phenomena of interest, that is, the rotating stall. The physical size of such vortices can be estimated using their dimensionless size, see Table 1.2, and such a physical size will be used to estimate the spatial discretization requirement.

1.4.3 Mesh Requirements

To estimate the physical size of the streamwise vortices, the viscous length $l=\nu/C_\tau$, which links the dimensionless wall unit to the dimension one, has to be determined. However, the complexity of such an evaluation is that the friction velocity, which is unknown and is dependent on time and space, also has to be determined. Based on the flat plate boundary layer theory, an approximation of the friction velocity can be computed using the following formulas developed initially by Chapman [5], and a correction for high Reynolds number suggested by Choi et al. [6]. Such formulas relate the mean flow velocity to the friction velocity using the wall skin friction coefficient c_f and the Reynolds number. The variation of the wall skin friction coefficient with regards to the Reynolds number is depicted in Fig. 1.3.

$$
\begin{aligned}
\frac{C_\tau}{C} &= \sqrt{\frac{c_f}{2}} \\
c_f &= 0.0577 Re_x^{-1/5} &&\text{for } Re_x \leq 10^6 \\
c_f &= 0.027 Re_x^{-1/7} &&\text{for } 10^6 \leq Re_x \leq 10^9
\end{aligned}
\tag{1.1}
$$

However, the Reynolds number is dependent on the choice of a characteristic length and a characteristic velocity, which can vary significantly. As the velocity of the flow field in the diffuser is driven by the impeller revolution, it is assumed that the absolute velocity C_1 at the impeller outlet is the characteristic velocity. Furthermore, the flow in the diffuser will first evolve by passing around the guide vanes. Then, the characteristic length selected is the guide vane chord length, which results in a Reynolds number of 1.9 millions.

For a Reynolds number of 1.9 million, the ratio between the friction velocity and the absolute velocity is 4% giving a viscous length of 1.24 μm. The expected dimensions
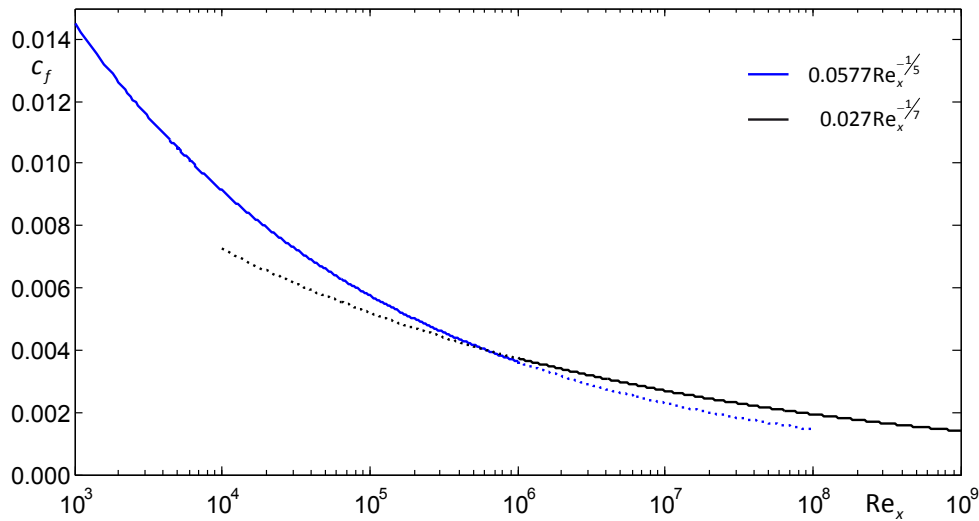
Figure 1.3: Flat plate wall skin friction coefficient as a function of the Reynolds number

in mm of these streamwise vortices are thus given in Table 1.3. To estimate the total number of elements, it is assumed that the volume of fluid between two adjacent diffuser guide vanes can be represented by a rectangular box with the following dimension: 100 x 75 x 35 mm representing respectively the streamwise, transverse and spanwise directions. Furthermore, to estimate the total number of elements for the full pump-turbine, it is assumed that the pump-turbine has 87 similar volumes of fluid: 3 for each impeller channel, 1 for each guide vane channel and 2 for each stay vane channel. Finally, to compute the number of elements per direction, the following spatial discretization was selected: $x^+=50$, $y^+= z^+=20$. This estimation has resulted in that the present computation will need 600 billions of elements. This is of course not feasible and the following change was adopted: based on the Reynolds-number similarity, the Reynolds number was reduced by a factor 5 in order to reach a realistic spatial discretization. The new required mesh is approximately 7 billions, which is nowadays feasible.

Table 1.3: Physical sizes of the streamwise vortices together with the corresponding grid discretization expressed in millimeter. The number of elements estimation is done for a velocity reference C_1 and for a velocity 5 times smaller, $C_1/5$, and 25 times smaller, $C_1/25$. The physical domain, consisting in the volume of fluid between two guide vanes, is represented by a rectangular box of 100x75x35 mm. The total number of elements is obtained assuming that the pump-turbine can be represented by 87 similar volumes of fluid.

	C_1	$C_1/5$	$C_1/25$
Vortex length [mm]	0.37	1.6	7.43
Vortex diameter [mm]	0.037	0.16	0.74
Vortex spacing [mm]	0.19	0.8	3.7
Streamwise grid resolution [mm]	0.06	0.27	1.24
Transverse and spanwise grid resolution [mm]	0.025	0.11	0.5
Number of elements per passage [-]	$7 \cdot 10^9$	$80 \cdot 10^6$	$1 \cdot 10^6$
Number of elements for the pump-turbine [-]	$600 \cdot 10^9$	$7 \cdot 10^9$	$80 \cdot 10^6$

1.4.4 Computing Resources Requirement

Since the estimation on the mesh size is carried out, one can estimate the computing resources in terms of memory size, amount of computing nodes and resources allocation requirement. To perform this estimation, some characteristics of the CFD software and the computation are necessary. In the present research, computation will be performed using FrontFlow/blue (FFB) software developed at the University of Tokyo. This software has already been successfully ported to several supercomputer architectures, and time measurements have shown that the sustained peak performance of the code is approximately 5% of the peak performance up to several ten thousands cores, that it requires about 20k floating point operation (FLOP) per element per time step and that the appropriate load balancing is 0.1 million elements per processor core. As introduced previously, the estimated size of the mesh is 7 billion elements. Furthermore, the time discretization is 10,000 time steps per impeller revolution and the number of impeller revolutions to compute to perform statistics is 40.

The computation will be performed on the supercomputer K, belonging to RIKEN. This supercomputer features 8 cores per computing node with a total number of computing nodes over 80,000 for a peak performance of 128 GFLOPS per computing node. Using the above information, the computation requires 10,000 computing nodes and one impeller revolution lasts approximately 7 hours. This results in the computation of 40 impeller revolutions within 12 days.

In conclusion, the feasibility study showed that such a computation is nowadays possible and that thanks to important resources, results can be obtained in a reasonable time.

1.5 Thesis Objective

Nowadays, the rotating stall is still a common issue when pumps are operated at part load condition. To better understand this phenomenon and to predict its impact for a specific machine, experimental or numerical research is usually performed. However, the location of the instability in the machine makes the experimental study difficult. Therefore, the numerical approach is often preferred, as the study of internal flows is easier. So far, numerical investigations were mainly done using the RANS approach or a resolved LES approach. Because of the constraining requirements of LES, some studies simplified the geometry by using symmetry assumption. Such simplification reduces the size of the computational mesh and make the study possible. However, as the rotating stall phenomenon modifies the flow in the upstream area of the diffuser in the circumferential direction, the flow field in the impeller may be affected and, therefore, the use of symmetry assumption should be avoided. From the knowledge of the author, there is presently no LES computation performed to study the rotating stall phenomenon without using any geometrical simplification. Therefore, thanks to new computational opportunities, the objective of this research is to perform a resolved LES, by resolving the streamwise vortices, and to demonstrate that the rotating stall can be accurately computed by the LES approach without the use of geometric symmetry. The selected case study is the HYDRODYNA pump-turbine, where the rotating stall phenomenon was experimentally observed [3], when operating the pump at 76% of the design point. This experimental

research will be used to assess the accuracy of the computation, which will allow us to demonstrate the mechanism of the rotating stall occurring in the present pump-turbine.

1.5.1 Document Organization

The thesis has been divided into four parts:

- Part I regroups the introducing chapters regarding the rotating stall phenomenon. It shows that the increasing needs to extend the operating range of a pump-turbine may lead to the appearance of the rotating stall phenomenon. Meanwhile, the increase of the computing power offers the possibility to study numerically this phenomenon using the LES approach, which has been often seen as an unfeasible approach for industrial studies. A feasibility study is then carried out and assesses that the LES approach is suitable to compute the flow field of the complete scale model pump-turbine.
- Part II is dedicated to the numerical investigation methodology. It introduces the LES approach with the turbulence model used. Then the different numerical tools required for this research are described: the numerical code, the computing resources and the visualization software. Part II concludes with the presentation of the pump-turbine characteristics, its spatial discretization and the flow initialization.
- Part III presents the results of the unsteady computation of the pump-turbine part load flow. First the computation is compared to the experimental data, and secondly the propagation mechanism of the rotating stall is discussed.
- Part IV draws the concluding remarks.

Part II

Methodology

Chapter 2

Large Eddy Simulation

2.1   Large and Small Scales Separation

The LES approach relies on the separation of the large and small scales from the solution. This separation is performed by applying a spatial filter to the governing equations of the fluid motion and is illustrated in Fig. 2.1, where a schematic representation of the kinetic energy spectrum is split in two parts. The left part represents the energy contained in the large scales, whereas the right part represents the energy contained in the small scales. The scale size at which the separation takes place depends on the filter width, which is a parameter when using an explicit filter or is the computational grid size when using an implicit filter. The LES approach computes thus explicitly all the scales larger than the filter width and computes the effect of the small ones through the use of a subgrid scale model. The filtering process and the subgrid modeling are introduced respectively in the following two sections.

2.2   Low-Pass Filtered Incompressible Navier-Stokes Equations

The governing equations of an incompressible fluid arise from two conservation laws, which are the momentum (based on Newton's second law) and mass conservation laws. The momentum equation expresses the link between the acceleration of a fluid particle to the surface forces and body forces experienced by the fluid. In the case where the body force is gravity, the force can be expressed through the gravitational potential Ψ, defined as $\Psi = gZ$ for a constant gravitational force. Therefore, the body force per unit mass is defined as $\boldsymbol{g} = -\nabla\Psi$. Using the previous definition for the body force, the two laws can be mathematically written as follow:

$$\rho\frac{\mathrm{D}C_i}{\mathrm{D}t} = \rho\left(\frac{\partial C_i}{\partial t} + C_j\frac{\partial C_i}{\partial x_j}\right) = \frac{\tau_{ij}}{\partial x_j} - \rho\frac{\partial\Psi}{\partial x_i} \qquad (2.1)$$

$$\frac{\partial\rho}{\partial t} + \frac{\partial}{\partial x_i}\cdot(\rho C_i) = 0 \qquad (2.2)$$
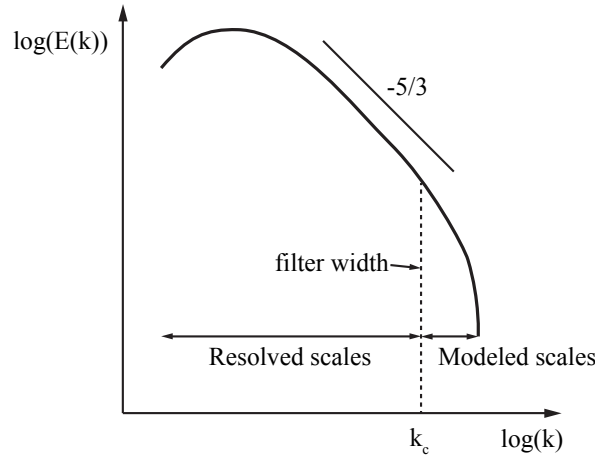
Figure 2.1: Schematic view of the energy spectrum showing the scales separation.

where τ_{ij} is the stress tensor, C_i components of the absolute flow velocity and ρ the density. In the case of an incompressible Newtonian fluid, the stress tensor can be expresses as:

$$\tau_{ij} = -P\delta_{ij} + \mu \left(\frac{\partial C_i}{\partial x_j} + \frac{\partial C_j}{\partial x_i} \right) \tag{2.3}$$

where P is the pressure, δ_{ij} the Kronecker's delta and μ the viscosity. In the case of an incompressible fluid, Eq. (2.2) reduces to $\partial C_i / \partial x_i = 0$ and the stress can be seen as the sum of the isotropic tensor $(-P\delta_{ij})$ and the deviatoric contributions by using the last expression and assuming that the density ρ is time and space independent, we obtain the Navier-Stokes (NS) equations for an incompressible fluid:

$$\rho \left(\frac{\partial C_i}{\partial t} + C_j \frac{\partial C_i}{\partial x_j} \right) = -\frac{\partial P}{\partial x_i} + \mu \frac{\partial^2 C_i}{\partial x_j \partial x_j} - \rho \frac{\partial \Psi}{\partial x_i} \tag{2.4}$$

Defining a modified pressure p, as

$$p = P + \rho \Psi \tag{2.5}$$

the governing equations of a Newtonian incompressible flow becomes:

$$\frac{\partial C_i}{\partial t} + C_j \frac{\partial C_i}{\partial x_j} = -\frac{1}{\rho} \frac{\partial p}{\partial x_i} + \nu \frac{\partial^2 C_i}{\partial x_j \partial x_j} \tag{2.6}$$

$$\frac{\partial C_i}{\partial x_i} = 0 \tag{2.7}$$

where ν is the kinematic viscosity of the fluid.

The modified pressure shows that the effect of the isotropic stress and the body forces have the same effect. Hence, the body force has no effect on the velocity field and on the modified pressure. Henceforth, the modified pressure p may be simply referred to as pressure [47]. Besides, Eqs. (2.6) and (2.7) are commonly expressed in the dimensionless form using the following dimensionless variables $x_i^* = x_i/L$, $C_i^* = C_i/C$, $t^* = t/(L/C)$ and $p^* = p/(\rho C^{*2})$, where L and C are respectively a characteristic length and velocity.

This dimensionless form clearly highlights the importance of the non-linear term for flows with high Reynolds number.

$$\frac{\partial C_i^*}{\partial t^*} + C_j^* \frac{\partial C_i^*}{\partial x_j^*} = -\frac{\partial p^*}{\partial x_i^*} + \frac{1}{\text{Re}} \frac{\partial^2 C_i^*}{\partial x_j^* \partial x_j^*} \tag{2.8}$$

$$\frac{\partial C_i^*}{\partial x_i^*} = 0 \tag{2.9}$$

The LES approach relies on a filtering process to damp out the turbulence scales smaller than the filter width. Therefore, every instantaneous quantity is decomposed into a resolved quantity ($\overline{f}$) and a modeled quantity (f'):

$$C_i(\mathbf{x}, t) = \overline{C}_i(\mathbf{x}, t) + C_i'(\mathbf{x}, t) \qquad p(\mathbf{x}, t) = \overline{p}(\mathbf{x}, t) + p'(\mathbf{x}, t) \tag{2.10}$$

By applying these decompositions to the NS equations, one obtains the incompressible low-pass filtered NS equations:

$$\frac{\partial \overline{C}_i}{\partial t} + \frac{\partial}{\partial x_j}\left(\overline{C}_i \overline{C}_j\right) = -\frac{1}{\rho}\frac{\partial \overline{p}}{\partial x_i} + \frac{\partial}{\partial x_j}\left[\nu\left(\frac{\partial \overline{C}_i}{\partial x_j} + \frac{\partial \overline{C}_j}{\partial x_i}\right) - B_{ij}\right] \tag{2.11}$$

where B_{ij} represents the subgrid-scale (SGS) tensor, which can be expressed as:

$$B_{ij} = \overline{C_i C_j} - \overline{C}_i \overline{C}_j \tag{2.12}$$

Using the statistical property, one can rewrite the SGS as:

$$B_{ij} = \underbrace{\overline{\overline{C}_i \overline{C}_j} - \overline{C}_i \overline{C}_j}_{L} + \underbrace{\left(\overline{\overline{C}_i C_j'} + \overline{\overline{C}_j C_i'}\right)}_{C} + \underbrace{\overline{C_i' C_j'}}_{R} \tag{2.13}$$

where $\boldsymbol{L}$ represents the "Leonard term", C the "cross term" and R the "Reynolds-stress like term". The Leonard term is the only one which can be calculated explicitly. Depending on the case studied it could be better to take out the Leonard term from the previous equation, which led to a new kind of SGS. However, in most SGS model this decomposition is not done and the SGS tensor B_{ij} is modeled as a whole.

2.3 Subgrid-scale Modeling

As introduced previously, the filtering process separates the large (resolved) and the small (modeled) scales and generates new unknowns gathered into the subgrid-scale tensor B_{ij}, which has to be modeled. The process of this modeling is first to represent the structure of the small scales of motion and secondly to represent the interactions between the modeled and the resolved scales. As LES is performed using a coarse computational mesh, the filter width is obviously located somewhere in between the largest and the smallest scales and deals with the inter-scales flow structures. It is evident that no universal tensor can be provided, as the physical behavior of the inter-scales and the small scales are flow dependent. Therefore, two strategies are adopted to incorporate the action of the small scales: functional modeling and structural modeling [50]. Looking at Eq. (2.11), one can

see that the subgrid scale tensor in the NS equations is in the form $\nabla \cdot \boldsymbol{B}$. Hence, one can model the term $\nabla \cdot \boldsymbol{B}$ as a whole or model the tensor $\boldsymbol{B}$ itself. The first approach is used for the functional modeling, whereas the second one is used for the structural modeling.

Since the modeling process requires the knowledge of the flow structure, the study case of the fully developed isotropic homogeneous turbulence was extensively used, as it is the only case that can be accessible by theoretical analysis. Therefore, the initial modeling were only dedicated for the computation of isotropic flow. The DNS research dedicated to find the location where the subgrid energy transfer occurs and what correlation exists between the different scales, permitted to show that the interaction between the small and the large scales is driven by two mechanisms. The first, which is the dominant mechanism, is assimilate to an energy drainage from the large scales to the small ones and is referred to as forward energy cascade phenomenon. The second mechanism is a weak energy feedback to the large scales and is referred to as backward energy cascade [50]. Furthermore, it was shown that the cascade mechanisms are associated to specific features of the velocity and vorticity field in the physical space [8], [28].

Functional modeling

The functional modeling in the physical space explicitly model the forward energy cascade mechanism to the subgrid scales. It relies on the hypothesis that the transfer mechanism from the resolved to subgrid scales is analogous to the molecular mechanisms represented by the diffusion term, in which the viscosity ν appears. Therefore, the mathematical form of the subgrid scale model, as Boussinesq proposed, is written as:

$$-\nabla \cdot \boldsymbol{B}^d = \nabla \cdot \left(\nu_{\text{sgs}} \left(\nabla \overline{\boldsymbol{C}} + \nabla^T \overline{\boldsymbol{C}} \right) \right) \tag{2.14}$$

where $\boldsymbol{B}^d$ is the deviatoric of $\boldsymbol{B}$ defined as:

$$B_{ij}^d = B_{ij} - \frac{1}{3} B_{kk} \delta_{ij} \tag{2.15}$$

The spherical tensor $\frac{1}{3} B_{kk} \delta_{ij}$ is added to the filtered static pressure and does not need to be modeled. Such decomposition is required, because for incompressible flows the tensor $\left(\nabla \overline{\boldsymbol{C}} + \nabla^T \overline{\boldsymbol{C}} \right)$ has a zero trace and thus the model has to have also a zero trace. Therefore, the model reduces in determining a relation of the form:

$$\nu_{\text{sgs}} = F(\overline{\boldsymbol{C}}) \tag{2.16}$$

Several examples of functional models can be found in [50] and the one from Smagorinsky is introduced later in section 2.3.1.

Structural modeling

The structural modeling in opposite to the functional modeling does not rely on the knowledge of the nature of the interaction between the large and the small scales, but aims to approximate directly the subgrid tensor B_{ij} from the resolved velocity field or from a formal series expansion [50].

2.3.1 Smagorinsky Model

The Smagorinsky model [57] is a subgrid viscosity model of the form of Eq. (2.16), which relies on the large scales. This model is expressed as:

$$\nu_{\text{sgs}}(\boldsymbol{x}, t) = \left(C_{\text{s}}\overline{\Delta}\right)^2 \left(2|\overline{S}(\boldsymbol{x}, t)|^2\right)^{1/2} \tag{2.17}$$

where C_{s} is the Smagorinsky constant, $\overline{\Delta}$ the filter width and $\overline{S}$ the resolved strain rate. The two main drawbacks of this model is firstly that it depends on the constant C_{s} that needs to be adjusted and secondly that it depends on the strain rate $\overline{S}$ of the large scales. Therefore, as long as the flow exhibits spatial variations, the subgrid viscosity is non-zero even if all scales are resolved as for example with a laminar flow. Such a model should thus be used for fully turbulent and under-resolved flows. Regarding the constant, it should be tuned in order that the ensemble-average subgrid kinetic energy dissipation rate is equal to ϵ, with ϵ being the kinetic energy dissipation rate. The first LES using the Smagorinsky model was done by Deardorff [10], where he used C_{s}=0.1 for a plane channel flow. Another study by Clark et al. [7] used a C_{s}=0.2 for an isotropic homogeneous turbulence computation. Several other studies suggested a constant between 0.1 and 0.12 [39], [60], [44]. Therefore, no universal constant is available. An approach to avoid this constant is to evaluate its value locally in space and time with regards to the local flow field. This approach is introduced in the following.

Dynamic Smagorinsky Model

The dynamic Smagorinsky model is similar to the Smagorinsky model except that the coefficient C_{s} is no longer constant but changes in space and time during the simulation. The purpose is to dynamically adapt this coefficient to the state of the flow to increase the accuracy of the solution. The first dynamic approach to evaluate the Smagorinsky coefficient was presented by Germano et al. [16]. This approach is subject to a source of singularity, which has led to a modification of the Germano subgrid-scale closure method by Lilly [37]. These "two" dynamic models rely on a second filtering of the Navier-Stokes equations. This second filter is usually called "test filter" and its width ($\widehat{\Delta}$) is often set twice the original filter width. The idea from this two filtering is known as the Germano identity, which shows that two tensors corresponding to two different filtering levels can be related by an exact relation.

The first tensor, is simply the subgrid tensor from the initial filtering, with the Smagorinsky model:

$$B_{ij} - \frac{1}{3}\delta_{ij}B_{kk} = 2C_{\text{s}}\overline{\Delta}^2|\overline{S}|\overline{S}_{ij} \tag{2.18}$$

The second tensor, is obtained by applying the test filter to the filtered equations:

$$T_{ij} - \frac{1}{3}\delta_{ij}T_{kk} = 2C_{\text{s}}\widehat{\overline{\Delta}}^2|\widehat{\overline{S}}|\widehat{\overline{S}}_{ij} \tag{2.19}$$

Germano showed on the following identity that the consistency between the two previous tensors depends on the choice of C_{s}. Hence, the relation known as the Germano identity:

$$L_{ij} = T_{ij} - \widehat{B}_{ij} = -\widehat{\overline{C_i}\overline{C_j}} + \widehat{\overline{C}}_i\widehat{\overline{C}}_j \tag{2.20}$$

The tensor L_{ij} represents the stress components of the scale motion between the test scale and the grid scale. These scales are referred to as the "test window" and can be explicitly evaluated. Furthermore, this evaluation can be compared to the Smagorinsky closure approximation by subtracting (2.18), where the test filter was applied from (2.19):

$$L_{ij} - \frac{1}{3}\delta_{ij}L_{kk} = 2C_{\mathrm{s}}M_{ij} \tag{2.21}$$

where

$$M_{ij} = \widehat{|\overline{S}|\overline{S}}_{ij} - \alpha^2 |\widehat{\overline{S}}|\widehat{\overline{S}}_{ij}, \quad \alpha \cong \frac{\widehat{\Delta}}{\Delta} = 2 \tag{2.22}$$

Equation (2.21) provides the value for C_{s} to insert in Eq. (2.18), but Eq. (2.21) represents five independent equations for a single unknown. Therefore C_{s} cannot be uniquely determined and an error minimization process is selected by using a least squares approach. C_{s} is thus obtained by the following equation:

$$C_{\mathrm{s}} = \frac{1}{2}\frac{\langle L_{ij}M_{ij}\rangle}{\langle M_{ij}M_{ij}\rangle} \tag{2.23}$$

where

$$L_{ij} = \left(\widehat{\overline{C}_i\overline{C}_j} - \widehat{\overline{C}}_i\widehat{\overline{C}}_j\right) - \frac{1}{3}\delta_{ij}\left(\widehat{\overline{C}_k\overline{C}_k} - \widehat{\overline{C}}_k\widehat{\overline{C}}_k\right) \tag{2.24}$$

Equation (2.23) differs in two manners from the original Germano model introduced below:

$$C_{\mathrm{s}} = \frac{1}{2}\frac{L_{ij}S_{ij}}{M_{ij}S_{ij}} \tag{2.25}$$

The first is that Germano multiplied Eq. (2.21) by S_{ij} to obtain the above equation. The issue is that the term $M_{ij}S_{ij}$ can vanish or becomes very small leading to unstable value of C_{s}. The second difference is the averaging process mandatory to ensure the computational stability. This avoids negative coefficient and prevents it from changing sharply.

Chapter 3

Numerical Tools

3.1 FrontFlow/blue

3.1.1 Numerical Code Structure

FrontFlow/Blue[1] is an open source Overset Finite Element code developed by the University of Tokyo, under the supervision of Professor Chisachi Kato, featuring Direct Numerical Simulation, DNS, Large Eddy Simulation, LES, and Reynolds Averaged Navier-Stokes, RANS. For LES computations, the static Smagorinsky turbulence model [57] as well as the dynamic version developed by Germano [16], where the Smagorinsky constant is determined locally in time and space using the modification of Lilly [37] are implemented. The computation of incompressible flows is performed using the fractional step method to solve the pressure Poisson equation with the Crank-Nicolson implicit time integration scheme. The resulting linear systems of equations are solved by the Biconjugate Gradient Stabilized method (Bi-CGSTAB) [61] incorporated with the residual cutting method [58]. Furthermore, the spatial and temporal discretization are both second-order accurate. To be able to handle large computational mesh, FFB is parallelized using the Message Passing Interface (MPI) library [17] for inter-domains communication and uses the METIS library [25] to decompose the computational domain into several sub-domains. The code structure of the flow computation is given in Fig. 3.1. FFB has also a multiple frame of reference implemented and uses an overset grid as interface. Regarding the grid, the solver version of FFB used for the present computations only computes flow using hexahedral element.

3.1.2 Numerical Code Performance on BlueGene/P

The performance of the numerical code on the supercomputer BlueGene/P has been investigated using the Hardware Performance Monitoring library provided by IBM. Such a library allows one to monitor, among others, the memory usage, the number of FLOP, the quantity of data read or written of the whole or parts of the numerical code. To monitor what parts of the code are the time consuming ones, the numerical code to compute the flow field for one time step can be decomposed as follow:

- Initial flow field development;

---

1. http://www.ciss.iis.u-tokyo.ac.jp/english/dl/

```
┌─────────────────────────────────┐
│    Computation Initialization   │
└─────────────────────────────────┘
                 │
┌─────────────────────────────────┐
│      Foregoing Computation      │
└─────────────────────────────────┘
                 │
┌─────────────────────────────────┐
│    Calculate fractional velocity│
└─────────────────────────────────┘
                 │
            RES ≤ EPS
               OR
           NITR ≥ NMAX
    FALSE ◄───◄◇►───► TRUE
                 │
┌─────────────────────────────────┐
│      Solve pressure equation    │
└─────────────────────────────────┘
                 │
            RES ≤ EPS
               OR
           NITR ≥ NMAX
    FALSE ◄───◄◇►───► TRUE
                 │
┌─────────────────────────────────┐
│     Velocity Field Correction   │
└─────────────────────────────────┘
                 │
┌─────────────────────────────────┐
│      Subsequent computation     │
└─────────────────────────────────┘
                 │
          DIVMAX ≥ DIVESC
               OR
          ITIME ≥ NTIME
    FALSE ◄───◄◇►───► TRUE
                 │
┌─────────────────────────────────┐
│    Computation Finalization     │
└─────────────────────────────────┘
```
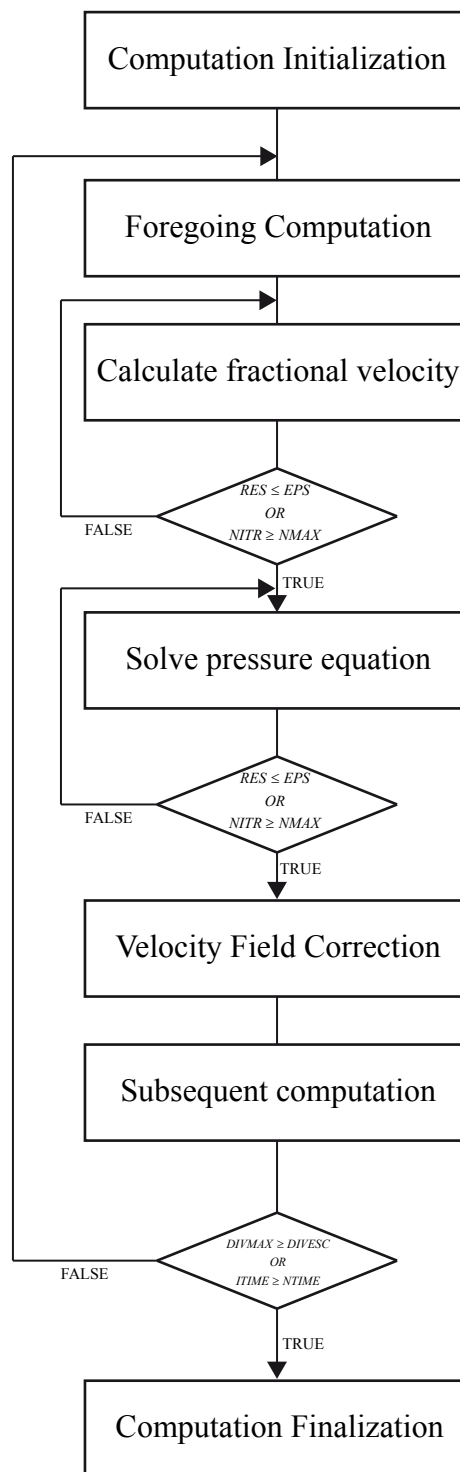
Figure 3.1: Flow computation algorithm.

- Overset grid compilation for parallel mode;
- Wall shear stress computation;
- Smagorinsky constant computation;
- Effective viscosity computation;
- Velocity computation;

- Pressure computation;
- Velocity field correction;
- Subsequent computations.

As the primary interest is in the computation of the velocity and the pressure fields, the analysis of the performance of the computation of the flow development, the overset grid computation, the wall shear stress computation, the element Smagorinsky constant computation and the element effective viscosity computation are merged into one analysis block called foregoing computation. The computation of the velocity, the pressure, the velocity correction and the subsequent computations compose each of the analysis block. The subsequent computations involve miscellaneous sub-block such as: the computation of the force acting on a specified body, the computation of the flow statistics and to save the data. As for the initial computation, these sub-blocks are merged into a single block. It results that the numerical code for the flow computation is decomposed into five distinct parts.

The analysis of the sustained performance of the numerical code is carried out by performing LES computations with the dynamic Smagorinsky turbulent model for the lid driven cavity flow [32]. The Reynolds number is 1,000 and the computational grid is decomposed into 512 subdomains with 0.1 million elements per subdomain. A subdomain is computed by a core. The lid driven cavity flow benchmark corresponds to a confined flow in a squared box with the lid moving at constant velocity in its plane. As the number of iterations required for the inner iterative solvers to converge changes, the convergence tolerance were set low enough to always impose 5 iterations for the velocity computation and 50 iterations for the pressure computation in this benchmark test. The computation of the pressure field requires more iterations than for the velocity field as the convergence rate is lower. The computation was performed for 100 time steps as it is estimated to be sufficient to obtain a statistically good representation of the time spent and the number of FLOP performed in each of these 5 blocks. The result of such a measurement is shown in Fig. 3.2 illustrating the time required for each block.
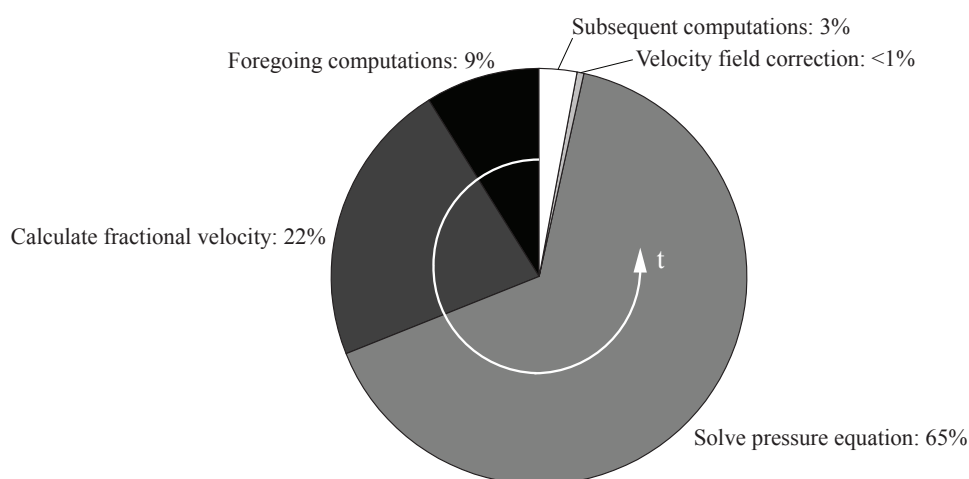
Figure 3.2: Pie chart showing the normalized time spent in each main part composing the computation of one time step.

As expected, the most time consuming block is the computation of the pressure, because 50 iterations were imposed whereas the number of iterations imposed for the

Table 3.1: Investigation of the time spent in the five main parts composing the computation of the flow field as well as the relative performance of the code with regards to the peak performance of the machine, which is 13.6 GFLOPS for a computing node.

	foregoing computation	Velocity computation	Pressure computation	Velocity correction	Subsequent computations
Elapsed time [s]	50.836	152.484	404.524	3.306	12.427
% of peak performance	5.69	5.82	5.34	4.82	1.01

computation of the velocity field was only 5 iterations as previously mentioned. However, such numbers of iterations are typical values for incompressible flow computation and only for the velocity computation a decrease to 2-3 iterations may be expected. During the computation, the number of FLOPS in each part were recorded, which permitted to compute the sustained performance presented in Table 3.1. As it can be seen, the relative performance is near 6% to the peak. This result is corresponding to the performances of other numerical codes optimized on massively parallel supercomputer and it is found satisfactory. Finally, this monitoring also permitted to evaluate the characteristics of FFB for the BlueGene/P, in term of the number of FLOP per element per time step, the memory requirement per element and the average sustained performance. These characteristics are given in Table 3.2.

To evaluate the behavior of FFB with regard to the number of cores used, a weak scaling analysis is performed using the lid driven cavity benchmark. The weak-scaling analysis increases the size of the computational domain in proportion to the number of cores so as to set a constant load for each core. This weak-scaling is performed for 1 to 8,192 cores (2,048 computing nodes) for the typical load of 0.1 million elements per core, requiring 74% of the main memory of one core. The averaged elapsed total time per a time step required for each computation is given in Figure 3.3; total elapsed time being defined as the sum of the computational time and the communication time. It should be noticed that with a half of the machine it is possible to have a computational domain near one billion elements. Furthermore, we can see that the total elapsed time per a time step slightly increases with respect to the number of cores. However, this increase is only 1.2 seconds when comparing the results for 1 and 8,192 cores which can be considered totally acceptable from a practical point of view.

3.1.3   Stationary and Rotating Interface

The interface between the rotating and the stationary meshes are done using an overset mesh [26]. As illustrated in Fig. 3.4, the idea is that each mesh includes an appropriate

Table 3.2: FFB characteristics on BlueGene/P.

Number of FLOP per element per time step	Memory requirement per element	Sustained performance
22,600	7.4kB	5.3%
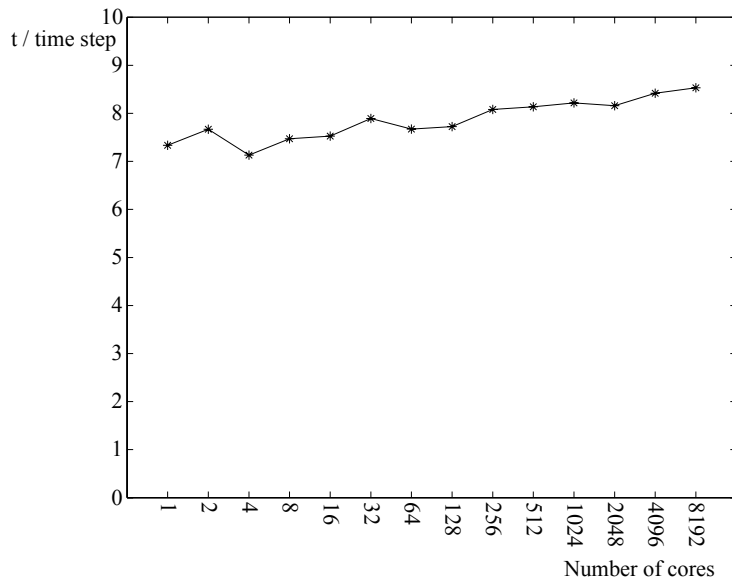
Figure 3.3: FFB7 weak-scaling benchmark up to 8,192 cores for a load per a core of 0.1 million elements on BlueGene/P.

margin, which overlaps with its neighboring mesh upstream and downstream. At each time step, the velocity components and the static pressure in the overlap region are interpolated from the neighboring mesh with element tri-linear interpolation function [19]. For the specific case of turbomachinery, a dual frame of reference is used to compute flows in the stationary and the rotating mesh. Therefore, when the velocity field between the rotating and the stationary meshes are overset, a transformation is applied in order to take into account the difference of the two different frames of reference. In the case of the fractional-step method, where the velocity and the pressure are computed successively, the velocity field is first overset. Secondly, the pressure gradient is overset in the inner iteration of matrix solver poisson equation. Finally, the static pressure is overset [19].

As the mass balance through the interface is not exactly guaranteed due to the interpolation in the overset interface, it may lead to nonphysical oscillation of the pressure field. To handle this issue, two approaches are used and implemented. The first approach is to accept small mass imbalance at the overset by using the low Mach number assumption. This assumption let an incompressible flow have a small compressibility, which then become compatible with the small mass imbalance. The second approach is to impose the mass balance at the overset by using the mass imbalance correction (hereafter denoted as MIC) [65]. Therefore, with the inconsistency generated by the mass imbalance being removed, the pressure solver does not exhibit nonphysical oscillation [19]. Furthermore, it is worth to mention that the overset does not affect the pressure field.

3.2 Computing Resources

3.2.1 IBM BladeCenter

The first type of computing architecture used is the local cluster implemented in the Laboratory for Hydraulic Machines, composed of two IBM BladeCenter [12]. The first
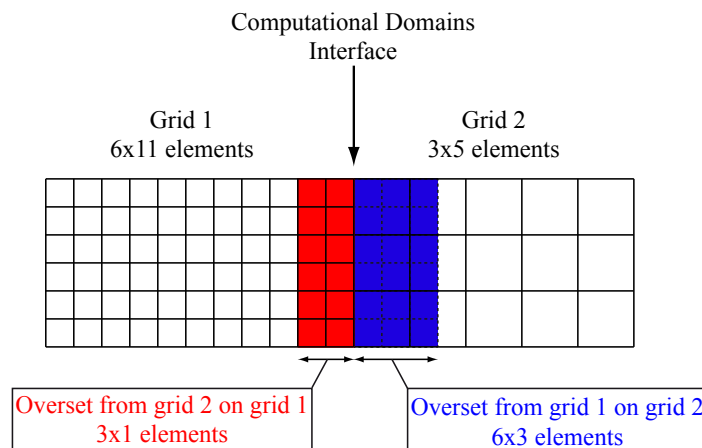
Figure 3.4: Overset scheme of two neighboring meshes.

BladeCenter is composed of 8 computing nodes, each of which has a bi-processor quad core Intel Xeon CPU X5570 (Gainstown) operated at 2.93 GHz (64 cores in total). The memory cache is 8 MB of L3 and each node processes 32 GB of DDR3 memory operated at 1333 MHz.

The second BladeCenter is composed of 12 computing nodes, each of which has a bi-processor quad core Intel Xeon CPU E5450 (Harpertown) operated at 3 GHz (96 cores in total). The memory cache is 12 MB of L2 and each node processes 8 GB of DDR3 memory operated at 1066 MHz.

The interconnection is composed of a Gigabit Ethernet, that is, a bandwidth up to 1 Gbps.

3.2.2   Blue Gene/P

The second type of computing architecture used is the CADMOS IBM Blue Gene/P supercomputer [22]. This supercomputer is a specific machine designed for massively parallel simulations, featuring a total of 16,384 cores. A unit of such a machine is called a rack. The packaging hierarchy of a BlueGene/P from the rack size to a single core is as follow. A rack accommodates two Midplanes containing 16 node cards. These node cards consist in the assembly of 32 nodes containing two CPUs (two processors) with two cores. That results in a total of 4 cores per computing node, i.e. a total of 4,096 cores per rack. One core corresponds to a PowerPC 450, running at 850 MHz and thanks to the dual-pipeline FPU, floating-point unit, it can simultaneously execute two fused multiply-add instructions per a machine cycle. This gives a peak performance of 4 floating-point operations (FLOP) per a machine cycle per core. Thus, the peak performance of a node is 13.6 billion floating-point operations pre second (GFLOPS). The CADMOS BlueGene/P is composed of 4 racks providing a peak performance of 56 TFLOPS with 16 TB of memory available.

The computing nodes are interconnected by a 3D torus network with a node-to-node bandwidth of 2 times (bidirectional) 3.4 GB/s in each direction.

Table 3.3: Blue Gene/P specification.

	BG/P
CPU Name	PowerPC 450
Cores/Node	4 cores (@0.85GHz)
Performance	13.6 GFLOPS
Cache	2xL3 4MB
Node configuration	1 CPU/Node
Memory capacity	4 GB
Number of nodes/rack	1,024
Number of rack	4
Rack peak performance	14 TFLOPS

3.2.3   FX10 - K Supercomputer

The third and fourth types of computing architectures are the PRIMEHPC FX10 and the K supercomputers. These supercomputers share the same architecture except that the PRIMEHPC FX10 is equipped with the new CPU generation of SPARC64 IXfx, whereas the K supercomputer is equipped with the SPARC64 VIIIfx. The SPARC64 IXfx is composed of 16 cores running at 1.848 GHz with 12MB of L2 cache, whereas the SPARC64 VIIIfx is composed of 8 cores running at 2 GHz with 6MB of L2 cache. Furthermore, these two CPU can perform 8 FLOP per machine cycle [15]. Regarding the packaging, the approach is similar to the one previously introduced. A rack is composed of 24 system boards, each with 4 nodes. Therefore, a rack features 96 nodes. The peak performance of a rack is 22.7 TFLOPS for the PRIMEHPC FX10 supercomputer and 12.3 TFLOPS for the K supercomputer.

The computing nodes are interconnected by a 6D torus network with a node-to-node bandwidth of 2 times (bidirectional) 5 GB/s in each direction.

Table 3.4: PRIMEHPC FX10 and K supercomputers specifications.

	FX10	K
CPU Name	SPARC64 IXfx	SPARC64 VIIIfx
Cores/Node	16 cores (@1.848GHz)	8 cores (@2GHz)
Performance	23.5 GFLOPS	128 GFLOPS
Cache	L2 12MB	L2 6MB
Node configuration	1 CPU/Node	1 CPU/Node
Memory capacity	32 GB	16 GB
Number of nodes/rack	96	96
Number of rack	50	864
Rack peak performance	22.7 TFLOPS	12.3 TFLOPS

3.3   VisIt

3.3.1   File Format

VisIt is an open source software developed by the Lawrence Livermore National Laboratory (LLNL) [2] to interactively visualize and analyse scientific data in serial or parallel mode. Furthermore, VisIt offers the advantage to leverage both the use of a remote parallel computer and the use of a local workstation, which has graphics acceleration hardware. Besides, such an approach is more natural since in most cases the scientific data are stored on a remote machine. Therefore, there is no need to transfer the data for analyses.

Regarding the file format, VisIt has a wide range of readers implemented to read data coming from different database. The default file format name of VisIt is "Silo". Silo is a C-language library with a well-defined application programming interface (API) allowing the user to write all kind of data to a Silo file. The Silo library is architecturally divided into an upper-level API and a lower-level I/O implementation called driver. There are several choices regarding these drivers, but the two main ones are the HDF5 (Hierarchical Data Format 5) and the PDB (Portable Data Base) drivers. For the utility program converting the data from a FFB database to a Silo database, the PDB driver was selected. The advantages using this file format are that it allows to store the data in binary format and that it is platform independent.

3.3.2   Parallelized Visualization

As the computational mesh increases, the data to load for visualization increases accordingly. Therefore, the visualization using a single CPU is no longer feasible and requires a parallel visualization to distribute the data among several CPUs. This is easily achieved with VisIt by compiling a parallel executable. Regarding how to handle the data to load in VisIt, two approaches may be used.
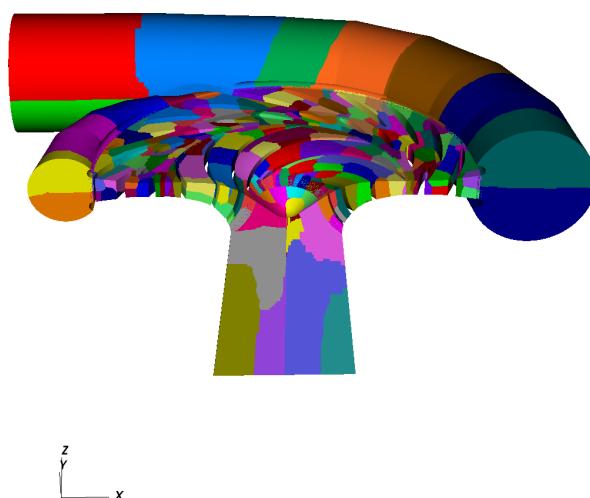
Figure 3.5: Illustration of the half Pump-turbine domain decomposed into 512 subdomains.

---

2. `https://wci.llnl.gov/codes/visit/`

The first consists in converting each partitioned flow data from the simulation to a Silo file format and to generate a specific file, called master file. The master file is generated using also the Silo library and works like an assembly file. It means that VisIt will know which data to read in in order to visualize the full computational domain. Such an assembly is illustrated in Fig. 3.5, where the computational domain of the pump-turbine is decomposed into 512 subdomains. Furthermore, for scalability purposes, this master file contains the spatial and the variables extents, which allows, when plotting a slice, an iso-surface or anything else to load only the subdomains containing the data to visualize. Therefore, avoiding to load all the data to retrieve only the one of interest.

The second approach consists in merging the partitioned flow data to built a single file containing the flow data of the full computational domain. This merge is nevertheless sometimes not feasible, when the data size is too large. But, on the other hand this approach may be appropriate when the data are analyzed on a machine with several CPUs and a sufficient amount of RAM memory. In that case, it is preferable to reduce the number of files to the minimum, as the demand for the file I/O degrades drastically the efficiency of VisIt.

Chapter 4

HYDRODYNA Pump-Turbine

4.1 Pump-Turbine Characteristics

The reduced scale model HYDRODYNA pump-turbine is depicted in Fig. 4.1 with its specifications given in Table 4.1.

Table 4.1: Specifications of the HYDRODYNA pump-turbine scale model.

ν	Specific speed	0.19
z_{b}	Number of impeller blades	9
z_{o}	Number of guide vanes	20
$D_{1\mathrm{e}}$	Outer impeller diameter	523.5 mm
$D_{\bar{1}\mathrm{e}}$	Inner impeller diameter	250 mm
b	Guide vane width	36 mm
α_{gv}	Guide vane opening angle	20°
$R_{2\mathrm{e}} - R_{1\mathrm{e}}$	Impeller-diffuser radial gap	25 mm
$(R_{2\mathrm{e}} - R_{1\mathrm{e}})/R_{1\mathrm{e}}$	Impeller-diffuser relative gap	9.5%

Two measurement campaigns were carried out in 2006 and 2008 to establish the pump-turbine performances in pumping and generating modes. For the first campaign, an instrumented impeller was used with 30 pressure sensors mounted. For the second campaign, a plain impeller was used to avoid any damage to the instrumented impeller during off-design investigations in generating mode. The resulting performance measurements are shown in Fig. 4.2, where the specific energy and the scaled efficiency are plotted against the discharge. It can be seen that the specific energy curves do not exhibit the expected monotonic behavior. Near a discharge coefficient of φ=0.021 and φ=0.026 the slopes become positive, which indicates the presence of instabilities within the machine. For this specific machine it was shown that this instability is associated with the rotating stall phenomenon.

4.1.1 Former Research on the Pump-Turbine

The internal flow of the HYDRODYNA pump-turbine reduced scaled model has been investigated, both in generating and pumping modes. This pump-turbine was installed in one of the three EPFL-LMH hydraulic machines testing facilities. Such a test facility is
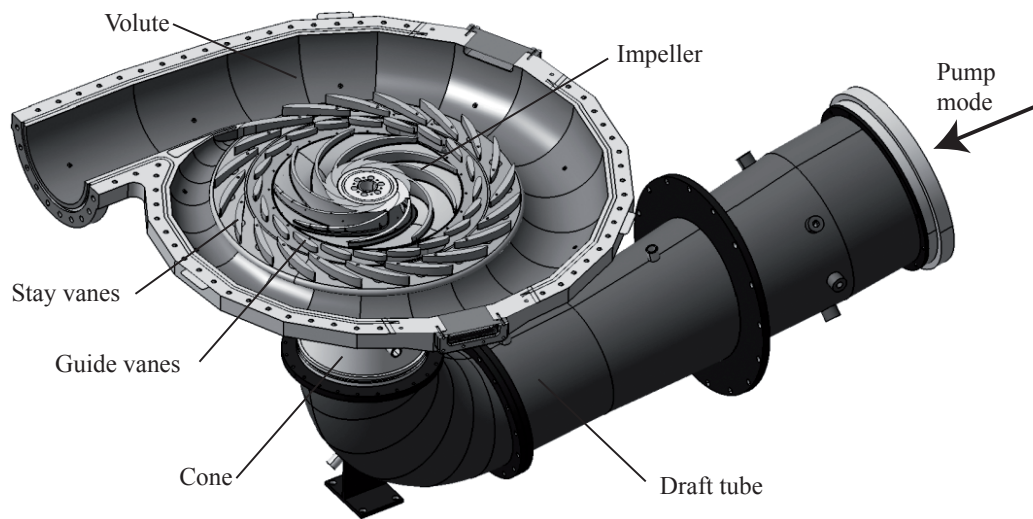
Figure 4.1: Pump-turbine main components.

illustrated in Fig. 4.3 showing the PF2 test rig. The maximum specific energy achievable is E=1,250 J·kg^{-1}, the maximum rotational velocity is N=2,500 rpm and the maximum discharge is Q=1.4 m^3·s^{-1}. The relative error of the discharge, the shaft torque and the differential pressure measurements are within 0.2%. The flow within the closed loop is driven by a single circulating pump coupled to a 1,000 kW electrical motor and the pump-turbine is coupled to a 300 kW electrical generator.
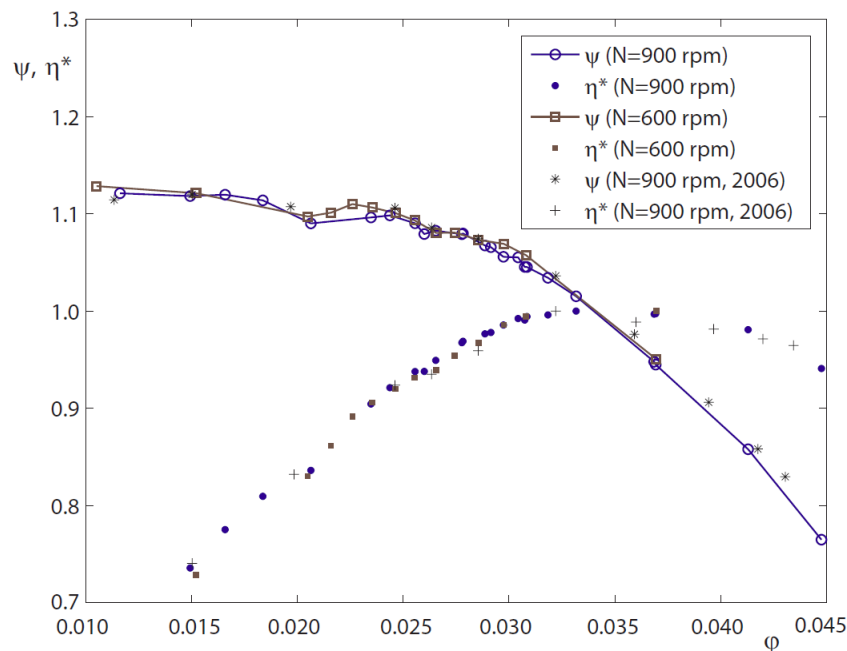
Figure 4.2: Specific energy and efficiency scaled by the efficiency at BEP versus discharge of the HYDRODYNA pump-turbine. Instrumented impeller (2006) and plain impeller (2008), N=600 rpm and N=900 rpm. Data obtained from [3]
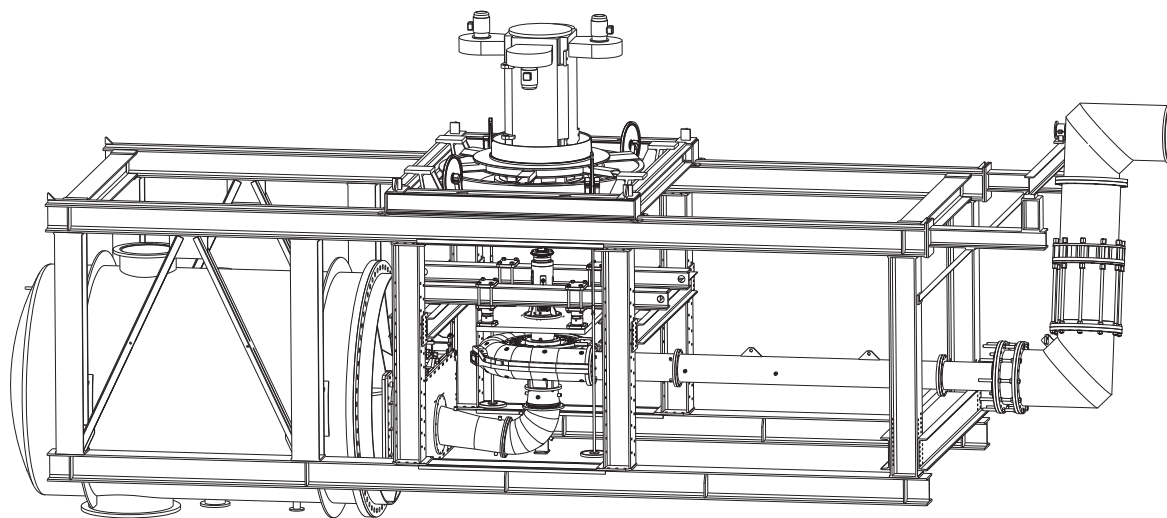
Figure 4.3: EPFL LMH PF2 test rig.

Four former studies were dedicated to study different phenomena related to this specific pump-turbine. One study was dedicated to the investigation of the pump-turbine in pumping mode and the other three studies are dedicated to the investigations of the pump-turbine in generating mode.

The first research was performed by Dr. A. Zobeiri [66]. He studied numerically and experimentally the Rotor Stator Interaction (RSI) in generating mode for three different conditions: part load, best efficiency and full load. This research identified the origin of the high pressure fluctuations and their impact on the structure of the different component of the machine.

The second research was performed by Dr. O. Braun [3]. He studied experimentally and numerically the internal flow in the diffuser in pumping mode at part load condition. This research quantitatively and qualitatively described the rotating stall occurring in the vaned diffuser.

The third research was performed by Dr. Hasmatuchi [20]. He studied experimentally and numerically the internal flow field in generating mode. This research describes how the flow field evolves within the impeller when operating the pump in the so-called "S-shape".

The fourth research was performed by Dr. Roth [49]. He studied experimentally the high periodic excitation due to the RSI on the pump-turbine guide vanes. This research elaborates a model to predict the dynamic behaviour of the entire guide vane cascade.

4.2   Flow Domain Discretization

4.2.1   Process

The spatial discretization of the pump-turbine was performed using the commercial software ANSYS ICEM CFD (ANalysis SYStem; Integrated Computer-aided Engineering and Manufacturing; Computational Fluid Dynamics). This software is very powerful as it gives a means to fully control the build of the mesh down to the very small detail. This

Figure 4.4: a) Wire-frame representation of the cone geometry. The cyan curves represent the physical limits of the cone and the grey curves represent the overset limits. The dashed grey lines represent the outer limits of the overset. b) Cone blocking. Using the rotational symmetry only 1/9 of the volume is blocked.

full control is achieved by the generation of the so called blocking. This blocking can be seen as a decomposition of the geometrical volume (i.e, here the volume of water in the machine) into multiple smaller volumes, called "block". These blocks are primordial, as they, on one side, represent the geometry and on the other side represent the mesh topology. To represent the geometry, each block has to be associated to the geometry. Typically, a block is represented by vertices, edges and faces, and they are associated with the geometry represented by points, curves and surfaces. Furthermore, this process of generating small blocks and mapping them to the geometry, gives the liberty to choose the kind of mesh topology, e.g., C-mesh, H-mesh or O-mesh. Once the topology is mapped, it remains to set the number of nodes on edges as well as the nodes distributions along each edge. This is very powerful, as it allows to have, for example, a high node density near walls and decrease the node density away from the wall, reducing the total amount of the nodes. Once all these operations are preformed, the computational mesh can be generated and exported.

4.2.2   Blocking

As shortly introduced previously, the mesh generation requires several steps, which can be time consuming and lead to extremely complex blocking. In order to simplify the blocking process, the geometry of the full pump-turbine is first decomposed into four distinctive parts: the cone, the impeller, the diffuser and the volute. Each of these parts are meshed separately and are assembled together using the overset capability introduced in section 3.1.3.

Cone

The cone is the upstream most component of the pump-turbine in pumping mode as it connects the inflow to the impeller. Its wire-frame geometry is depicted in Fig. 4.4 a). The physical limits of the cone correspond to the cyan curves, whereas the grey curves represent the overset limits. The overset surfaces here are the interface between the stationary cone and the rotating impeller. As the geometry has a rotational symmetry, the total volume to mesh could be simplified and only 1/9 of the cone was manually meshed. The corresponding blocking is depicted in Fig. 4.4 b). The resulting mesh features 6.7 million elements and 7 million nodes (including the overset).

Impeller

The impeller is the second (rotating) component of the pump-turbine. Its wire-frame geometry is depicted in Fig. 4.5 a). The physical limits of the impeller correspond to the cyan curves, whereas the grey curves represent the overset limits. The overset surfaces here are the interface between the stationary cone and the rotating impeller and the interface between the stationary diffuser and the rotating impeller. Since the impeller possess a rotational symmetry, only one impeller channel is blocked and is depicted in Fig. 4.5 b). The resulting mesh features 41 million elements and 42 million nodes (including the overset).
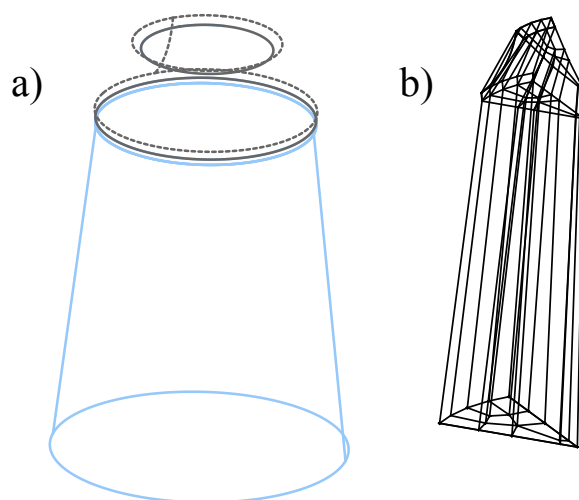

Figure 4.5: a) Wire-frame representation of the impeller geometry. The cyan curves represent the physical limits of the impeller and the grey curves represent the overset limits. The dashed grey lines represent the outer limits of the overset. b) Impeller single channel blocking.

Diffuser

The diffuser is the third component of the pump-turbine. As known, such a component has no rotational symmetry because of the presence of the tongue. Downstream of the tongue, which is in the counterclockwise direction, see Fig. 4.1, there are a smaller stay

vane and the tip part of the volute, both of which contribute to the non-symmetry of the diffuser. The choice to integrate the tip part of the volute into the diffuser part was made firstly due to the fact that the mesh has to be fully composed of hexahedral elements. Secondly, without this integration, the blocking in the tip of the volute would be catastrophic and lead to totaly deteriorated elements, which is not affordable. Consequently, in order to simplify the diffuser blocking, three diffuser channels were isolated as shown in Fig. 4.7 a), which include the three non-symmetric elements (tongue, smaller stay vane and volute tip). For the remaining 17 diffuser channels, the rotational symmetry was used, resulting in the blocking of only one single channel as shown in Fig. 4.6 b). In this case, the assembly of the two meshes will not be performed via an overset interface. Thus, the blocking and the node distribution has to be identical between those two meshes. The areas in common are depicted in Fig. 4.6 b) and Fig. 4.7 b) by red surfaces. As previously mentioned, the physical limits of the diffuser surfaces correspond to the cyan curves, whereas the grey curves represent the overset surfaces limits. The overset surfaces here are the interface between the the rotating impeller and the stationary diffuser and the interface between the stationary diffuser and the stationary volute.

After the generation and the merge of the two meshes, the resulting diffuser mesh features 73 million elements and 76 million nodes (including the overset).
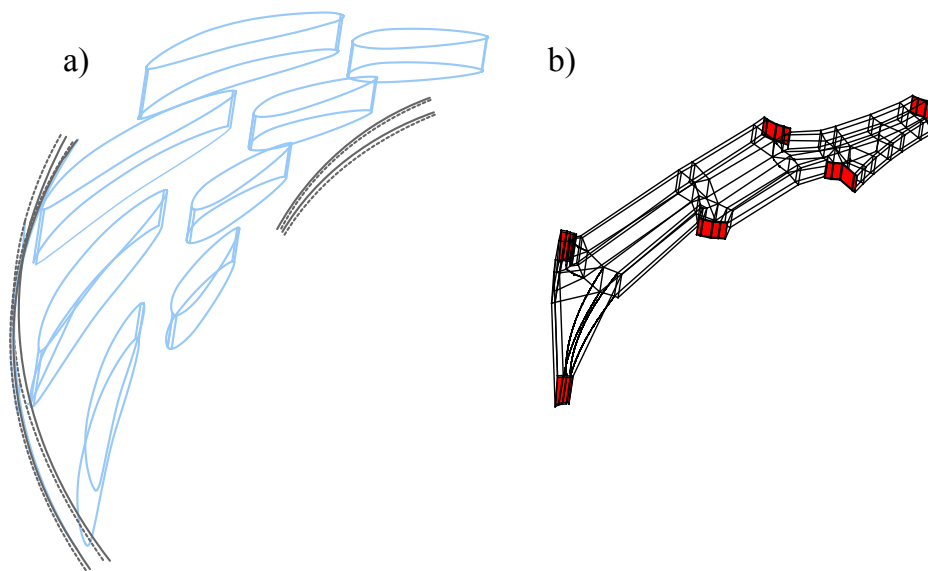
Figure 4.6: a) Wire-frame representation of the diffuser channel geometry (symmetric part). The cyan curves represent the physical limits of the diffuser channel and the grey curves represent the overset limits. The dashed grey lines represent the outer limits of the overset. b) Diffuser single channel blocking.

Volute

The last component of the pump-turbine is the volute, whose symmetrical wire-frame geometry is depicted in Fig. 4.8 a). The physical limit of the volute correspond to the cyan curves, whereas the grey curves represent the overset limits. The overset surfaces
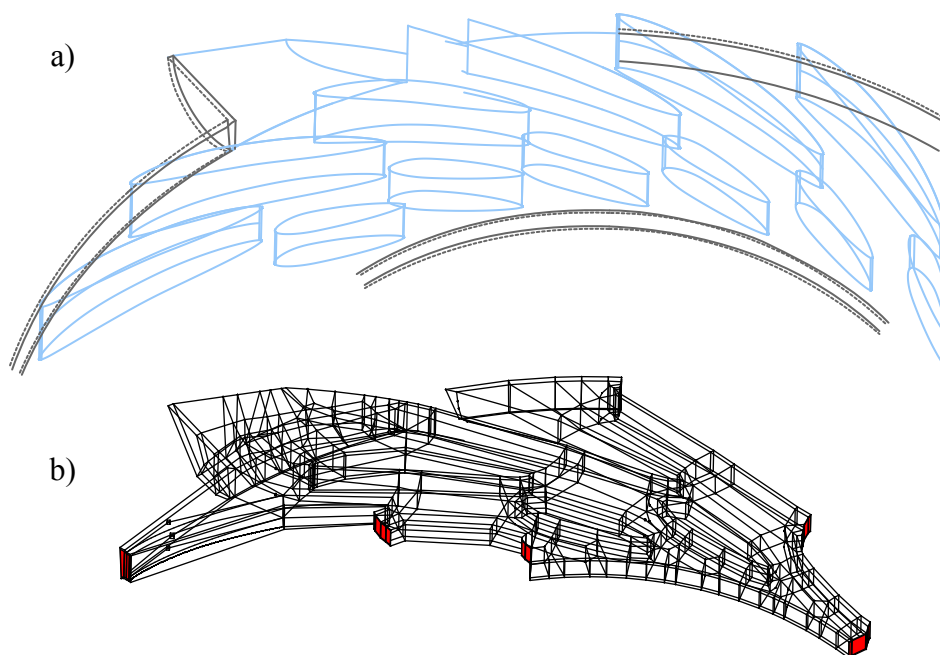
Figure 4.7: a) Wire-frame representation of the diffuser channels geometry around the tongue (nonsymmetric part). The cyan curves represent the physical limits of the diffuser and the grey curves represent the overset limits. The dashed grey lines represent the outer limits of the overset. b) 3 nonsymmetric diffuser channels blocking.

here are the interface between the stationary diffuser and the stationary volute. As the geometry has a plane symmetry, the total volume to mesh can be simplified and only half the volute was manually meshed. The corresponding blocking is depicted in Fig. 4.8 b). The resulting volute mesh features 7.8 million elements and 8.1 million nodes (including the overset).
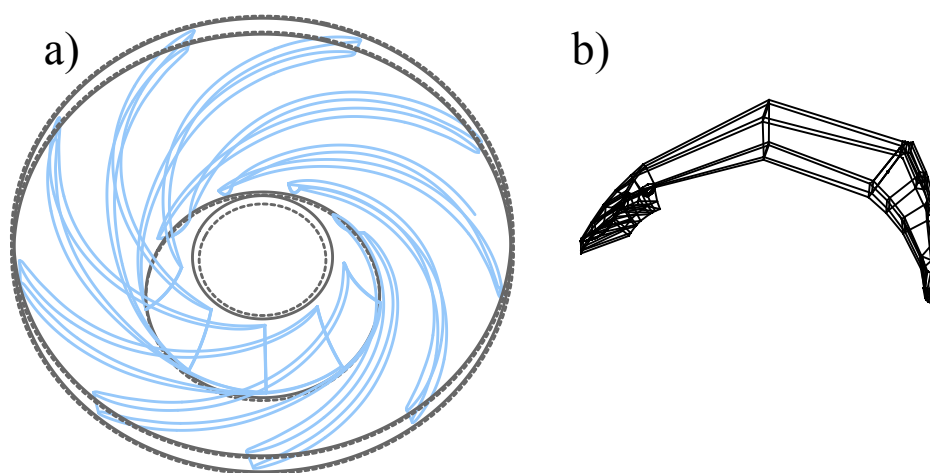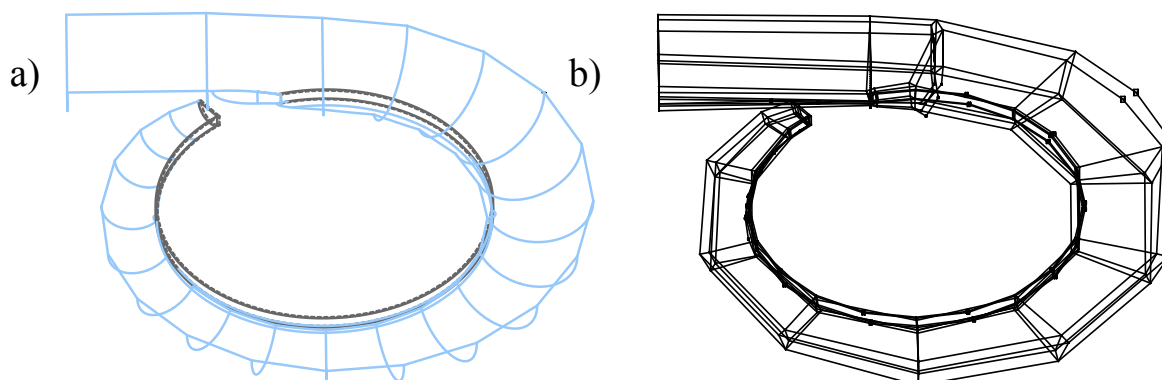

Figure 4.8: a) Wire-frame representation of the volute geometry. The cyan curves represent the physical limits of the volute and the grey curves represent the overset limits. The dashed grey lines represent the outer limits of the overset. b) Volute blocking.

Table 4.2: Number of nodes and elements for each component of the pump-turbine.

Pump-Turbine Part	Number of nodes 10^6	Number of elements 10^6	Ratio of the global mesh %
Cone	7.00	6.76	5.23
Impeller	42.45	41.44	32.02
Diffuser	76.15	73.36	56.70
Volute	8.11	7.82	6.05
Total	133.73	129.40	

Pump-turbine

Table 4.2 summarizes the size of the mesh for each different component. The total number of the elements reached 129 million elements, which fits the 130 millions estimated in the previous chapter. The generated mesh is shown in Fig. 4.9.

Mesh Quality

There exist several criteria to check the quality of a mesh and ICEM offers more than 35 criteria. However, it is estimated that only three criteria are sufficient to quantify the mesh quality. These criteria are the equiangle skewness, the volume change and the aspect ratio. The equiangle skewness is a measure regarding how an element is distorted. The volume change indicates how the volume evolves between an element and its neighboring elements. Finally, the aspect ratio measures how elongated an element is.
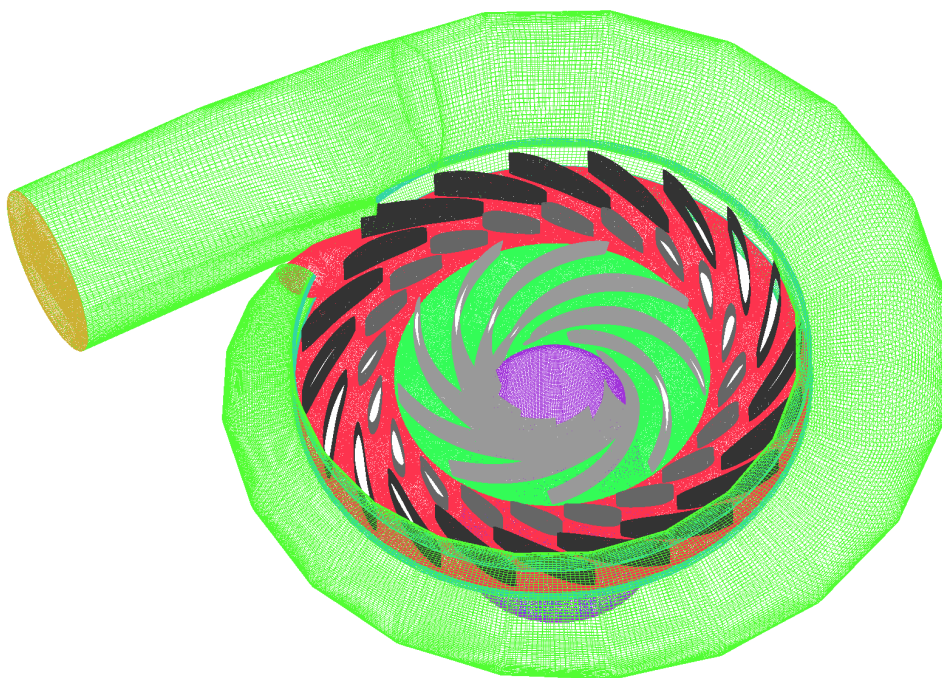
Figure 4.9: Spatial discretization of the pump-turbine.

Figure 4.10: Mesh quality quantification using the equiangle skewness criterion. The bars give the criteria distribution for each mesh in percentage.

Equiangle Skewness

The equiangle skewness criterion takes a value between 0 and 1 where 0 represents a completely "flat" hexahedral element and 1 represents the perfect element with all angles equal to 90 degrees. The definition of the equiangle skewness criterion is as follow:

$$\text{skew} = 1.0 - \max((Q_{\max} - Q_e)/(180 - Q_e), (Q_e - Q_{\min})/Q_e)$$

where $Q_{\max}$ is the largest angle between two neighboring sides in the element, $Q_{\min}$ is the smallest angle in the element and Q_e is the angle of an equiangular element (e.g., 90 degrees for a square).

Figure 4.10 shows the distributions of the equiangle skewness criterion for the different pump-turbine components. The ordinate gives the number of elements, expressed in percentage regarding the total number of elements in the individual component. As it can be seen, the majority of the elements possess a value higher than 0.5. This tendency is confirmed by high averaged values, which are approximately 0.8, confirming the good quality of the meshes. It can also be noted that the criterion distribution for the impeller does not follow the same tendency as the three other meshes. This can be explained by the characteristic complexity of the impeller geometry with high curvatures. Because the mesh has to fit closely the geometry, it induces mesh curvatures in both the streamwise and the spanwise direction, explaining the above mentioned difference.

The worst equiangle skewness qualities are located in the diffuser and the volute components. These components also possess complex geometry to be discretized, consisting mainly in sharp edges. The consequences are that the blocking has to be built in accordance to these sharp edges, inducing non regular blocking with bad shaped elements.

Volume Change

This quality metric is calculated for the individual element by finding the maximum volume of its neighboring elements and dividing it by the volume of the element itself. In

an area with important flow structure this metric should not exceed 1.2. Elsewhere where the flow does not change significantly, this metric could be relaxed to values higher than 1.2. However, it is preferable to keep this metric within the range 1.1-1.2.

Figure 4.11 shows the distribution of the volume change criterion for each mesh. For visualization purpose, only the range between 1 to 2 is shown as it contained the majority of the elements. Near walls, the expansion ratio is set to 1.1, whereas it is set to 1.2 elsewhere. However, it is not possible to meet the prescribed expansion ratio because it resulted in the increase of the number of nodes, which was sometimes not affordable. This constraint explains why the average values are slightly above 1.2.

The maxima shows that in some cases the expansion ratio reaches 25 or even 37, which should be avoided. Because all the settings are set manually, some of them may have been missed and may explain such a high ratio.
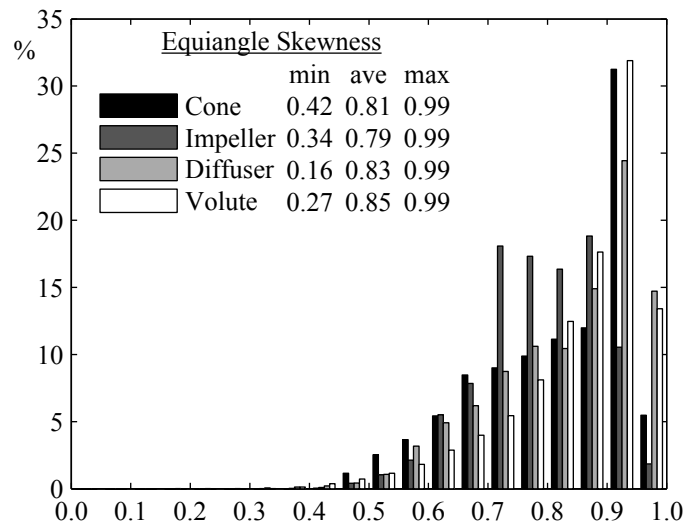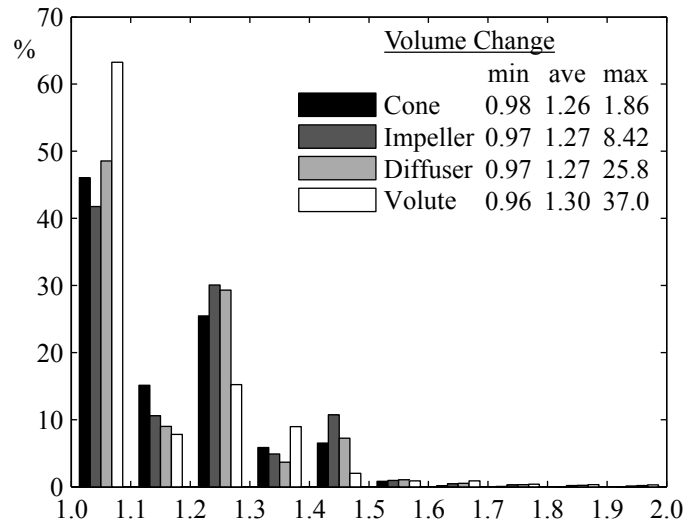

Figure 4.11: Mesh quality quantification using the volume change criterion. The bars give the criteria distributions for each mesh in percentage.

Aspect Ratio

For hexahedral elements, the aspect ratio is defined as the size of the maximum element edge divided by the size of the minimum element edge.

Figure 4.12 depicts the distributions of the aspect ratio for each mesh in the range 1-20. Except the volute which contains the majority of its elements in the range 1-3, other components contain only about 30% of their elements in this range. This is confirmed by an average value for the volute, which is 2-3 times smaller than in the other components. One reason is that, for the volute component, the discretization near walls to capture the boundary layer was not taken into account. A mesh refinement was still carried out near walls in this component, but it is not as fine as in other components.

The necessity to refine the mesh near the wall always induces high aspect ratio elements as it is not affordable to have an equivalent size in the wall normal direction, spanwise and streamwise directions. For this reason, due to the particular discretization of the

boundary layer, elements with high aspect ratio up to 100 are present in the impeller and diffuser components.
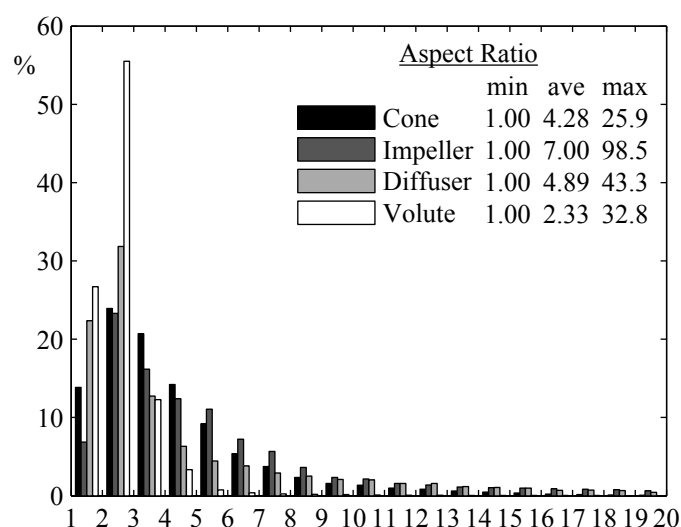
Figure 4.12: Mesh quality quantification using the aspect ratio criterion. The bars give the criteria distributions for each mesh in percentage.

4.2.3 Overset Discretization

As presented in section 3.1.3, the interface between meshes is done using an oversetting approach. Thus, for each mesh to be connected to another mesh, the geometry was modified in order to incorporate the geometry of the neighboring component to build the topology of the overset volume. Figures 4.4 a), 4.5 a), 4.6 a) and 4.8 a) (see pages 36-39) showed the result of such expansion by the grey surfaces. Table 4.3 gives the size of each overset volume in term of number of elements. In the present mesh, there are three interfaces, which are the interface between the cone and the impeller, between the impeller and the diffuser and finally between the diffuser and the volute. Since the overset process is bidirectional, it results that for each interface, two overset area are required, and hence Table 4.3 has six entries. As it can be seen, each overset volume are composed of several layers between six and ten. For an optimal use of the overset approach, it is often required to set a ten layers overset. However, because of geometrical constraint, e.g. the presence of a wall, it was not always possible to extend the overset as far as it should be. Furthermore, another determining constraint is the size of each element. One example is the overset between the diffuser and the volute. The interface between the two components is located near the trailing edge of the stay vanes, where the mesh is fine in order to capture the physics near the wall. However, the volute exhibits the larger volume to be discretized, thus large elements are required in order for the number of elements to be acceptable. It results then, that the two overset area will present different element density and that according to the limitation in elements volume change, it will not be possible to achieve ten elements within the overset volume. This constraint explains the difference in mesh density for the interfaces between the cone and the impeller and between the diffuser and the volute. In both cases, the ratio is about one-third.

Table 4.3: Number of layers and number of elements for each overset. The third column gives the ratio expressed in % of the overset mesh size regarding the component mesh size, which include the overset.

Pump-Turbine Component	Number of layers	Number of elements	% to global mesh
Cone on Impeller	10	414,000	6.12%
Impeller on Cone	9	1,595,000	3.85%
Impeller on Diffuser	7	1,341,000	3.24%
Diffuser on Impeller	7	1,710,000	2.33%
Diffuser on Volute	6	1,502,000	2.05%
Volute on Diffuser	6	547,000	7.00%
Total	-	7,112,000	5.50%

The third column in Table 4.3 gives the proportion of the overset in term of the number of the component mesh elements, which includes the overset elements. As it can be seen, the overset features 7 million elements, which corresponds to 5.5% of the full pump-turbine mesh. This quantity could be considered as a significant increase. However, when performing large-scale computations involving a large number of cores, i.e. 2048, such a quantity of added elements is acceptable and it corresponds to only a few thousand elements added per sub-domain.

4.3   Computation Parameters & Flow initialization

The flow computation of a full pump-turbine reduced scale model by the Large Eddy Simulation for a high Reynolds number requires a fine temporal and spatial discretization to capture all the relevant turbulent structures within the flow. For these discretizations, the necessary computing power resources can be very high and the allocation of these resources can be long. In order to save time and computing resources, the flow initialization is performed using a coarse mesh, featuring 85 million elements by down scaling the mesh introduced in section 4.2, and one impeller revolution discretized by 10,000 time steps. With such a spatial and temporal discretization, the computation of one impeller revolution using 2,048 cores can be performed in less than 7 hours on the FX10 supercomputer.

4.3.1   Numerical Setup

The execution of the unsteady flow computations requires several settings, such as the choice of a turbulence model, the numerical scheme and some settings specific to the start of a computation in order to avoid numerical instabilities. FFB gives two choices for the turbulence model: the static and the dynamic Smagorinsky turbulence models. As it is known that the Smagorinsky model tends to be too dissipative [36], the dynamic Smagorinsky model is chosen with the no-slip condition at the walls. The presence of the overset interfaces in the mesh requires specific settings to avoid the above mentioned issues regarding the mass imbalance at the interface. Therefore, the Fractional Step method with the low Mach number assumption is selected. The setting of the low Mach number is done via a parameter called FSMACH which is the inverse of the numerical

speed of sound: $1/a$. Using the definition of the Mach number: $Ma=C/a$, where C is a characteristic velocity, the parameter FSMACH becomes the ration of Ma/C and Ma and C are respectively set to 0.1 and 4.1135 m/s which is the peripheral speed of the impeller. However, in some computations the low Mach assumption may not be sufficient, especially at the early phase of the computation, and it brings about the mass imbalance issue. Such a situation was encountered during the start of the present computation and was solved by using a specific function (MIC) imposing the mass balance at the overset interfaces. Such a function has been used during the computation of the first 33 impeller revolutions. Finally, the last setting concerns the overset between the rotating and the stationary components. In this situation, the overset area attached to the impeller rotates with time and the corresponding overlapping region between the rotating and stationary parts has to be updated. In order to save time without loosing the accuracy, the overlapping is updated at every 4 time steps.

FFB requires the choice of a temporal numerical scheme and weighting functions for the elements. For an accurate computation, the Crank-Nicolson scheme with the standard Galerkin method are chosen, which results in a second order accuracy both in time and space.

Finally, to compute the flow corresponding to the part load condition φ=0.026, the inlet uniform velocity and the impeller rotational speed have been set respectively to 2.57 m/s and 15.708 rad/s.

Table 4.4: Summary of the computation parameters.

Re	Reynolds number	$1.1 \cdot 10^6$
ν	Kinematic viscosity	10^{-6} m^2/s
φ	Flow coefficient	0.026
ω_n	Impeller rotational speed	15.708 rad/s
C_{in}	Inlet velocity	$2.57 \cdot 10^{-1}$ m/s

Computation Initialization

The start of a computation can lead to numerical instabilities as the flow undergoes a sudden change at boundaries. To prevent such an instabilities from occurring, it is common to use functions which gradually increase the boundary values. Therefore, the inlet uniform velocity and the impeller rotational speed were exponentially increased from 0 to their steady values during the computation of the first impeller revolution. Moreover, to prevent unphysical pressure fluctuation from taking place associated with the RSI, no overset update were carried out during the first 5 impeller revolutions (i.e. static oversetting mode was set).

In the following, all the results shown were obtained using the University of Tokyo Supercomputer PRIMEHPC FX10.

4.3.2 Computation Convergence

The convergence of a computation to a steady, a cyclic or a statistically steady solution can be demanding, especially for large computational domains and a small time step. To estimate the required number of impeller revolutions to obtain a fully developed flow field, one can compute the number of impeller revolutions necessary to renew the flow within the full pump-turbine. Table 4.5 gives the volume of each components of the pump-turbine with the estimation of the number of impeller revolutions required for all initial fluid particle present in the individual pump-turbine component to exit from it. As it can be seen, the computation of 25 impeller revolutions would be required to completely renew the initial fluid present in the machine, which is too huge for an initialization as it would need the use of 358,400 CPU hours. However, the components of interest are the impeller and the diffuser, which are the two smallest volumetric components of the pump-turbine, respectively 5% and 7%. Therefore, the required number of impeller revolutions to renew the flow within these components is lower than 2. However, such an estimation is just an indication of the duration for the required initial computation, thus such an estimation is generally taken several times its value to get a safer assumption. For the present computation, it is assumed that the computation of 10 impeller revolutions (5 times the estimation) should be sufficient to obtain a fully developed flow field in the impeller and the diffuser.

The pressure coefficient at the sampling point SP1, see Fig. 5.2 on page 55, was monitored since the start of the computation for evaluating the computation convergence. The time history of this signal is shown in Fig. 4.13(a). The pressure coefficient is computed as follow: $C_{\mathrm{p}} = \frac{p - p_{\mathrm{ref}}}{\frac{1}{2}\rho U_{1\mathrm{e}}^2}$, where p_{ref} is located in the cone (upstream the impeller) at [-0.1190,0.0687,-0.2302]. As it can be seen, the start of the computation induces a

Table 4.5: Volume of each component of the pump-turbine scale model with an estimation of the number of impeller revolutions for all initial fluid particles to leave each component. Q and T respectively represent the pump-turbine flow rate and the impeller period and are equal, respectively, to $2.304 \cdot 10^{-2}$ m^3/s and 0.4 s.

Component	Volume [m^3]	Volume/Q/T [Nb of revolutions]
Cone	$3.04 \cdot 10^{-2}$ (13%)	3.3
Impeller	$1.09 \cdot 10^{-2}$ (5%)	1.2
Diffuser	$1.49 \cdot 10^{-2}$ (7%)	1.6
Volute	$1.72 \cdot 10^{-1}$ (75%)	18.7
Total	$2.28 \cdot 10^{-1}$	25

high-amplitude pressure wave, which is dampened within 3 impeller revolutions. After 5 impeller revolutions, the overset mode was switched from the static mode to the dynamic mode and the fluctuations due to the Blade Passing Frequency (BPF) appeared in the signal. A better presentation of those fluctuations is given in Fig. 4.13(b), which shows the pressure coefficient evolution during one impeller revolution. It can be seen that the main fluctuation is occurring at twice the BPF. A glance at the evolution of the pressure during the following 5 impeller revolutions does not show significant variation. This suggests that the flow field in this area of the machine already reached a fully developed state and confirms that only a few impeller revolutions were required to initiate the flow field against the estimation given in Table 4.5. However, this short pressure time series does not necessarily show the presence of the instability within the diffuser. To clarify the occurrence of the rotating stall, Fig. 4.14 shows the instantaneous normalized velocity magnitude in the diffuser symmetry plane. As it can be seen, some diffuser channels exhibit higher velocity than their neighboring channels. Moreover, these high velocity zones can be assembled into 4 groups which are separated by approximately 90 degrees. This confirms the presence of the instability in the present computation.
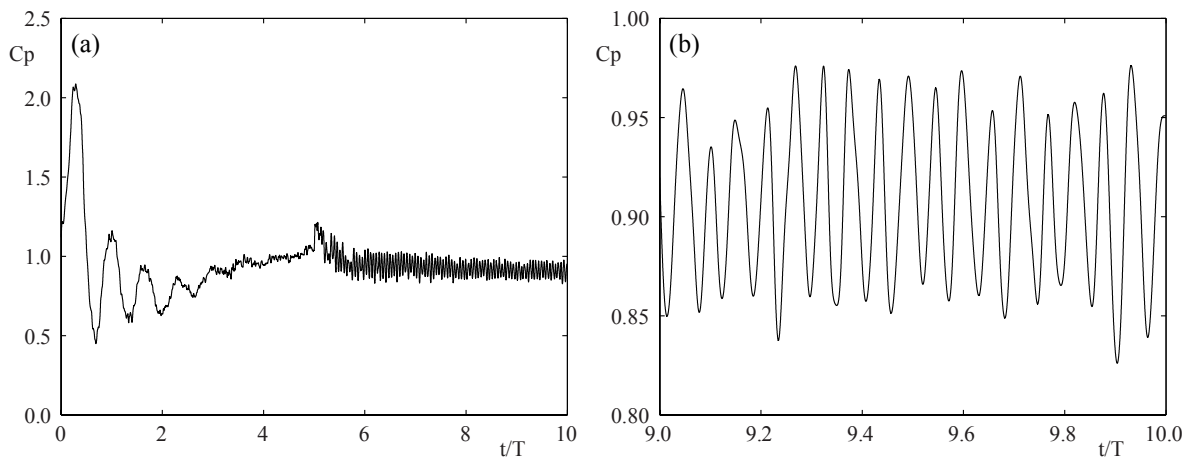
Figure 4.13: (a) Time history of the pressure coefficient at SP1 during the flow initialization. (b) Time history of the pressure coefficient during the 10th impeller revolution.
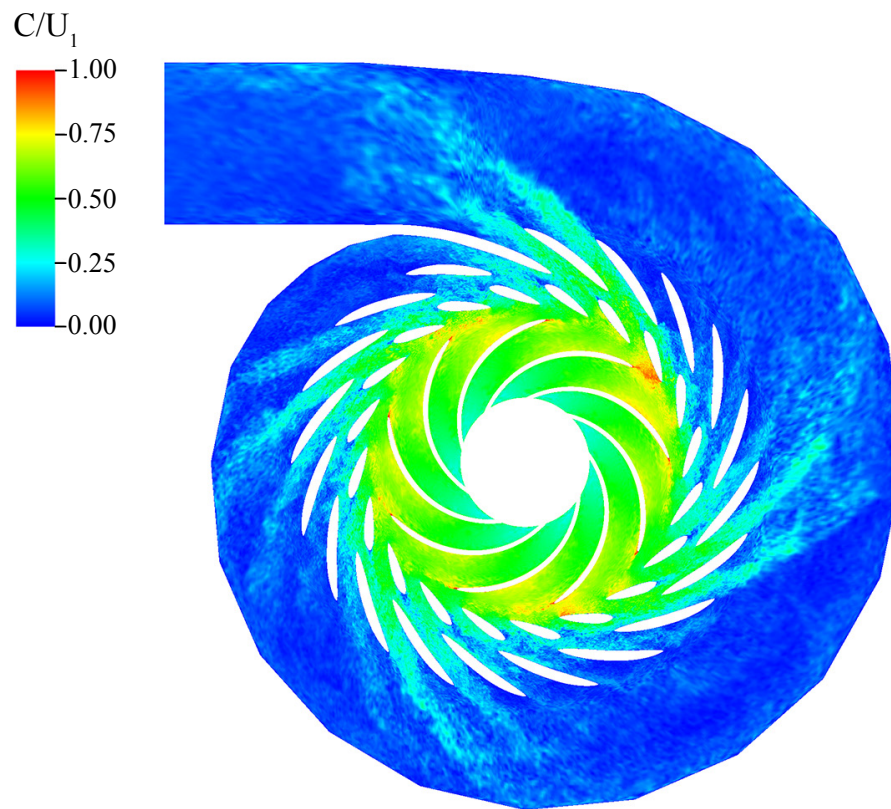
Figure 4.14: Instantaneous normalized velocity on the diffuser symmetry plane after the computation of 10 impeller revolutions.

4.3.3 Propagation Speed Discovery

The previous section showed the existence of the instability within the diffuser since the early computation stage. Therefore, as the experiment reported that such an instability

Figure 4.15: (a) Time history of the pressure coefficient fluctuation at SP1 (black curve). The red curve is the low-pass filtered pressure coefficient. (b) Discrete Fourier Transform of the instantaneous pressure coefficient.

propagates at 2% of the impeller revolution speed [3], significant pressure variation in the gap between the impeller trailing edge and the guide vane leading edge is expected. Figure 4.15(a) shows the time history of the fluctuation (black curve) and the low-pass filtered fluctuation (red curve) of the pressure coefficient at SP1, during 38 impeller revolutions. The instantaneous fluctuation exhibits a peak at t/T=33, which is the results of turning off the MIC option at that instant. The low-pass filtered pressure fluctuation was obtained by applying a zero-phase digital filter, using a low-pass 3rd order Butterworth filter with a normalized, by the impeller frequency, cutoff frequency set to f_n. Such filter will be used in the remaining of the document for any instantaneous signal unless otherwise explicitly stated. The pressure signal clearly exhibits a cyclic pattern recognized by the two pressure drops at t/T approximately equal to 16 and 38. The time lag between these two drops indicates that the individual channel is encountered with the passage of a stall cell at every 22 impeller revolutions which is about twice longer period than what was reported by the experiment, i.e. approximately 12 impeller revolutions. Such a low propagation speed is confirmed by the Discrete Fourier Transform (DFT) shown in Fig. 4.15(b) with a normalized frequency resolution of 0.019. Three main peaks are visible at the normalized frequencies 0.038, 9 and 18. The latter two normalized frequencies correspond to the BPF and its first harmonics, respectively. The first one corresponds to the rotating stall. Since there are 4 stall cells, the normalized frequency of the first peak has to be divided accordingly, which results in a normalized propagation speed of 0.95% (26 impeller revolutions for one stall cell passage), i.e. approximately twice smaller than the experiment. The counter measure that the present research has taken against this discrepancy will be explained in the next chapter.

Part III

Results

Chapter 5

Reduced Reynolds Number Computation

5.1 Numerical Setup

The initial computation of the rotating stall performed for a Reynolds number 5 time smaller than the experiment showed that the four rotating stall cells can be captured, but the computed propagation speed was approximately twice smaller compared to that of the experiment. It is assumed that the cause of this difference is due to an under resolution of the physics, as the mesh used is too coarse for that Reynolds number. Therefore, to verify this hypothesis, the Reynolds number is again reduced by a factor 5, resulting in a total reduction by a factor of 25 compared to the experiment. The numerical setup is strictly identical to the previous computation (use of the same mesh of 85 million elements) except for the kinematic viscosity, which is multiplied by a factor 5. Furthermore, the initial flow field was set to the latest flow field obtained with the initial computation and 5 impeller revolutions computation were carried out for the flow to converge to the new state for the further reduced Reynolds number.

5.2 Comparison with Experimental Data

5.2.1 Propagation Speed Discovery

Local Pressure Fluctuation

The presence of the rotating stall is clearly visible by the pressure variation in the area between the trailing edge of the impeller blades and the leading edge of the guide vanes, as shown in the former computation. Therefore, the pressure at SP1 location is monitored during the computation of 35 impeller revolutions. Such a time history fluctuation is depicted in Fig. 5.1(a), where three pressure drops can be identified. Compared to the initial computation, which showed that the passage of one stall cell required approximately 26 impeller revolutions, see Fig. 4.15(a), the passage of one stall cell requires approximately 12 impeller revolutions. This propagation speed is confirmed by the frequency spectrum of the pressure coefficient fluctuation as shown in Fig. 5.1(b), where three main peaks at a normalized frequency of 0.076, 9 and 18 can be seen. The two latter
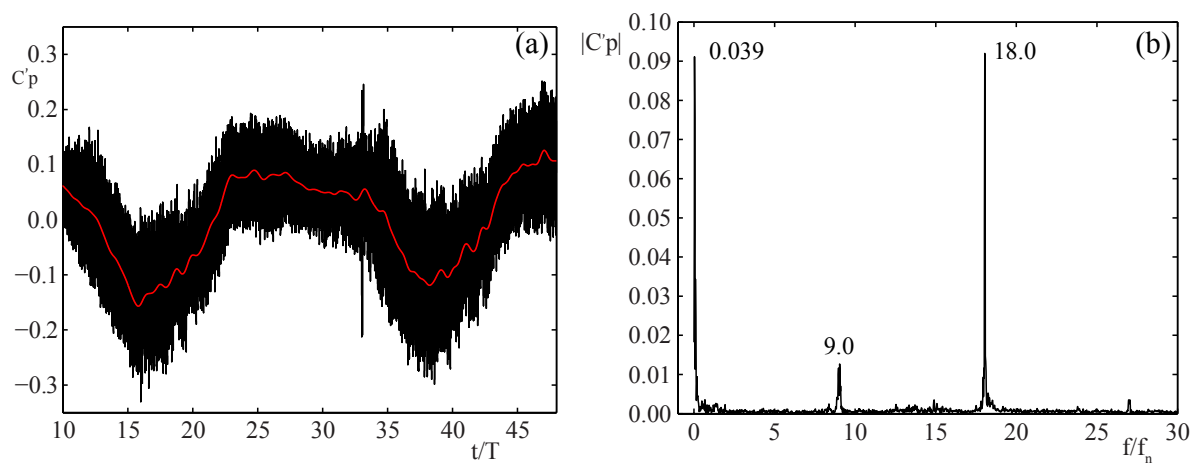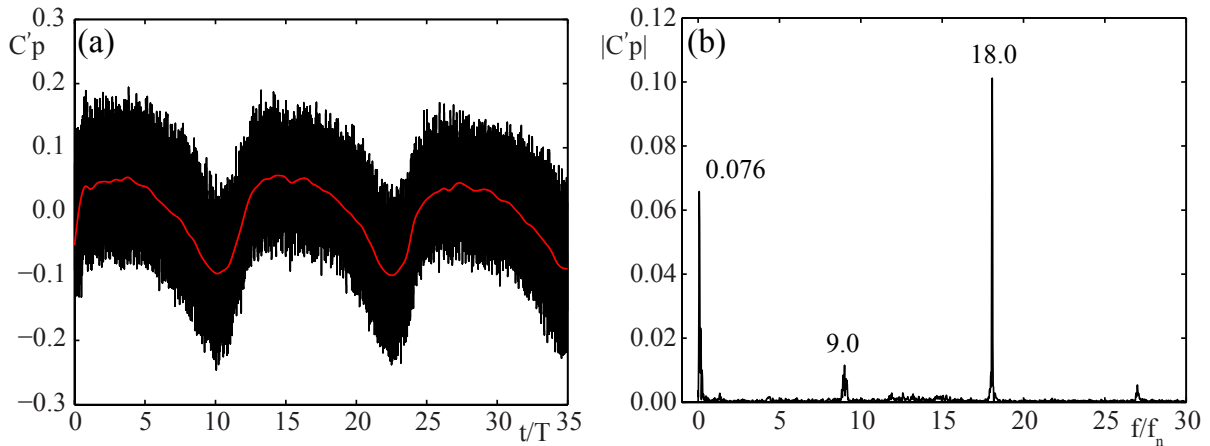
Figure 5.1: (a) Time history of the pressure coefficient fluctuation at SP1.The red curve is the pressure coefficient fluctuation that is low-pass filtered using a cutoff frequency equal to f_n. (b) Discrete Fourier Transform of the instantaneous pressure coefficient fluctuation.

frequencies correspond respectively to the BPF and its first harmonic, whereas the first frequency corresponds to the stall rotation. The resolution of the spectrum is similar to the former computation and is 0.019. From the investigation of the local pressure it can be concluded that the propagation speed is 9% slower compared to the experiment, i.e. $\omega_s/\omega = 1.9\%$. However, the present spectrum resolution is not sufficient to accurately assess the propagation speed, as the two neighboring frequencies would give a propagation 31% lower and 13% faster than the experiment.

Flow Rate Fluctuation at the Guide Vane Throat

Another approach to quantify the propagation speed of the stall cells is to monitor the flow rate variation through each guide vane channel because the presence of a stall cell in a channel reduces the amount of flow passing through it. Using the FFB capability to save the value of any quantity at each time step, a discrete surface representing the guide vane throat was generated to record the velocity field for each time step. A 2D view of the guide vane throat is shown in Fig. 5.2 by the green circles and they are composed of 27 sampling points hyperbolically distributed in order to have a finer discretization near the guide vane walls. In the spanwise direction 29 sampling points were also distributed hyperbolically, which resulted in a total of 783 sampling points per guide vane throat.

The previous visualization of the flow, see Fig. 4.14, showed that the stall cells exhibit a double spatial symmetry, which suggests a propagation speed approximately similar for each stall cells. Figure 5.3 shows the time histories of flow rate through 4 guide vane throats separated by 5 guide vane channels with each other, i.e. throats 4, 9 14 and 19. It can be confirmed that these four channels exhibit a similar variation. Furthermore, using the four flow rates, a spatial average was computed and is depicted by the black line. Such an average has been used to estimate the number of impeller revolutions required to reach back to the initial condition for the individual channel. It takes 12.3 impeller revolutions for a channel to see the full passage of one stall cell. Using this evaluation, 49.3 impeller revolutions are required for one full stall cycle, which results in a normalized propagation speed of $\omega_s/\omega = 2.03\%$. This results is very satisfactory as it confirmed the
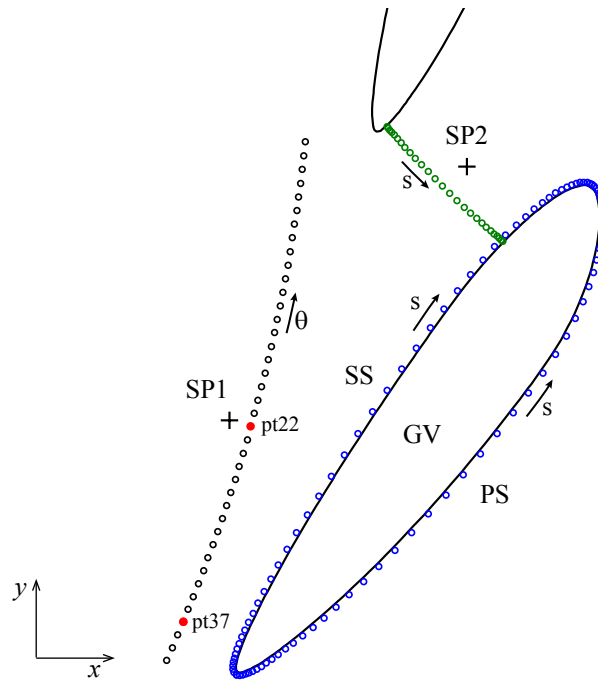
Figure 5.2: 2D location of the velocity sampling points represented by circles. The black equidistant circles compose the circular surface with a radius of 277 mm. The hyperbolically distributed green circles compose the throat surface. The hyperbolically distributed blue circles compose the surface 0.5 mm apart from the guide vane. The two black circle filled in red are the nearest sampling points to SP1 and the guide vane suction side. The crosses SP1 and SP2 are two pressure sampling points.

previous estimation of the propagation speed using the pressure signal and also because it means that the computed stall cells propagate approximately the same speed as in the experiment. In fact, the computed propagation speed is only 3.4% slower than that of the measurement.

5.2.2 Flow Patterns at Specific Locations

During the experimental campaign, Laser Doppler Velocimetry (LDV) measurements were carried out to investigate the local flow patterns at three different locations. These locations are the guide vane throat surface where the velocity normal to the surface was measured; a surface 0.5 mm apart from a guide vane where the velocity tangential to the surface was measured and a cylindrical surface with a radius of 277 mm (15.2 mm apart from the impeller trailing edge) where both the radial and the tangential velocities were measured. Furthermore, the data were averaged regarding the phase of the stall. Such a phase is obtained using the time history of a pressure signal located at the same location at SP1 for 100 impeller revolutions to make an analytic signal as follow:

$$\mathcal{P}(t) = \tilde{p}'(t) + i\mathcal{H}(\tilde{p}'(t)) \tag{5.1}$$

where $\tilde{p}'$ is the fluctuation of the low-pass filtered pressure and $\mathcal{H}(\tilde{p}')$ its Hilbert transform. The analytic amplitude and analytic phase are respectively $a(t) = |\mathcal{P}(t)|$ and $\phi(t) =$
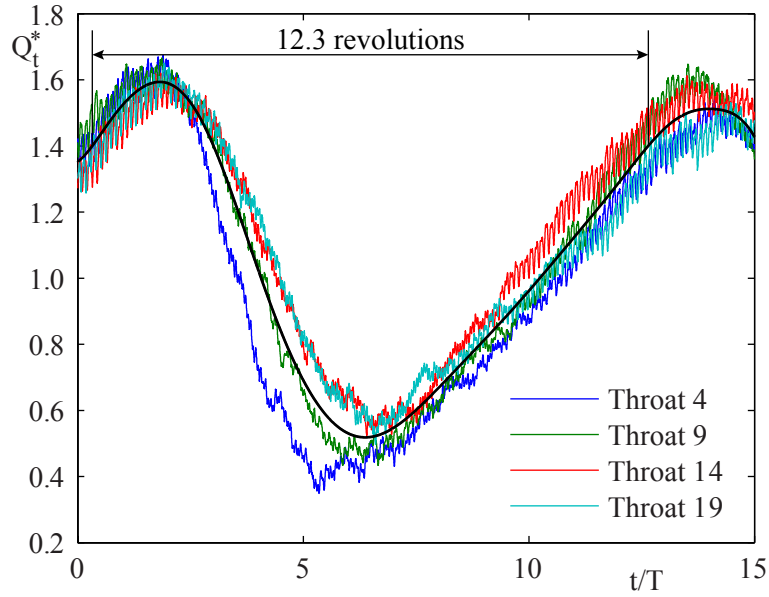
Figure 5.3: Time histories of the flow rate through 4 guide vane throats separated by 5 channels.

$arg(\mathcal{P}(t))$. This decomposition is reversible and the original signal can be reconstructed as follow:

$$\tilde{p}'(t) = a(t)cos(\phi(t)) \tag{5.2}$$

Figures 5.4 a) and b) show respectively the analytic phase and the analytic amplitude of the pressure signal computed at SP1 shown in Fig. 5.1 (a). The three cycles that can be seen in Fig. 5.1 (b) correspond to three passages of a stall cell. Therefore, the analytic phase ϕ will be hereafter referred to as stall phase.

For comparison purposes, the flow through the guide vane throat and the cylindrical section have been recorded along all the diffuser circumference. However, with the number of the sampling points being large, the flow near the guide vanes could be recorded only for five guide vanes. The resulting number of the sampling points is 160,000 to save the three instantaneous velocity components. To the contrary, as the rotating stall phenomena propagates at a low speed, the present computation computes only three passages of a stall cell through a guide vane channel which makes the number of samples for stall phase average low. Therefore, to increase the number of samples, a space average is performed, which takes into account all the samples in the diffuser experiencing a similar stall phase. Doing so gives around 50 samples for the throat and the cylindrical surfaces and 12 samples for the guide vane surfaces.

As introduced previously, the numerical data were obtained by storing the velocity vector on a discrete surface at each time step, see Fig. 5.2, using hyperbolic distribution to better discretize the flow near walls. For all the surfaces, the spanwise side is discretized by 29 sampling points. The resulting discrete surfaces are given in Table 5.1 and the flow patterns in these surface will be described below.
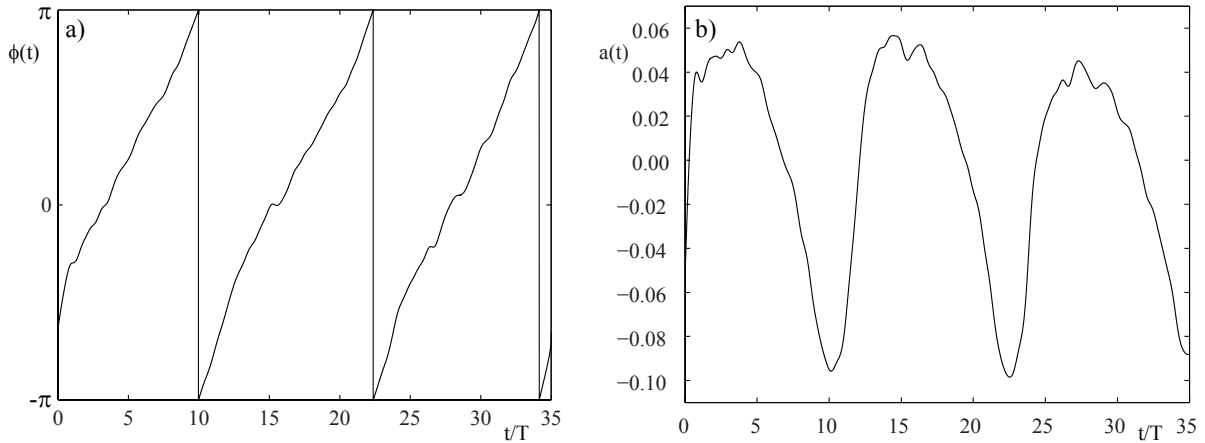
Figure 5.4: Analytic signal of the low-pass filtered pressure fluctuation signal shown on Fig. 5.1 (a): a) analytic/stall phase, b) analytic amplitude.

Flow Patterns at the Throat Surface

The stall-phase-averaged velocity normal to the throat surface obtained by the measurement and the computation, are depicted respectively in Fig. 5.5 and Fig. 5.6. The stall-phase-averaged flow is shown for 6 different phases, i.e. $\phi=[0,\ \pi/2,\ 3\pi/4,\ \pi,\ 5\pi/4,\ 3\pi/2]$, with $\phi=0$ representing the phase when the guide vane channel experiences the maximum flow rate, i.e. the minimum pressure. The comparison between the experiment and the computation shows that some discrepancies exist between them.

The experiment reported a reverse flow between the stall phases $\phi=3\pi/4$ to $\phi=5\pi/4$. The reverse flow spans all the vane-to-vane channel pitch near the hub and occupies approximately 20% of the throat surface area. The computation also shows a reverse flow, but occupies a smaller area than the experiment. The reverse flow is mainly located at the guide vane suction side near the hub. A reverse flow is also visible at the guide vane pressure side near the hub, but no decisive reverse flow is observed at the mid-pitch in the computation.

Regarding the magnitude of the flow velocity, it can be seen that the computation indicates that the velocity extrema are higher than the experiment. Indeed, the computed velocity is lower than the measured velocity when the channel is stalled, see Fig. 5.5 (c) and Fig. 5.6 (c). In the same manner it can be seen that the computed velocity is higher than the measured velocity, when the channel experiences a high flow rate, see Fig. 5.5 (a) and Fig. 5.6 (a).

These differences may be partially attributed to the stall phase averaging, which picks

Table 5.1: Surface discretization for comparison with LDV measurements. The physical location of these surfaces is shown in Fig. 5.2.

Surface	Discretization	Total
Throat	27x29	783
Guide vane	2x50x29	2,900
R277	40x29	1,160

Figure 5.5: Stall-phase-averaged normal (streamwise direction) velocity in the guide vane throat section measured by LDV at $\varphi = 0.026$. a-f) Velocity contour plots along different phase angles from 0 to $3\pi/2$. The bold line represents the level of zero velocity. Figures obtained from [3].

a single phase to average the data. Namely, the flow field fluctuates rapidly and thus changes in a short time. Therefore, a small difference in the time of picks up may result in a noticeable difference in the average flow pattern. Furthermore, in both cases a discrete grid was used and the corresponding data were interpolated. The grid for the computation is approximately twice finer than the experiment and refinement is performed near walls for the computation, which may introduce some differences. However, these possible source of errors cannot by themselves explain the differences between the computed and the measured flow velocities. These differences are most likely attributed to the difference of the Reynolds numbers in the computation and in the experiment.

Flow Patterns at the Guide Vane Surface

In a similar manner, the measured and computed stall-phase-averaged tangential flows,
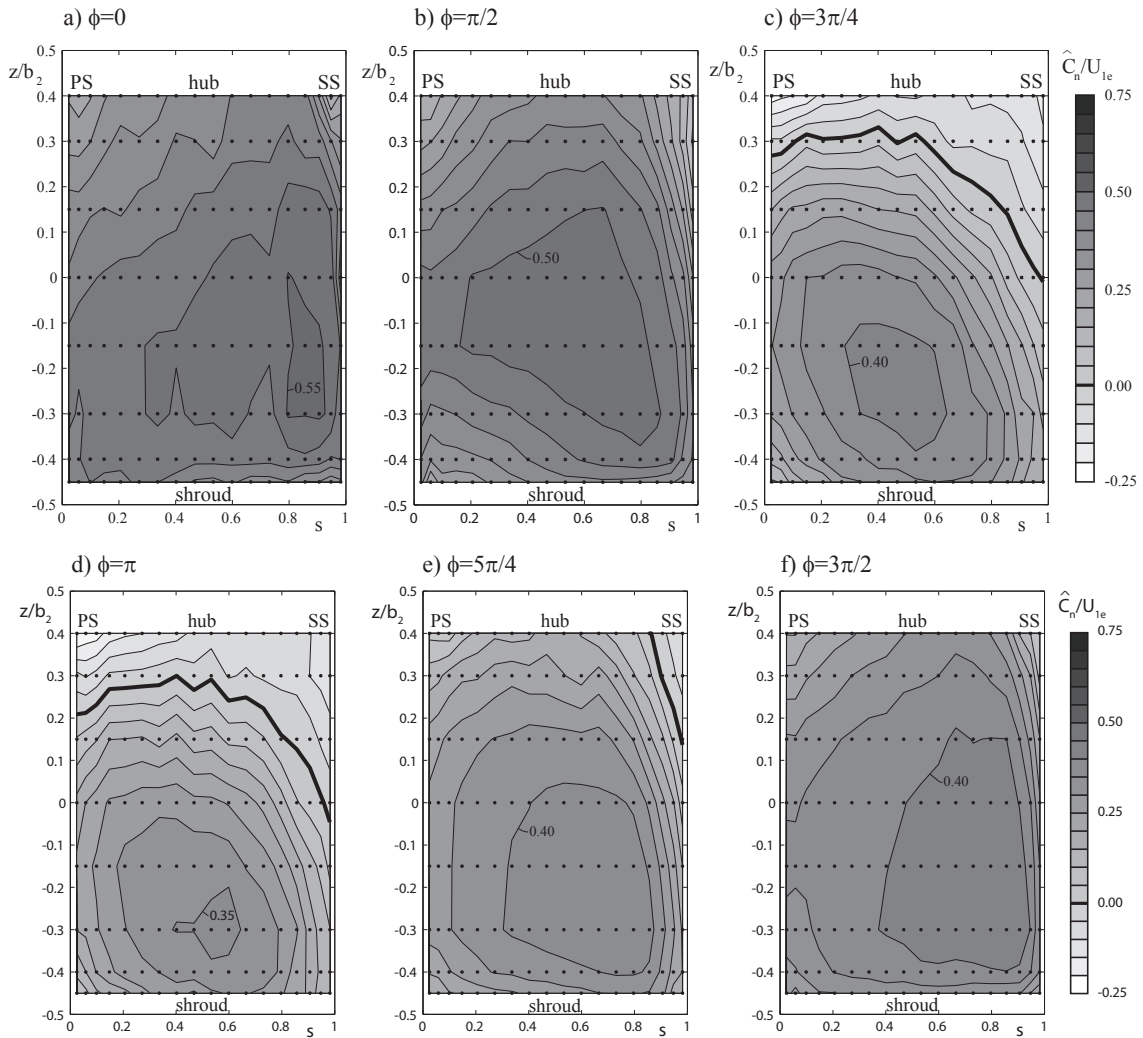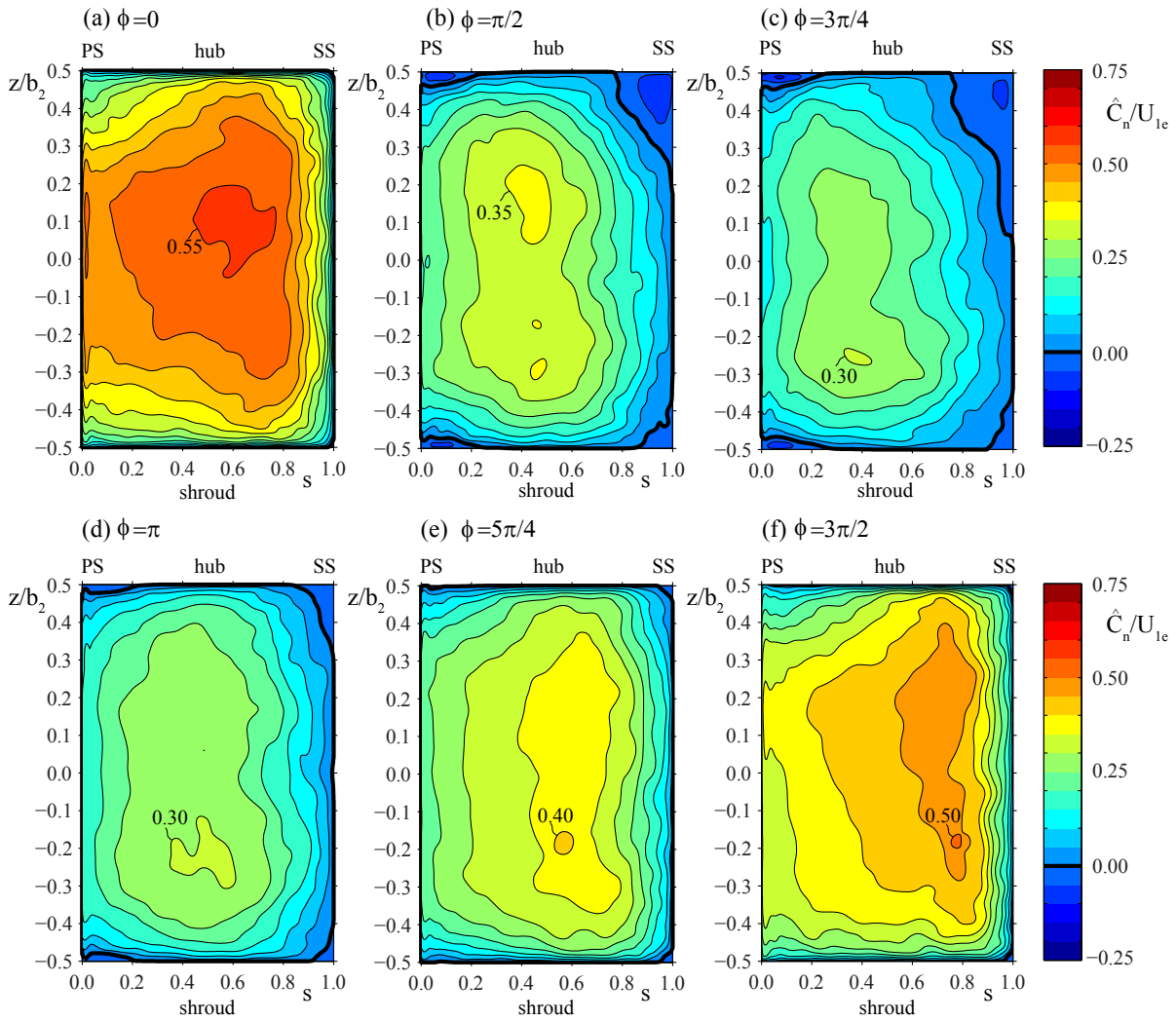
Figure 5.6: Stall-phase-averaged normal (streamwise direction) velocity in the guide vane throat section computed by LES at $\varphi = 0.026$. a-f) Velocity contour plots along different phase angles from 0 to $3\pi/2$. The bold line represents the level of zero velocity.

in the streamwise direction, on a surface apart from 0.5 mm of a guide vane are shown in Fig. 5.7 and Fig. 5.8, respectively. The surface around the guide vane is decomposed into the suction side (SS) part and the pressure side (PS) part. These figures show the stall-phase-averaged flow patterns for the 6 different phases as in Fig. 5.5 and 5.6. Regarding the computed flow pattern, it is noticeable that recirculations are always present at the guide vane trailing edge (s=1) all along the span. The reason is that the blunt trailing edge always induces flow separation. This recirculation is not visible from the experiment, as this area was not accessible. In this representation of the flow field, the computation delivers again a more symmetric (with respect to the spanwise direction) flow patterns compared to the experiment. The experiment shows a recirculation located near the hub at the suction side. Furthermore, the velocity gradients are less pronounced in the experiment compared to the computation. In the experiment, the flow decelerates gradually from the leading edge toward the trailing edge near the shroud, whereas the computation exhibits higher gradients located near the leading edge. However, it should

be recalled that only a few samples (approximately 12) were available for this phase average in the computation. Hence, these patterns in the computation may not represent the phase-averaged flow and may just show that of an instantaneous flow.

In addition to that, at most of the phases (Fig. 5.8 (a) to (f)), low tangential velocities are observed near the guide vane leading edge both near the shroud and the hub in the computation. These low velocity zones are associated with the presence of two horseshoe vortices, which are the result of the interaction of the impinging boundary layer at the top and the bottom ring on the guide vane. The effect of these horseshoe vortices is mainly seen in the computation on the suction side at $\phi=\pi/2$, thus before the channel is fully stalled.

Flow Pattern at the Cylindrical Section

The pattern of the flow field entering the guide vane is very important as it is a key parameter to determine the favorable conditions for the stall to appear. Thus, the radial and tangential components of a cylindrical surface with a radius $R=277$ mm are monitored. The resulting stall-phase averaged flows are shown in Fig. 5.9 for the experimental data and in Fig. 5.10 for the computational data. In both cases, figures (a) to (c) show the normalized radial velocity and figures (e) to (f) show the normalized tangential velocity for $\phi=[0, \pi/2, 3\pi/4]$.

The comparison between the experiment and the computation shows that there are good qualitative and quantitative agreements for the radial velocity. The computed magnitude of the velocity as well as the location of the reverse flow agree well with the measurements. However, the sizes of the computed reverse flow are smaller compared to the experiment. For the tangential velocity, one can see that the computed velocity is about 10% higher compared to the measurements. One possibility is that the relative velocity W exiting the pump is slightly slower in the computation than in the experiment, which would be the typical result of an under resolution in the boundary layer thickness. If the impeller boundary layers are under-resolved, the thickness of the boundary layers are also under-predicted, which increases the effective channel pitch and reduces the flow velocity. Therefore, the absolute angle α is reduced, increasing the tangential velocity.

5.3   Discussion

This chapter compared the computed flow with the experiment. It confirmed that the Reynolds number plays a significant role in the computation of the rotating stall phenomenon. Reducing the Reynolds number compared to the initial computation resulted in the capture of the phenomenon reported by the experimental investigation. The consequence of the reduction of the Reynolds number was an increase of the size of the turbulence scales. Therefore, the ability of the present grid to compute the turbulence scales was enhanced.

However, it was shown that the patterns of the flow through the throat, around a guide vane and through a circular surface near the guide vane inlet are different in the velocity magnitude and in the velocity distribution. These differences may partially be attributed to the difference of the surfaces discretization and by the difference of the number of samples for the stall averaging. However, these cannot explain the observed

difference between the computation and the experiment by themselves. The observed difference is most likely due to the difference in the Reynolds numbers in the experiment and the computation. Effects of the Reynolds number will further be discussed in the next chapter.

Despite discrepancies of the flow patterns, the computed specific energy coefficient ψ are consistent with the experiment. Indeed, the relative difference between the computed ψ and the experiment is only of 0.36%. Meanwhile, the propagation speed computed was only 3.4% slower than the experiment. Table 5.2 shows the comparison between the experimental and computed flow coefficient φ, energy coefficient Ψ and the propagation speed ω_s. The results of the RANS computation were obtained from [3]. Such a comparison enhances the accuracy of the Re/25 computation. Therefore, it is believed that, despite the flow pattern discrepancies, the present computation has produced essential features of the flow field and can thus be used to study the rotating stall phenomenon in detail.

Table 5.2: Comparison of the experimental and numerical values for the flow coefficient φ, the energy coefficient Ψ and the propagation speed ω_s.

	Exp.	RANS	LES(Re/5)	LES(Re/25)
φ	0.026	0.032	0.026	0.026
Rel. difference	-	23%	0%	0%
Ψ	1.079	0.962	1.115	1.082
Rel. difference	-	-10.8%	3.35%	0.36%
ω_s/ω	0.021	0.029	0.0008	0.0203
Rel. difference	-	38%	-60%	-3.4%
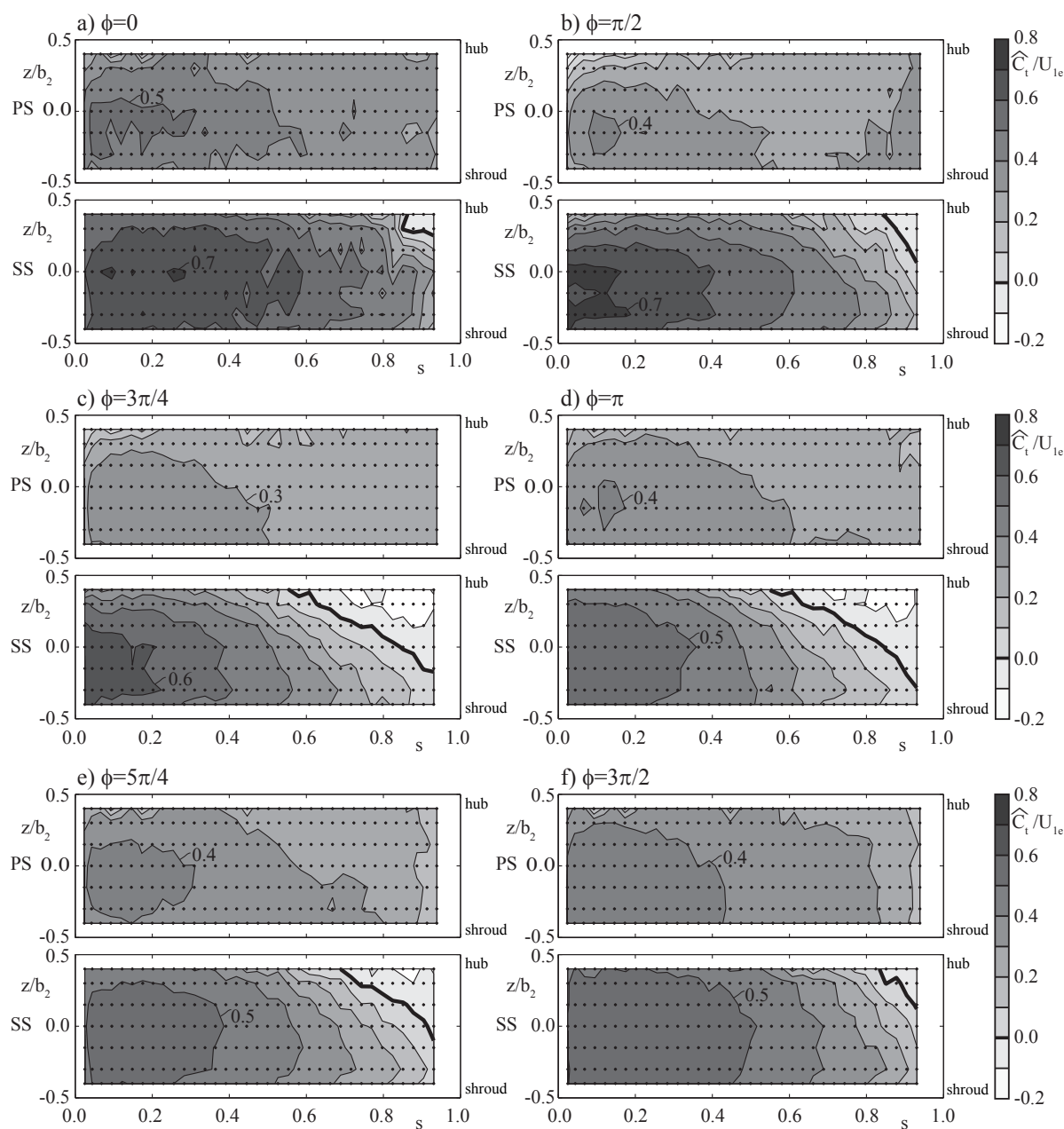
Figure 5.7: Stall-phase-averaged tangential velocity at 0.5 mm apart from guide vane 4, measured by LDV at $\varphi = 0.026$. The bold line represents the level of zero velocity. Figures obtained from [3].
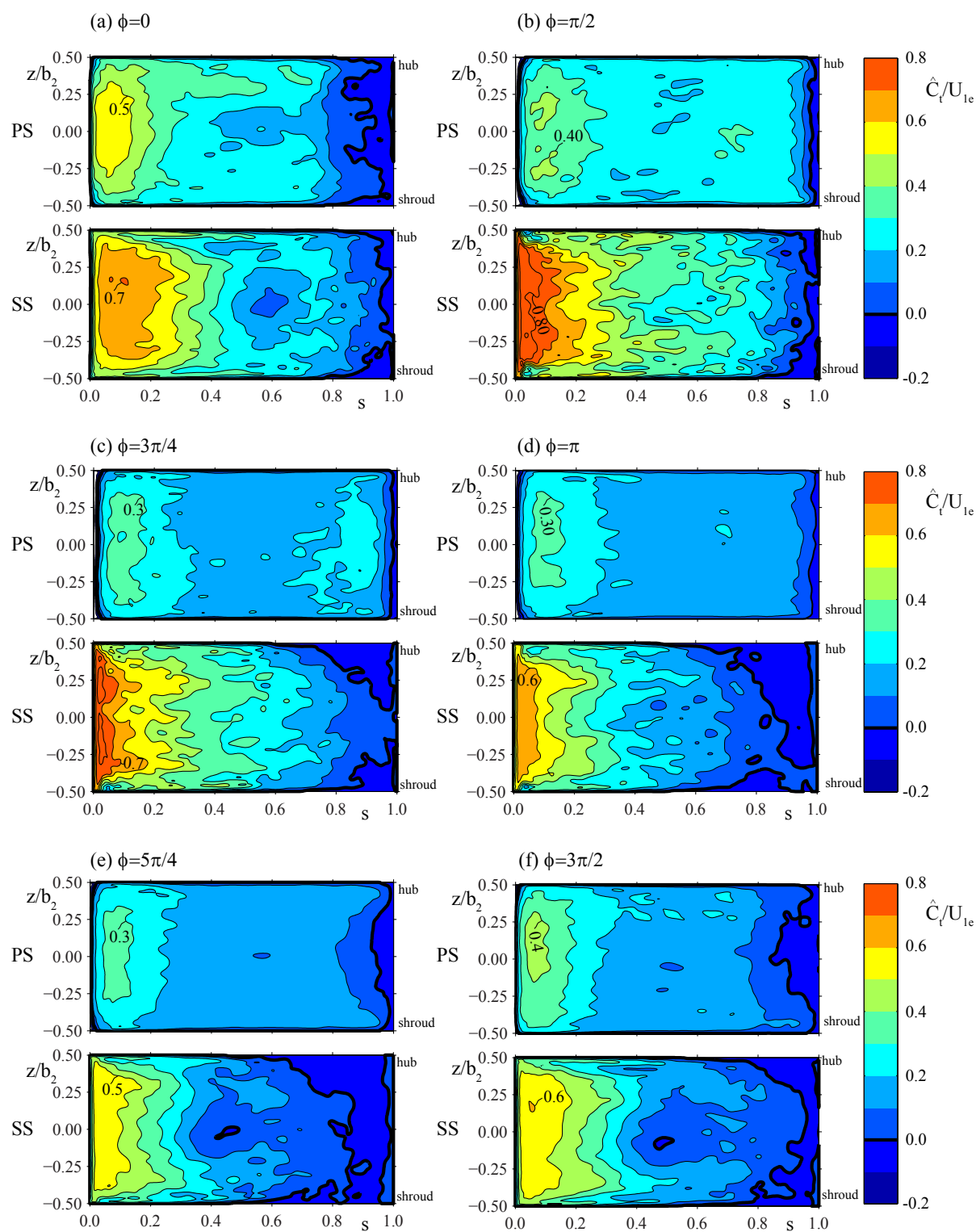
Figure 5.8: Stall-phase-averaged tangential velocity at 0.5 mm normal distance from guide vane 4, computed by LES at $\varphi = 0.026$. The bold line represents the level of zero velocity.
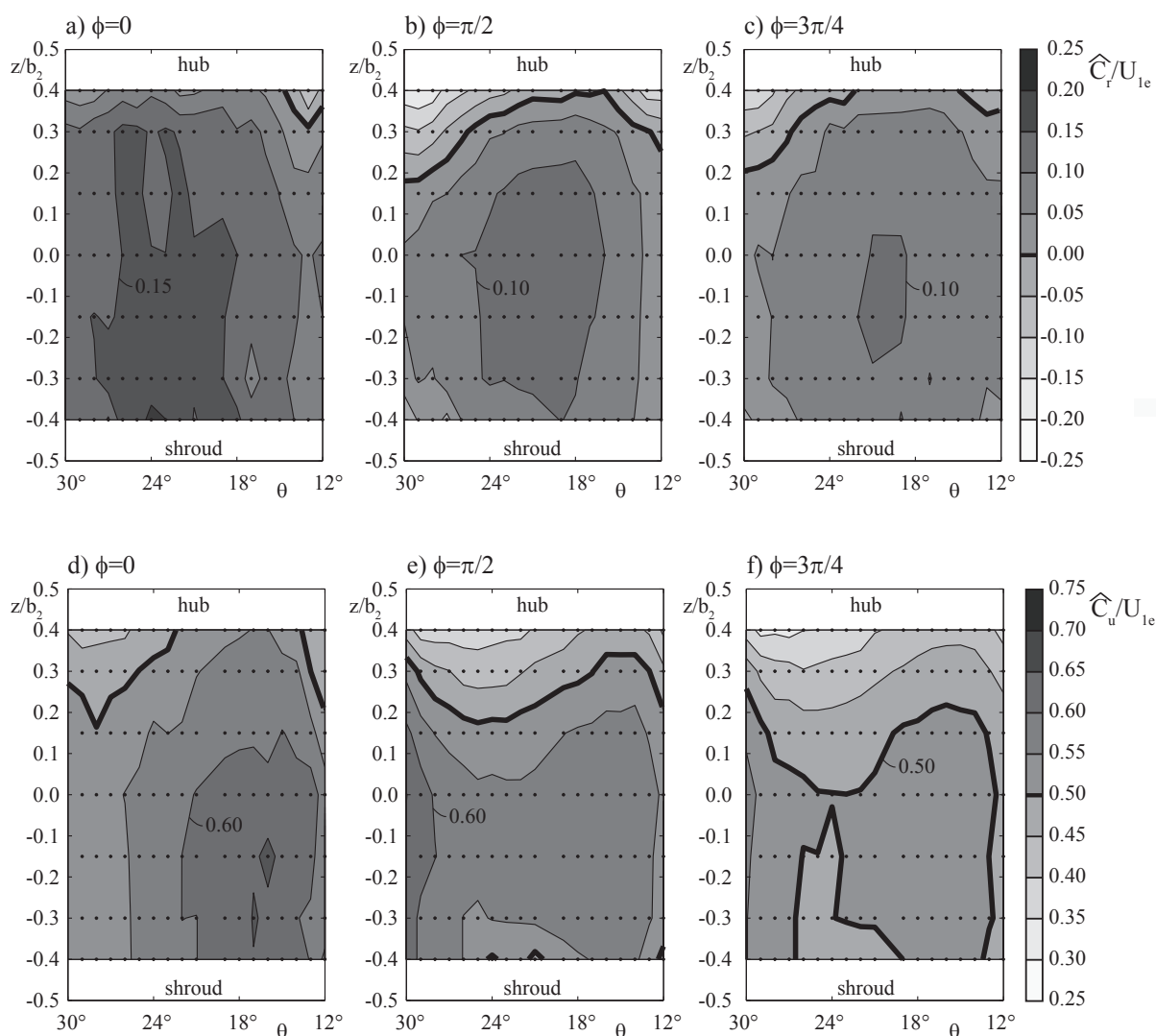
Figure 5.9: Stall-phase-averaged velocity on cylindrical section at guide vane, measured by LDV at $\varphi = 0.026$. a, b and c) radial velocity, d, e and f) circumferential velocity. The bold lines represent the level of zero velocity for the radial velocity and the level of 0.5 velocity for the circumferential velocity. Figures obtained from [3].
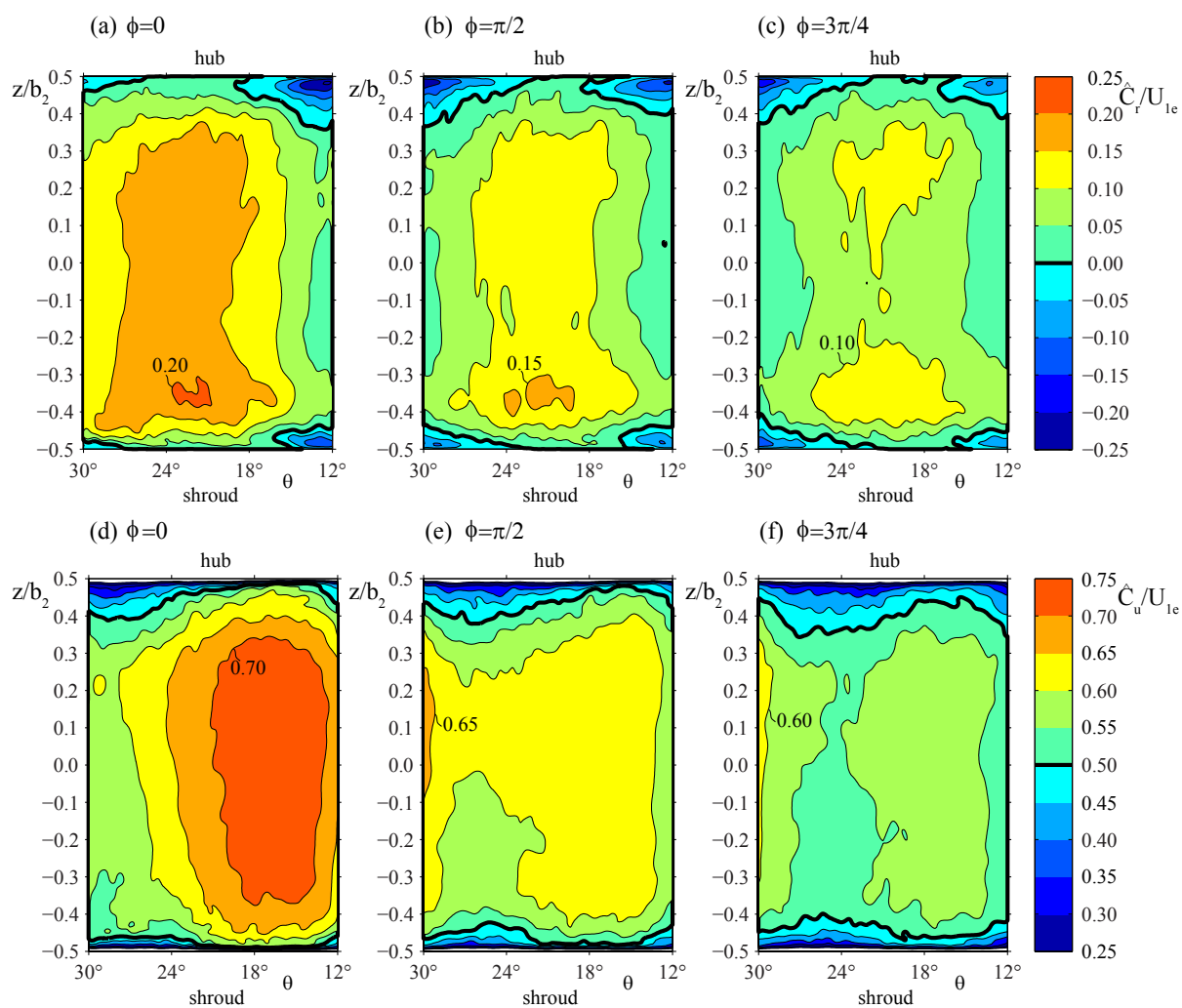
Figure 5.10: Stall-phase-averaged velocity on cylindrical section at guide vane, computed by LES at $\varphi = 0.026$. a, b and c) radial velocity, d, e and f) circumferential velocity. The bold lines represent the level of zero velocity for the radial velocity and the level of 0.5 velocity for the circumferential velocity.

Chapter 6

Rotating Stall Analysis

6.1 Stall Onset

The previous chapter revealed the existence of four stall cells in the diffuser, propagating in the sense of the impeller rotation, at a speed of ω_s/ω=2.05%. Furthermore, comparisons with the experimental data produced satisfactory results, which enable the investigation of the rotating stall phenomenon using the previously computed flow fields. Therefore, the present chapter focuses on the evolution of the flow within the diffuser, in order to obtain a better understanding of the propagation mechanisms of the stall cells in the HYDRODYNA pump-turbine.

A stall cell can be regarded as a flow recirculation region. The main reason for such a recirculation to exist is because of the part load operating conditions. A decrease in the flow rate passing through the impeller results in a reduction of the exit flow angle of the impeller as shown in Fig. 6.2. This decrease of α causes an increase of the angle of attack (AOA) on the diffuser guide vane, which leads to favorable conditions for flow separation, which results in a recirculation region at the guide vane trailing edge on the suction side. Furthermore, it is also worth mentioning that the present pump-turbine has, regardless of its operating conditions, a recirculation region at the trailing edge of the guide vanes. The guide vanes are dedicated for turbine operation and feature a standard hydrofoil shape with a thicker leading edge and a thinner trailing edge to avoid flow recirculation. However, when operating the pump-turbine in pumping mode, the guide vane profile is used in the opposite way, resulting in a thick trailing edge, which always generates a recirculation region. This region is shown by the grey area in Fig. 6.1, bound by the two horizontal tangents, shown as dash lines.

Figure 6.1: Guide vane profile. The grey area shows the region favorable for flow separation in pumping mode and the dashed lines the two horizontal tangents.
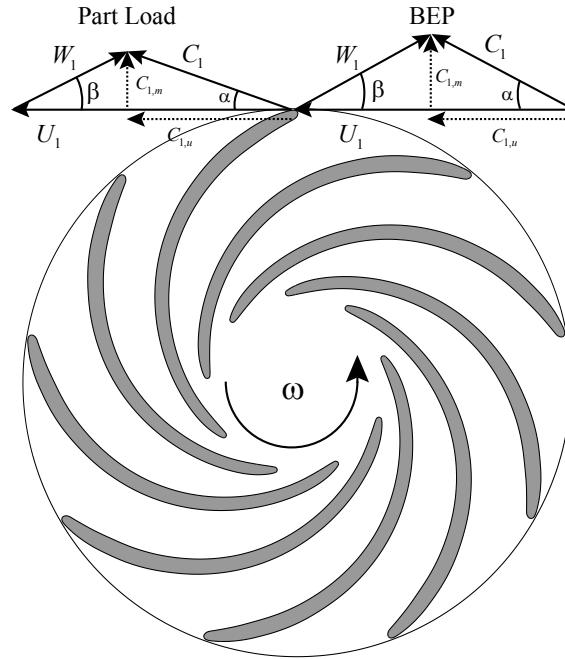
Figure 6.2: Velocity triangle at the impeller exit for the BEP and the part load conditions.

6.2   Observation of Stalled Channel Behavior

The present diffuser features 20 guide vanes and 20 stay vanes, that results in 20 vane to vane channels for the flow to reach the volute. Incompressibility imposes that at any time, the flow rate at the diffuser entry matches the one at the exit of the impeller. It results that any channel exhibiting a lower flow rate will have a counter channel experiencing a higher flow rate to keep the overall flow rate constant. In a space perspective of the rotating stall, this incompressibility constrain is the key parameter for the stall pattern into the diffuser.

The operation of the pump-turbine at 76% BEP induces the presence of four stall cells. These cells locally perturb the flow by reducing the discharge passing through a channel, as already seen in Fig. 4.14. However, continuous pressure and velocity variations between each of those cells necessitate a similar spatial organization. As the instability involves four cells at this specific operating condition, each cell has to cover 5 channels. This spatial organisation is shown in Fig. 6.3, which shows the spanwise-averaged instantaneous velocity in six channels. Channels a-b and f-g are experiencing the highest flow rate. The flow rate passing through these guide vane channels is approximately Q_t/Q_o=1.6, with Q_o being the nominal flow rate passing through the channel. As channels a-b and f-g are exhibiting a similar flow pattern, they represent the two bounds of a stall cell and the channels in between reflect the spatial organization of a stall cell. Taking the direction of the impeller rotation as reference, the upstream neighboring channel, channel b-c, exhibits a lower flow rate because of the presence of a recirculation region. This recirculation region occupies almost half the guide-vane channel pitch and the flow rate is close to Q_t/Q_o=1.0. This channel is in so called stalling process. The next upstream neighboring channel, channel c-d, is stalled corresponding to a flow rate approximately Q_t/Q_o=0.4. The recirculation region occupies almost the entire channel pitch and only

some flow can pass near the pressure side of the guide vane c. The channel with maximum and minimum flow rates are thus close as they are separated only by a single channel. Finally, to reach a cyclic pattern, the two remaining channels, channels d-e and e-f, have to represent a situation where the flow rate is increasing and the recirculation region is decreasing. Such a situation is indeed reached, as a greater flow rate is passing through channels d-e and e-f. The combination of the increase of flow rate and the decrease of the recirculation region results in an important wake spreading until the stay vane channel. Such channels have respectively a flow rate approximately Q_t/Q_o=0.8 and Q_t/Q_o=1.2.

From this first observation it can be concluded that the stall cells have a strong impact on the flow rate distribution within the diffuser. Indeed, it was shown that the presence of a stall cell induces a relative difference of the flow rate compared to the nominal flow rate up to $\pm 60\%$.

6.3 Propagation Mechanism of Stalled Cells

As the stall phenomenon is unsteady, each guide-vane channel experiences a flow rate fluctuation as shown previously in Fig. 5.3. This requires a continuous variation of the local flow field to switch from conditions favorable for the stall cell to grow to conditions favorable for the stall cell to decay and vice versa. To illustrate this evolution, Fig. 6.4 shows the flow field passing through a guide-vane channel (between GVA and GVB), at five successive different phases representing conditions encountered in the spatial organization presented in Fig. 6.4. Furthermore, each phase is temporally located in Fig. 6.4 f), where the black line shows the evolution of the flow rate passing through the channel shown in Fig. 6.4 a) by the red line. Except for the flow field shown in Fig. 6.4 c), the phase of the impeller is identical. In the case of Fig. 6.4 c) the phase of the impeller is rotated 2° in the counterclockwise direction.

To study how the flow evolves temporally within a single channel, one can set the initial phase of the rotating stall cycle when the channel does not have any significant
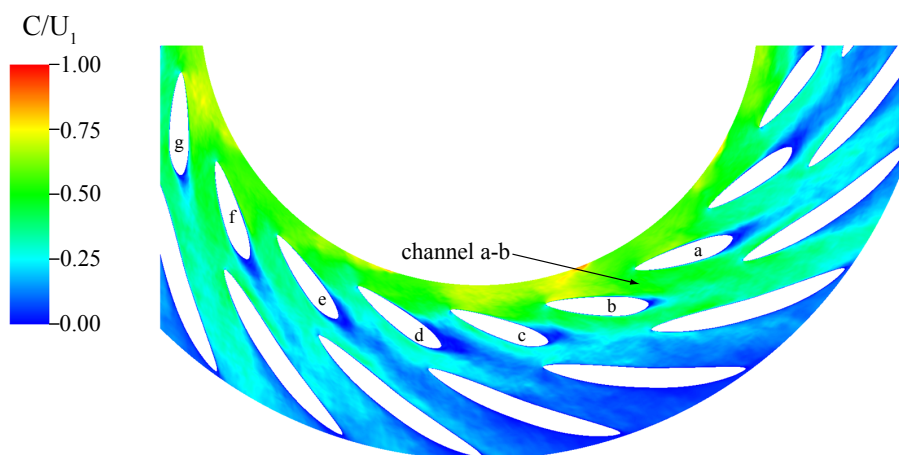
Figure 6.3: Instantaneous spanwise-averaged velocity magnitude in six diffuser channels showing the spatial organization of a stall cell. Channels a-b and f-g exhibit the highest flow rate passing through the channel. Channel b-c is stalling, channel c-d is stalled and channels d-e and e-f are recovering.
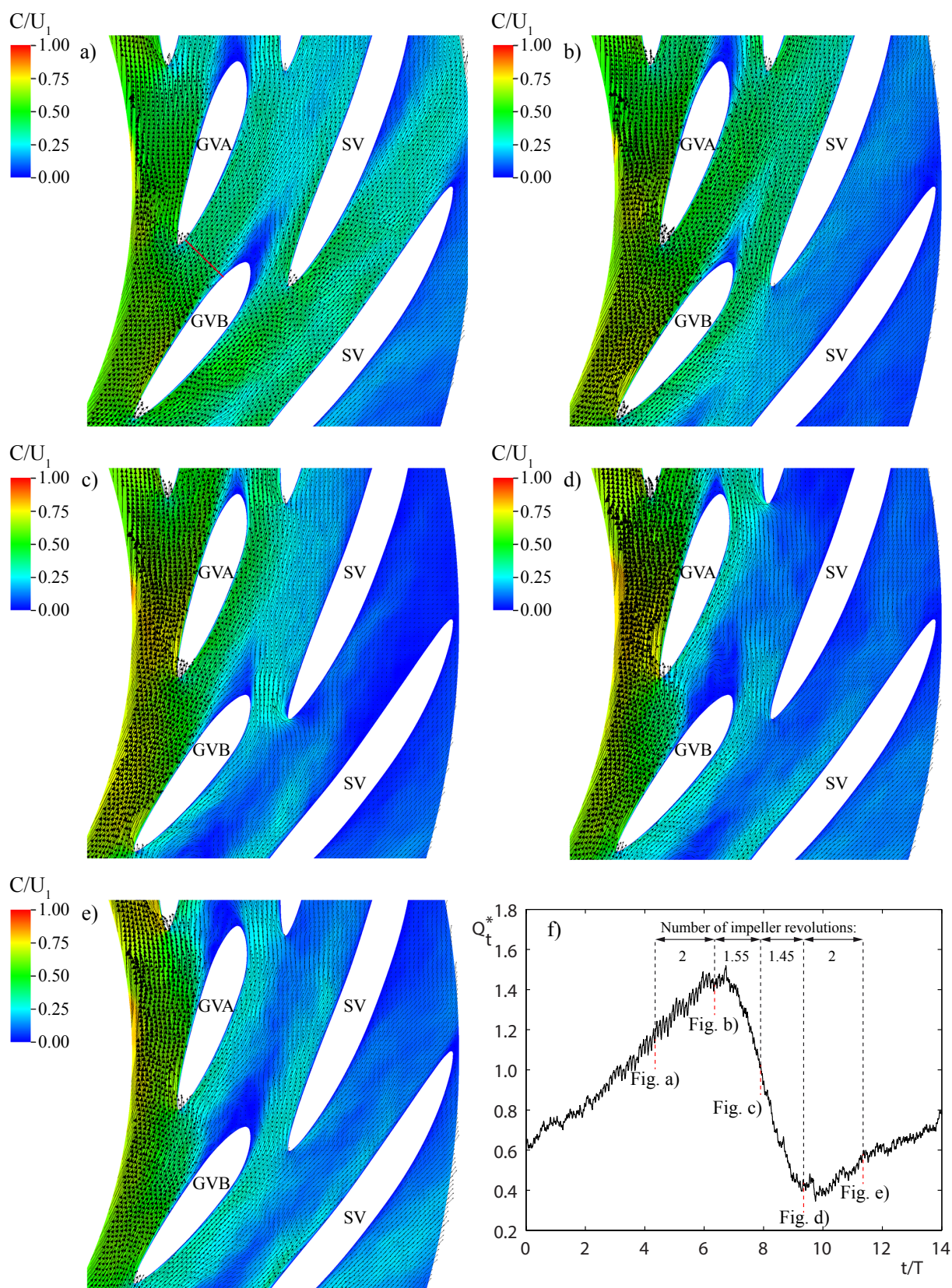
Figure 6.4: Spanwise-averaged instantaneous velocity magnitude passing through the diffuser for 5 different stall phases: a) late recovery phase, b) highest flow rate phase, c) stalling phase, d) stalled phase and e) early recovery phase. f) evolution of the flow rate passing through the section shown by the red line in figure a).
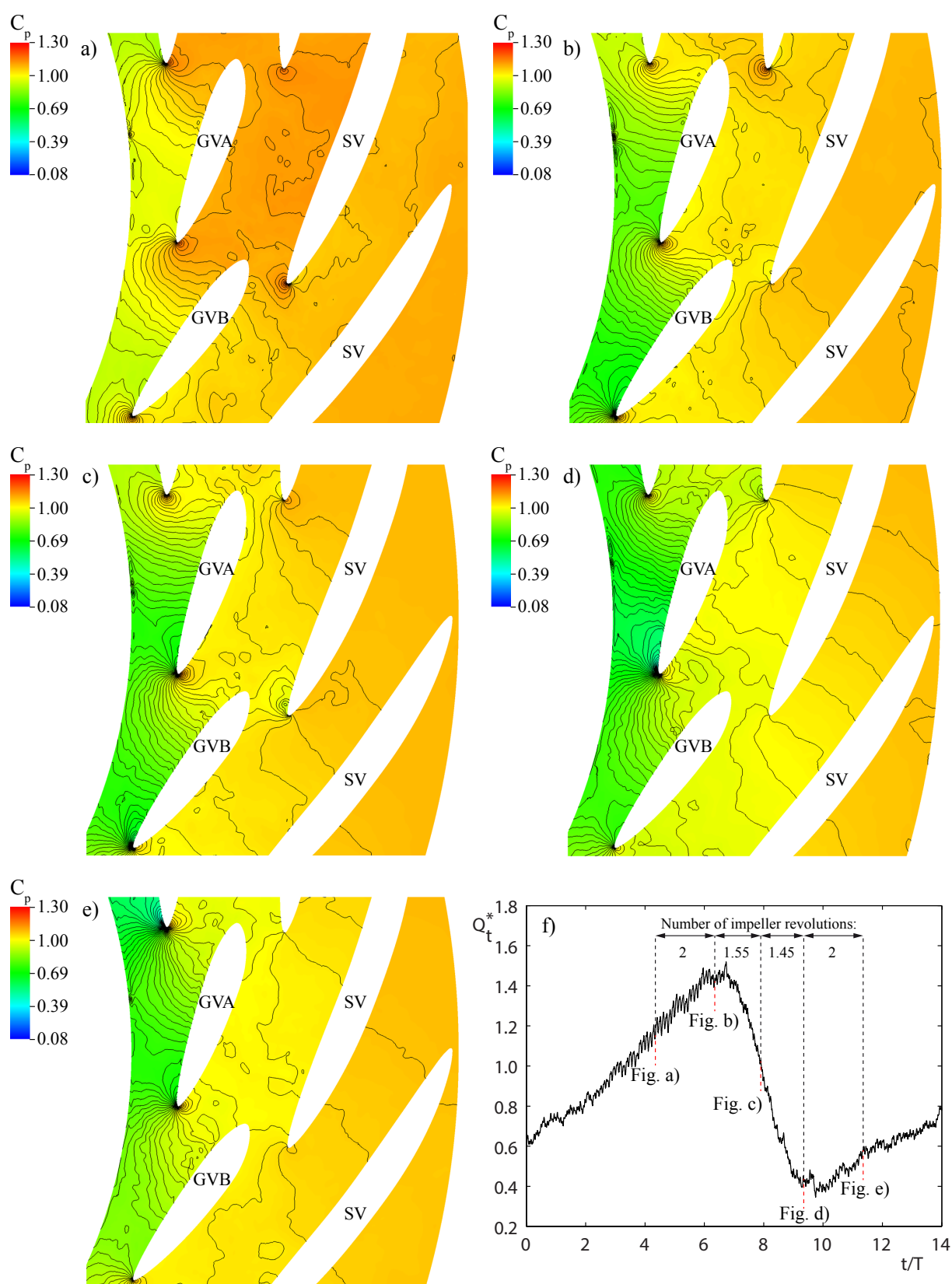
Figure 6.5: Spanwise-averaged instantaneous C_p in the diffuser for 5 different stall phases: a) late recovery phase, b) highest flow rate phase, c) stalling phase, d) stalled phase and e) early recovery phase. f) evolution of the flow rate passing through the section shown by the red line in figure a). The interval of the contour line (shown in black) is $\Delta C_p = 0.015$.

recirculation. Such a phase is shown in Fig. 6.4 a), where the guide-vane channel experiences a flow rate higher than the nominal flow rate Q_o, i.e. $Q_t^*=Q_t/Q_o=1.15$. The particularity of this phase is characterized by a flow incidence on GVA and GVB with a near zero angle of attack. Furthermore, the high velocity passing around GVB, leads to the flow separation, both on the suction and the pressure sides, because of the the guide vane geometry. The resulting wake is elongated and aligned with the guide vane chord.

Two impeller revolutions later, the channel reaches its maximum flow rate of $Q_t^*=1.42$, see Fig. 6.4 b). As previously, the flow incident on GVB is nearly parallel to the guide vane chord, but GVA exhibits a flow deviation at the leading edge, which is visible by the flow not aligned with the guide vane suction side near the leading edge, even if the flow velocity nearly reaches its maximum intensity. Regarding the recirculation zone, it can be seen that its size has reduced compared to the previous phase a). More precisely, it reaches its minimum size and tends to be less aligned with the guide vane chord. The reason is that the flow rate near the the pressure side of GVB and between GVB and the Stay Vane (SV) is increased. Because of this increase, the flow is less favorable to separate and stays attached to the GVB pressure side.

After, the channel reaches the maximum flow rate, it enters the stalling phase. Therefore, the flow rate in the passage is decreasing. Such a phase is shown in Fig. 6.4 c), which is 1.55 impeller revolutions later and has a flow rate of $Q_t^*=1.02$. Clearly, the recirculation zone has grown and occupies about the downstream 30% of the GVB suction side. The zone extends toward the center of the channel and deviates the flow passing through the channel toward the GVA pressure side, which explains why during the previous phase the flow rate near the GVB pressure side increased. With this increase of the recirculation zone toward the center of the channel, it becomes difficult for the upstream flow to pass through the channel and therefore circumvent the channel by deviating toward the downstream channel. Regarding the flow passing through the gap formed by GVB and SV, the flow rate is decreasing but still large.

Finally the flow rate trough the channel reaches its minimum and corresponds to the stalled phase, $Q_t^*=0.44$. As we can see in Fig. 6.4 d), the flow can barely go through the guide vane channel because the recirculation occupies almost all the guide vane pitch. Namely, the channel is almost blocked. This situation implies a significant rise of the pressure along the guide-vane channel and the flow that can pass trough the guide-vane channel is deviated towards the gap between GVA and SV as the pressure is lower in this area.

When the flow rate reaches its minima, the channel starts to recover, as shown in Fig. 6.4 e), $Q_t^*=0.58$. This is characterized by an increase of the flow rate near the pressure side of GVA. Furthermore, the flow incidence on GVB is decreasing. As a result, the stall cell size decreases as well. This phase is characterized by the presence of an large wake, which elongates far downstream the flow. Furthermore, as the flow velocity near the pressure side of GVB is increasing, the flow starts again to separate.

The distribution of the pressure coefficient in the diffuser is shown in Fig. 6.5. In a similar manner to the velocity fields, the distribution of the pressure coefficient is shown for 6 different phases. Figure 6.5 a) shows the pressure coefficient when the flow is near to reach its maximum flow rate through the channel. The spherical pattern of the iso-pressure at the leading edge of GVB reconfirms that the flow is almost aligned with the guide vane chord length. Therefore, no significant acceleration of the flow is seen near the

leading edge on the suction side. But, from approximately 40% to 90% of the chord length, the contour lines are concentrated on the suction side of GVB, showing the deceleration of the flow. But, once the flow passes the guide vane throat no significant decrease is visible.

Once the flow rate through the channel reaches its maximum, see Fig. 6.5 b), the pressure gradients on the suction side of GVB exhibits iso-pressure line starting from the leading edge to some points on the suction side (up to 25% of the chord length). Therefore, the flow first accelerates when it passes the leading edge and secondly decelerates where stronger adverse pressure gradients are presented. Again, once the flow passed the guide vane throat, no significant decrease is visible.

The phase shown in Fig. 6.5 c) exhibits the same pattern as previously except that the acceleration of the flow near the leading edge of GVB on the suction side is stronger. The flow is still experiencing a strong deceleration shown by the concentrated iso-pressure lines. The origin of such adverse gradients is the greater pressure drop occurring in the clearance area formed by the tailing edge of the impeller and the leading edge of the guide vane.

The next phase represents the one where the channel is stalled, see Fig. 6.5 d). In that situation, one can see that the flow acceleration on the suction side near the leading edge decreased considerably. Furthermore, the pressure gradient along the suction side also decreased considerably. Therefore, the flow can again go through the channel.

Finally, since the adverse pressure becomes weaker, the condition are more favorable for the flow to pass through the channel and will gradually increase. With this gradually increase, the velocity increases again and the pressure in the clearance will decrease, which will generate stronger adverse pressure gradients.

6.3.1 Pressure Evolution in Diffuser Channel

Under a normal condition, the pressure distribution along a diffuser channel should be constant in time. However, when stalled, because of the temporal and spatial non uniformity of the flow passing through a diffuser channel, the pressure along a channel varies according to the flow speed. The relation between the pressure and the velocity in the clearance area can be described with the Bernoulli's principle as in this area the flow is still accelerating with low vorticity and that the viscous force can be neglected. The following relation can be then applied to any arbitrary point along a streamline in the clearance area:

$$\frac{C^2}{2} + gZ + \frac{p}{\rho} = \text{cst} \tag{6.1}$$

Therefore, if the velocity of a fluid particle on an iso-altitude streamline accelerates it results that the pressure has to decrease accordingly to maintain the same level of the specific energy. To analyse how the pressure varies in a diffuser channel, the pressure at four sampling points (SP), see Fig. 6.6, is recorded. A typical evolution of the pressure coefficient, at the sampling point SP1, is shown for 14 revolutions in Fig. 6.7 a), where the black line is the instantaneous signal, the blue line is a polynomial interpolation of the signal and the letters, with their corresponding dashed lines, represent the stall phase introduced previously in Fig. 6.3. As it can be seen, the instantaneous signal exhibits high frequency and amplitude fluctuation up to 8%. The frequencies present in the signal
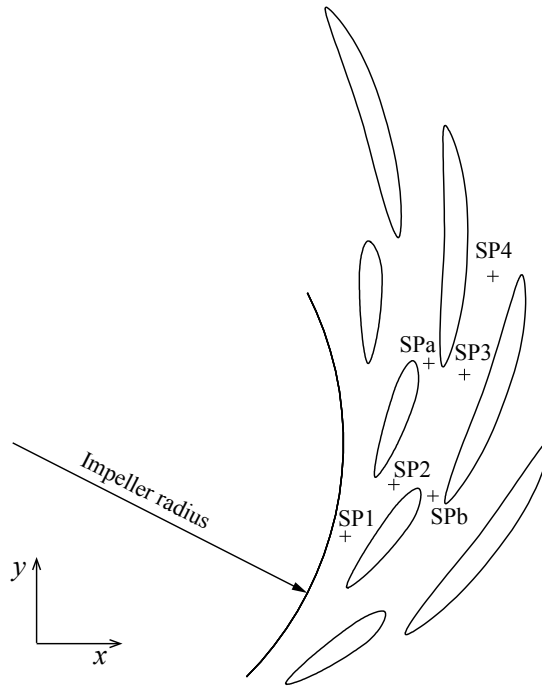
Figure 6.6: Location of the diffuser sampling points (SP).

are the blade passing frequency (BPF) and its first harmonic. For comparison purposes, only the polynomial interpolation of the four pressure signals are shown in Fig. 6.7 b). Such signals also show fluctuation at the BPF and its first harmonic, but the amplitude is decreasing along the diffuser channel flow path. The oscillation amplitudes for SP2, SP3 and SP4 are respectively 6.5%, 4% and 1%. Except the pressure near the volute (SP4) all signals show the sudden pressure decrease after 6 impeller revolutions. This confirms the presence of a stall cell, where as the flow rate increases the pressure level decreases in the whole channel to reach its minimum. However, the minimum among the signals are not reached at the same time. SP2 and SP3 reach their minimum when the channel experiences a high flow rate as shown in Fig. 6.3 f). But the minimum at SP1 is reached a little later, because of the location of the sampling point. Indeed, its location is in the gap between the impeller and the guide vane channel, where the flow field evolves differently compared to the one passing through the diffuser channel. In that gap, the variation of the tangential flow has to be taken into account and it will be shown later that the velocity passing near the sampling point reaches its maximum at the same time corresponding to that pressure minimum.

After reaching its minimum, the pressure starts to increase as the flow rate decreases. Once the stall cell is well developed, the pressure in the stay vane channel reaches the same pressure level as the volute, corresponding to the stalled phase. This phase lasts approximately during one impeller revolution and then since the flow starts again to pass through the channel, the pressure level in the channel decreases.

A closer view of the pressure coefficient evolution in the area between the guide vanes and the stay vanes is introduced in Fig. 6.8. Furthermore, the pressure coefficient evolutions (SPa and SPb) in the gap between the guide vane and the stay vane are also taken into account. As explained previously, the data is interpolated for a better visualization.

It can be seen that the evolution of the pressure located at SPb follows closely the evolution of the pressure at SP2. Therefore, it is expected that SPa is representative of the local pressure level in the downstream channel. Interestingly, we can see that the pressure at SPa is lower than all others pressures for approximately during 3.5 impeller revolutions (from t/T=8 to t/T=11), which has an impact on the flow field. As already discussed, the flow field approaching the stay vane channel is sometime deviated toward the gap formed by the guide vane and the stay vane when the channel is in the stalling phase and in the stalled phase. The reason is the difference of the flow rate passing through the two channels until that the downstream channel stalls. During that period, the difference of the flow rates induces a difference of the pressure level between the two channels. Therefore, the flows entering the stalled channel from the guide vane channel or from the upstream gap, are more favorable to exit the diffuser via the downstream gap than using the stay vane channel.

From the previous observations, the main impact of the rotating stall on the pressure level takes place in the clearance area, i.e. at SP1. It results that the difference of pressures between SP1 and SP2 is not constant and such a difference is shown in Fig. 6.9. It can be seen that the pressure difference increases when the channel experiences high flow rate and also during the first half of the stalling phase. Then, the difference decreases which corresponds to the second half of the stalling phase until the early recovery phase. Therefore, the flow is subject to a varying intensity of the adverse pressure gradient which explains one of the favorable conditions for the stall cell to grow. Since the boundary layer is decelerating, separation can take place if the momentum is not strong enough to overcome the adverse pressure gradient. In the present situation, as the flow rate through a channel increases, the pressure difference increases. However, this increase in the pressure difference does not stop the flow rate to decrease during the early stage of the stalling phase as the approaching flow has a high velocity. This approaching flow is the flow deviated from the upstream channel and this deviation is maximum at the instant c), see Fig. 6.9, because the upstream channel is fully stalled. Therefore, it can be concluded that a channel experiences its highest adverse pressure gradient once its upstream channel is fully stalled.

6.3.2 Flow Incidence of Vanes

Guide Vane

Figure 6.10 shows the evolution of the AOA on guide vanes GVA and GVB at three different distances upstream of the leading edge, i.e. 5%, 10% and 15% of the guide vane chord length. The AOA corresponds to the angle formed by the velocity vector with the orientation vector of the guide vane chord. As expected, the AOA becomes higher when approaching the leading edge, but the same trend is observed on each curve. Furthermore, both graphs show a similar pattern, but with a temporal shift assessing the disruption generated by a stall cell and this shows that the stall cell is propagating.

A strong correlation is visible between the flow incidence on GVA and the evolution of the flow rate passing through the channel shown in Fig. 6.4 f). Indeed, when the channel is in the phase of the increasing flow rate (Fig. 6.4 a) and b)), the AOA is decreasing and the flow tends to be aligned with the guide vane. However, when the flow rate through the channel is decreasing, i.e in the stalling phase Fig. 6.4 c), a clear increase of the AOA
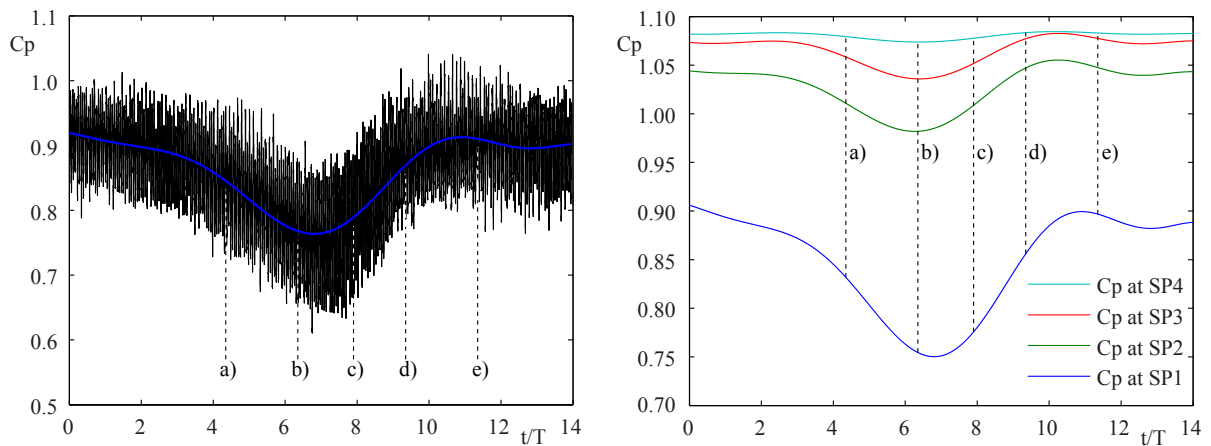
Figure 6.7: a) Time history of C_p located at SP1, represented by the black line. The blue line is an interpolation. b) Interpolations representing the time history of the pressure coefficient along a diffuser channel.
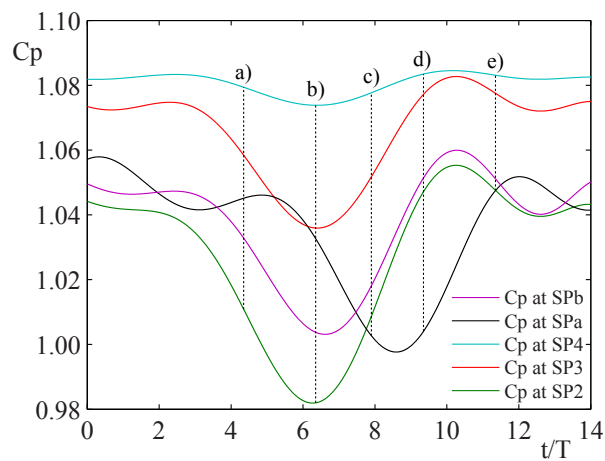

Figure 6.8: Time history of interpolated C_p in the area between the guide vane and the stay vanes.
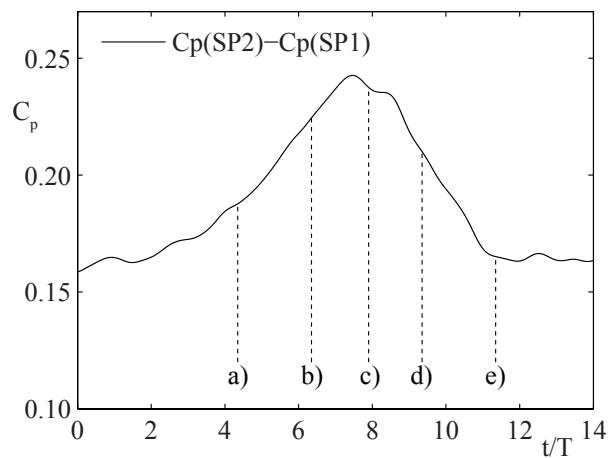

Figure 6.9: Difference of the pressure coefficient at SP1 and SP2.

is visible. This increase lasts during the entire phase of the decreasing flow rate (Fig. 6.4 b) to d)) and the maximum AOA is reached once the flow rate through the channel starts again to increase.

As mentioned above, the same trend is visible in Fig. 6.10 b), but with a forward temporal shift. Observing the relation between the AOA on GVB and the channel flow rate, some general comments can be made. First of all, the AOA reaches its minimum about 2 impeller revolutions before that on GVA reaches its minimum, which is consistent with the propagation speed of 2.4 impeller revolutions for the propagation of one stall cell from one diffuser channel to the downstream channel. The early increase of AOA (from a) to b)) does not impact on the flow passing through the channel as it is still increasing. However, we can see that the start of decrease in the flow rate can be associated with a high incident of the flow on GVB. Then, the maximum AOA (phase c) corresponds to the middle phase of the stalling process. Beyond that phase, the oncoming flow on GVB still has a high AOA, but is decreasing. Once the decrease is sufficient, i.e. the flow is almost aligned with the guide vane orientation, the flow rate into the channel starts to increase again.

Since it was shown that the orientation of the flow near the leading edge of the guide vane changes in a stall cycle, one can expect a variation of the flow orientation all along the pitch at the inlet of the guide vane channel. To confirm this, the evolutions of the radial component of the velocity on the cylindrical section at two different locations, see Fig. 5.2, are shown in Fig. 6.11. Furthermore, when the flow velocity in the clearance area is decomposed into its tangential and radial components, with respect to the cylindrical section, the main parameter determining the orientation of the flow is the radial component as the tangential component does not change significantly. Therefore, to avoid misunderstanding with the angle describing the AOA of the flow on the guide vane, the radial component is shown as it dictates the orientation of the flow.

As it can be expected, the evolution of the flow near the center of the pitch and near the leading edge of the suction side are different. Indeed, the orientation of the flow near the leading edge is mainly dictated by the physics taking place in the upstream channel, whereas the orientation of the flow in the center of the guide vane pitch is dictated by
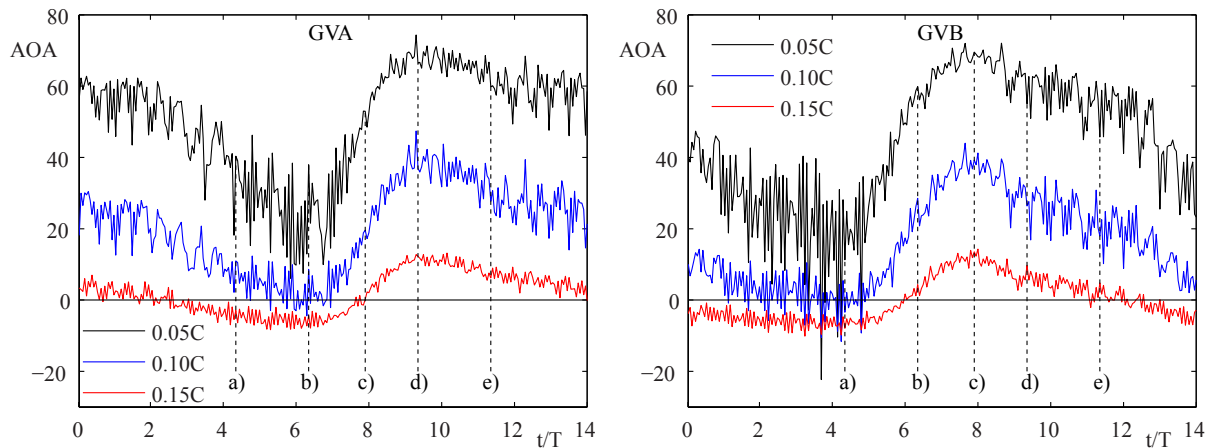

Figure 6.10: Evolution of the AOA on GVA and GVB for three locations: 5%, 10% and 15% of the guide vane chord length upstream of the leading edge.
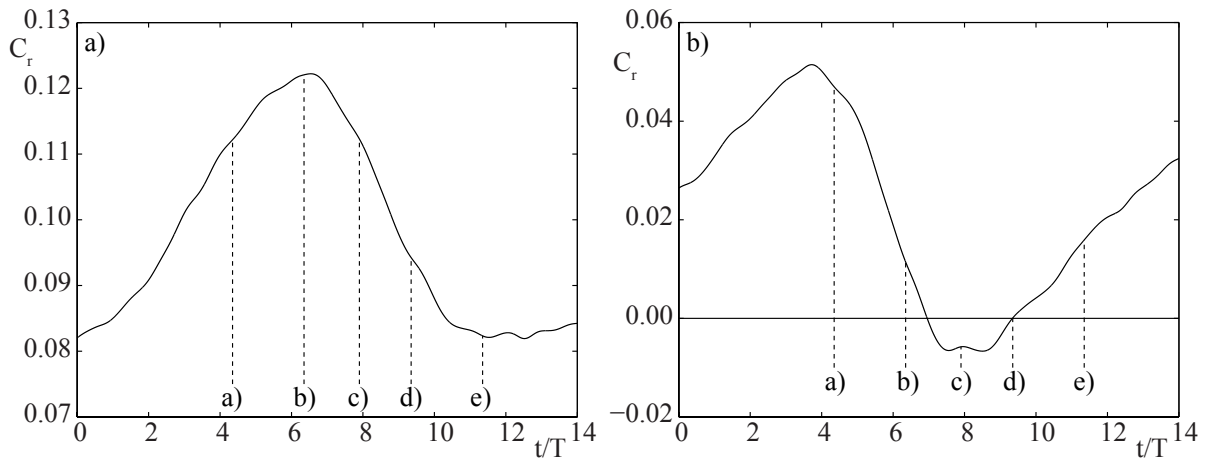
Figure 6.11: Evolution of the low-pass filtered radial component C_r at two locations, see Fig. 5.2 on page 55. a) pt22, b) pt37.

the physics taking place in the channel. It was already shown that the AOA of the flow incidence on GVA increases from the instant a) to c). Therefore, the corresponding change occurs for the flow near the leading edge, see Fig. 6.11 b). The deviation of the flow in the upstream channel is such that the radial component becomes negative, which means that the deviation induces a reverse flow near the leading edge. The consequences of this change are that the flow is not directed toward the radial direction as it is under normal condition and that the momentum of the flow near the suction side is decreasing. Regarding the center of the channel, no reverse flow is observed. However, the evolution is different as this area is mainly affected by the recirculation zone taking place in the channel. When the channel experiences high flow rate, the orientation of the flow is close to the orientation of the guide vane, which results in high radial velocity. However, since the flow near the leading edge on the suction side is more deviated and the recirculation zone grows, the flow at the center of the channel is more favorable to deviate toward the downstream channel resulting in the decrease of the radial velocity.

Stay Vane

Figure 6.12 also shows the evolution of the AOA, but for the corresponding stay vane. Furthermore, for comparison purposes, the distances from the leading edge are normalized using the guide vane chord length, hence the notation C_{GV}. As it can be seen, the flow incidence on the stay vanes undergoes a fast transition from negative incidences to positive ones and then reduces back to negative incidences. The main characteristic driving the incidence of the flow on the stay vane is the size of the wake generated by the guide vane and the recirculation region. In situations of high flow rates within the channel, only a small recirculation region is present and is located on both pressure side and suction side of the trailing edge of the guide vane. Therefore, it does not perturb the flow and the latter approaches the stay vane with negative incidence. However, since the stall cell is growing, the flow is deviated toward the guide vane pressure side and generate a large wake there. As it can be seen in Fig. 6.3 b) such a wake reaches the leading edge of the stay vane which explains such a fast transition. Furthermore, the maximum AOA is
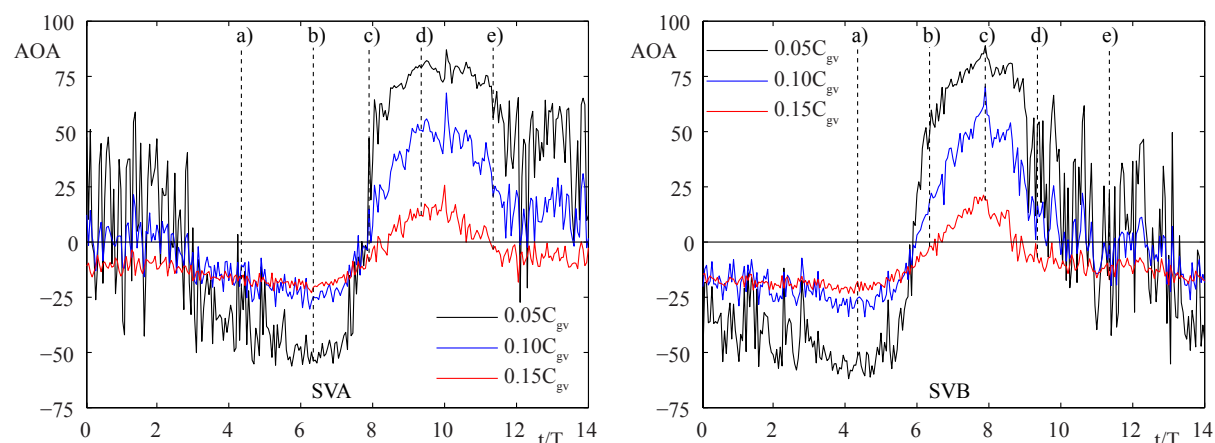
Figure 6.12: Evolution of the AOA on SVA and SVB for three locations: 5%, 10% and 15% of the guide vane chord length upstream of the leading edge.

reached when the diffuser channel is fully stalled. In that specific instance, the pressure in the stay vane channel reaches the high pressure of the volute, as previously explained in Fig. 6.8. Meanwhile, the pressure in the downstream neighboring diffuser channel has a lower pressure as the flow is near the nominal flow rate. Therefore, some part of the flow approaching the stay vane channel is deviated toward the gap formed be the guide vane trailing edge and the stay vane leading edge, see Fig. 6.3 c) and d). Such a deviation results in these very high AOA.

6.3.3   Summary of the Stall Cells Propagation Mechanism

Step 0 The flow rate within a channel is increasing and higher than the nominal flow rate, see instant a) in Fig. 6.4 f). Resulting from this increase, the pressure decreases within the channel (Fig. 6.7). However, because of the high velocity taking place in the clearance area, the pressure decrease is higher than downstream in the diffuser (Fig. 6.9). Therefore, the increase of flow rate contributes to the increase of the adverse pressure gradient within the guide vane channel.

Meanwhile, the flow near the leading edge on the upstream guide vane suction side starts to be deviated toward its downstream channel (Fig. 6.10 GVB). This deviation on the upstream channel modifies the orientation of the flow near the leading edge on the suction side of the guide vane (Fig. 6.11 b). The flow is less aligned with the guide vane and deviates toward the downstream channel.

Step 1 The deviation of the flow near the leading edge on the suction side becomes sufficiently large and the flow at the inlet of the channel all along the pitch is modified (Fig. 6.11 a). This instant corresponds to the instant with the highest flow rate (instant b). It results that the AOA on the downstream guide vane start to increase (Fig. 6.10 GVA) and that the flow rate passing through the channel starts to decrease (Fig. 6.4 f). However, since the flow velocity in the clearance is still high and that the flow rate decreases the pressure downstream the diffuser (SP2) increases, resulting in increasing further the pressure difference (Fig. 6.9). Furthermore, the combination of the decrease of the flow rate and the high pressure

gradient give favorable conditions for a growth of the recirculation area near the trailing edge on the suction side to start. Besides, because of the guide vanes geometry configuration, the shortest distance between the two guide vanes is from point x/C=2.2% on the downstream guide vane (GVA) pressure side and point x/C=84.9% on the upstream guide vane (GVB) suction side. Any, perturbation of the flow near the trailing edge of the upstream guide vane has therefore an impact on the flow near the upstream guide vane.

Step 2 The deviation taking place near the leading edge on the suction side reaches its maximum (Fig. 6.11 b) instant c). The flow rate through the channel reduced considerably and the adverse pressure gradient reached its maximum (Fig. 6.5 c) and Fig. 6.9). It results that the recirculation zone becomes more significant (Fig. 6.4 c). The flow within the channel is redirected to the downstream guide vane due to the recirculation zone.

Step 3 Since the conditions stay favorable, the recirculation zone grows and occupies almost all the guide vane pitch (Fig. 6.4 d), which blocks the flow and forces the flow to pass through the downstream channel, which results in high AOA on the downstream guide vane (Fig. 6.10). However, the deviation of the flow near the leading edge on the upstream guide vane suction side reduces (Fig. 6.11 b) and since that the flow velocity decreased the pressure difference decreases as well (Fig. 6.9). Therefore, the conditions are less favorable for the recirculations zone to maintain, i.e. the flow is less subject to separate and the size of the recirculation zone decreases.

6.4   Rotating Stall Impact

6.4.1   Impeller

The flow exiting the impeller is subject to changes imposed by the stalled channels. Furthermore, it was shown that the main variation of the pressure in the diffuser takes place in the clearance area, namely downstream of the impeller exit. Figure 6.13 a) shows the instantaneous pressure coefficient located on the impeller represented by the red curve for one impeller revolution. On the diffuser, the pressure at SP1 is monitored for each channel. Using such signals, the local pressure in the diffuser near a specific blade channel can be built. This results in the black line and it can be confirmed that the pressure at the impeller exit is similar to the pressure field in the stationary part. The amplitude and the phase agree well. Furthermore, with regards to the pressure field in the clearance, the interaction with some guide vanes are missing. Indeed, the diffuser is composed of 20 guide vanes, but the pressure signal on the impeller shows only 16 main oscillations. The fluctuation of the pressure in the impeller is slightly smaller than in the diffuser. The main frequency of the fluctuation is the first harmonic of the BPF and the amplitude is approximately 8%. But, since the impeller is rotating at a much faster speed compared to the propagation of the stall, there is no similar variation as the pressure drop seen in the diffuser. Finally, the presence of the stall cell confirms that the frequency of the RSI changes under rotating stall and therefore may affect or even worse damage the machine.

The evolution of the flow rate through a single impeller channel is shown in Fig. 6.13 b) for one impeller revolution. Since the instantaneous flow fields were saved at 100 time
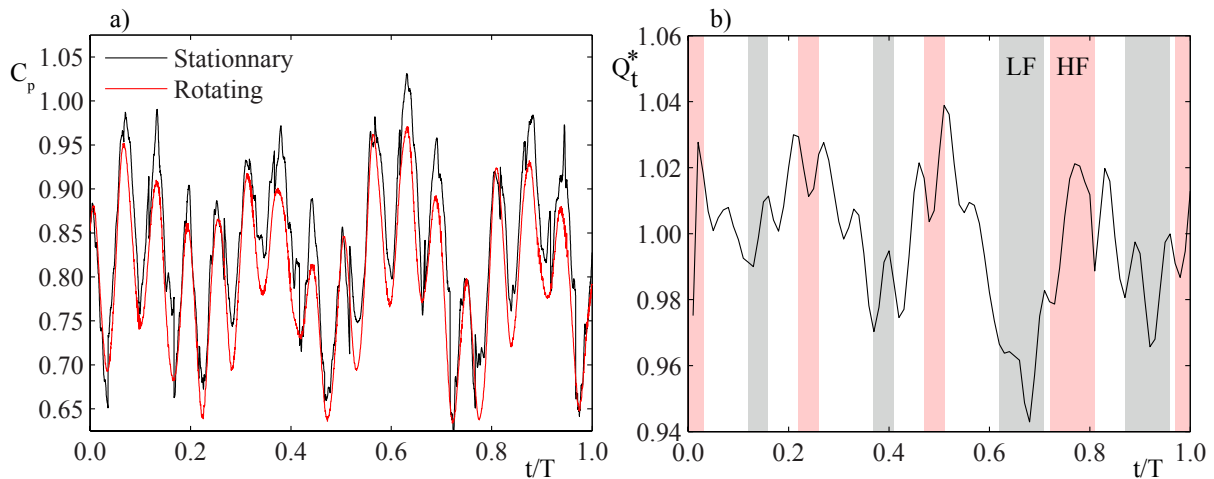
Figure 6.13: Comparison between the evolution of a quantity in the impeller for one impeller revolution with the corresponding quantity on the stationary part, i.e. the diffuser. a) pressure coefficient, b) flow rate (LF: Low Flow rate, HF: High Flow rate).

steps, which corresponds to the revolution of the impeller with 3.6 degrees, the above flow rate was also computed at every 3.6 degrees. Furthermore, the approximate duration when the impeller channel is close to a high/low flow rate guide vane channels is represented by the grey and pink strips. It can be seen that the flow rate in the impeller changes in accordance with the change occurring in the diffuser. However, the magnitude of the fluctuations is one order smaller compared that in the diffuser. Indeed, it was shown that the fluctuation in the diffuser are $\pm 60\%$, whereas in the impeller the fluctuation are $\pm 6\%$. Such difference can be explained by the fact that the flow within the impeller is very energetic and is driven by the mechanical rotation of the impeller. Therefore, the rotating stall only has relatively weak impacts on the flow within the impeller.

6.4.2   Guide Vane

It was shown that the presence of the stall cells modifies the pressure field and the velocity field. These changes induce a temporal and spatial local variation of the stress applied to different components of the machine. To elucidate this behavior, the evolution of a guide vane lift coefficient (black line) during 1/4 stall cycle, i.e. one passage of a stall cell, is depicted in Fig. 6.14 (a). The red line is the low-pass filtered lift coefficient. In the previous section, we see the close relation between the pressure field and the velocity field. It can then be expected that the lift of a guide vane is correlate with the flow rate passing through the channel surrounding the guide vane. Figure 6.14 (b) shows thus the instantaneous flow rates of the two channels (here upstream and downstream denote direction with regards to the impeller rotation), as well as their difference shown by the black line. It clearly shows that the high lift occurred when the upstream channel is in the stalling process. As soon as the downstream channel starts to stall, and thus the flow rate difference start to decrease, the lift coefficient starts to decrease accordingly. The lift coefficient changes by a factor of 3, when a stall cell is passing.

Figure 6.14: (a) Lift coefficient variation on a guide vane during one quarter stall cycle. The black line is the instantaneous lift coefficient and the red line the low-pass-filtered lift coefficient with a cutoff frequency set to f_n. (b) The green and the blue lines are respectively the normalized flow rate through the upstream and downstream channels. The black line is the flow rate difference between the two channels.

6.4.3   Stay Vanes

An identical approach was adopted for the effect of the stall cell on the stay vane load, see Fig. 6.15 (a). The low-pass filtered lift coefficient (red curve) is near zero. Furthermore, the instantaneous lift coefficient (black curve) periodically takes negative value, indicating that the stay vane pressure side is acting as a suction side and viceversa. As previously, it can be seen that the lift coefficient is function of the flow rate difference between the two channels surrounding a particular stay vane.

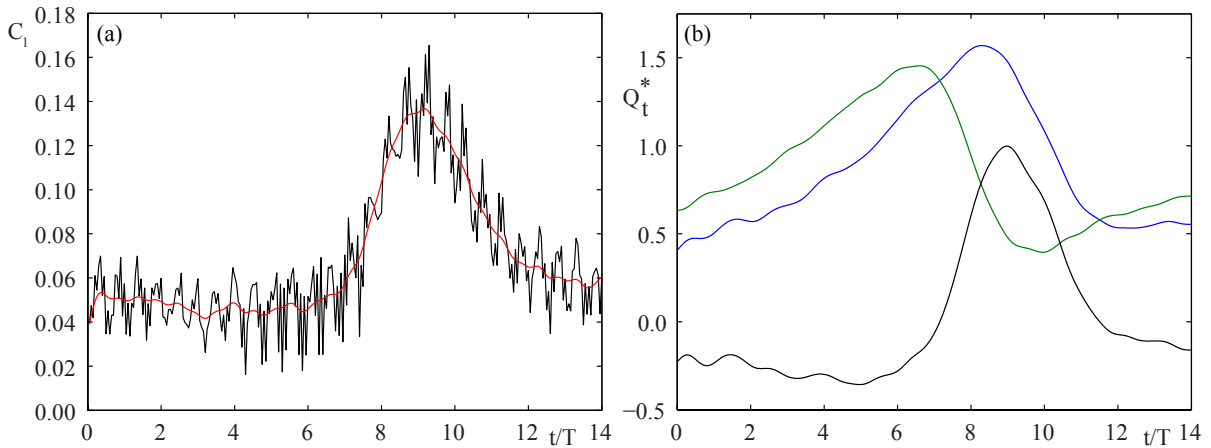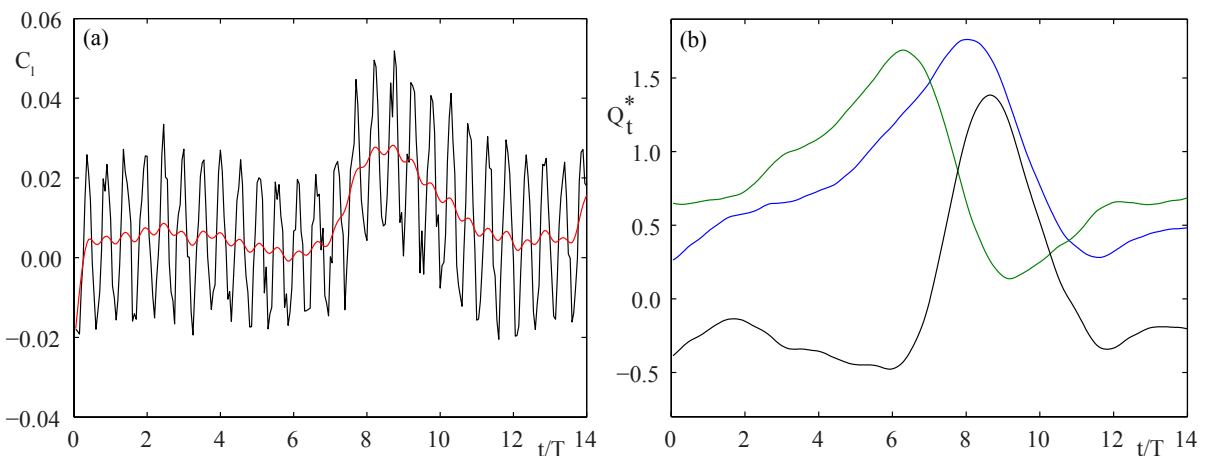Figure 6.15: (a) Lift coefficient variation on a stay vane during one quarter stall cycle. The black line is the instantaneous lift coefficient and the red line the low-pass-filtered lift coefficient with a cutoff frequency set to f_n. (b) The green and the blue lines are, respectively, the normalized flow rate through the upstream and downstream channels. The black line is the flow rate difference between the two channels.
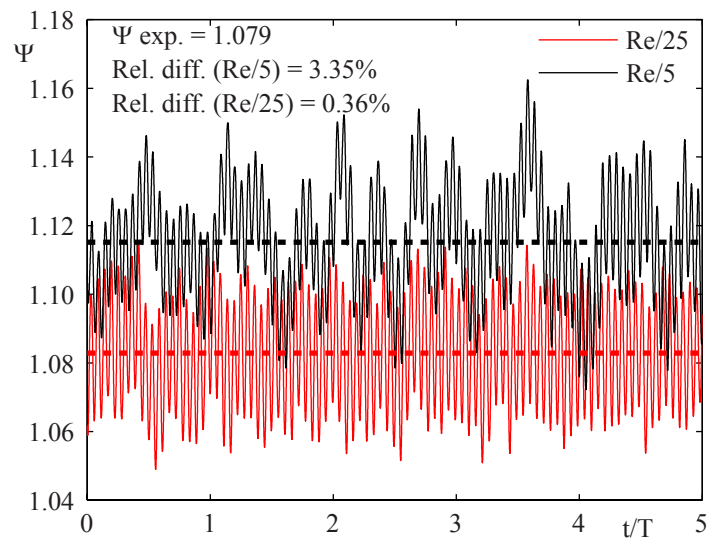
Figure 6.16: Comparison of the computed Head for the initial computation (Re/5) and the reduced Reynolds number computation (Re/25).

6.5   Grid Resolution Effect

Energy coefficient

The latest computation performed for a Reynolds number reduced by a factor 25 agrees well with the measurements. Therefore, the question regarding the grid resolution influence arises. To begin with, one can compare the specific energy coefficient Ψ computed. The computed energy coefficients during 5 impeller revolutions are shown in Fig. 6.16. There is no significant change, as already the specific energy coefficient computed in the initial computation is already close to the experiment with a relative difference of 3.35%. For the second computation, the relative difference drops to 0.36%, which fits precisely the experiment. Furthermore, the specific energy coefficient is a good measure to ensure that the appropriate recovery of the flow is achieved. In the initial computation, the flow is slightly too much decelerated compared to the experiment. However, such a variable does not provide any information regarding the physics taking place in the guide vane channels, but only assesses if the flow is first sufficiently accelerated and secondly sufficiently decelerated.

Flow rate through a guide vane channel

To evaluate the difference taking place in the diffuser, one can monitor, as previously introduced, the temporal evolution of the flow rate passing through each guide vane channels. An example of such an evolution is shown in Fig. 6.17. For each comparison between the initial and the second computation, the same guide vane channel is used. Such representations allow to confirm that a significant difference is taking place between the initial and the second computations. In Fig. 6.17 a), one can see that the flow rate passing through a guide vane channel in the case of the second computation (Re/25) experiences a entire passage of one stall cell. Regarding the Re/5 case, only the recovery
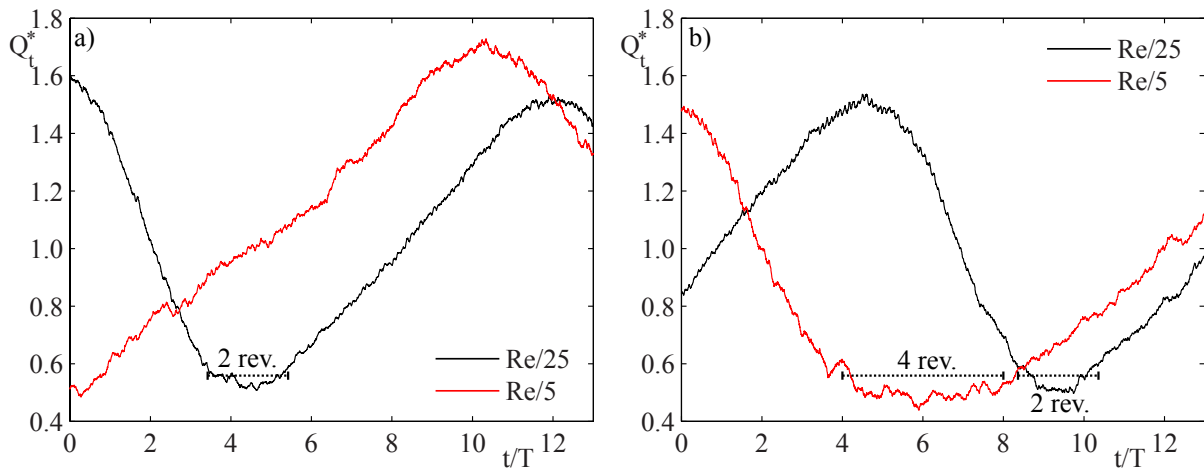
Figure 6.17: Comparison of the computed flow rate variation through the guide vane throat for the initial computation (Re/5) and the reduced Reynolds number computation (Re/25).

and the early phase of the stall are visible in the same duration. Fig. 6.17 b) shows the stalled phase experienced by another guide vane channel. From this observation, it can be concluded, that one of the main differences between the two computations and therefore responsible for the difference of propagation speed, is taking place during the stalled phase. Indeed, in the case of Re/5, a guide vane channel is in the stalled phase for more than 4 impeller revolutions, whereas for the Re/25 case this phase lasts less than 2 impeller revolutions.

The comparison between the rate of increase and decrease of the flow rate shows a difference but not as significant as for the stalled phase. The phase where the flow rate is maximal is similar for the two cases, but in the case of Re/5 the maximum flow rate is approximately $Q_t^*=1.7$. Finally, using the two graphs, one can estimate the number of impeller revolutions needed for one stall cell to propagate from one channel to the downstream channel. It requires approximately 20 impeller revolutions, which results in a propagation speed 60% slower for the Re/5 case.

Flow pattern at the throat section

The normal velocity in the downstream direction through the guide vane throat is shown in Fig. 6.18 at an instant when the channel experiences the minimum flow rate for the two different computations. It can be seen that a significant difference exists between the two computations. The pattern shown in Fig. 6.18 b) is obtained from the flow for a reduced Reynolds number as already introduced in Fig. 5.6 on page 59. For this computation, the reverse flow is mainly located near the hub on the suction side. Figure 6.18 a) represents the flow pattern obtained with the initial computation. It results in a better agreement with the experiment, as the reverse flow also occupies the whole pitch of the guide vane channel near the hub. Therefore, further computations of the initial calculation should be performed to identify the origin of the non-symmetry in the flow in a symmetrical diffuser.
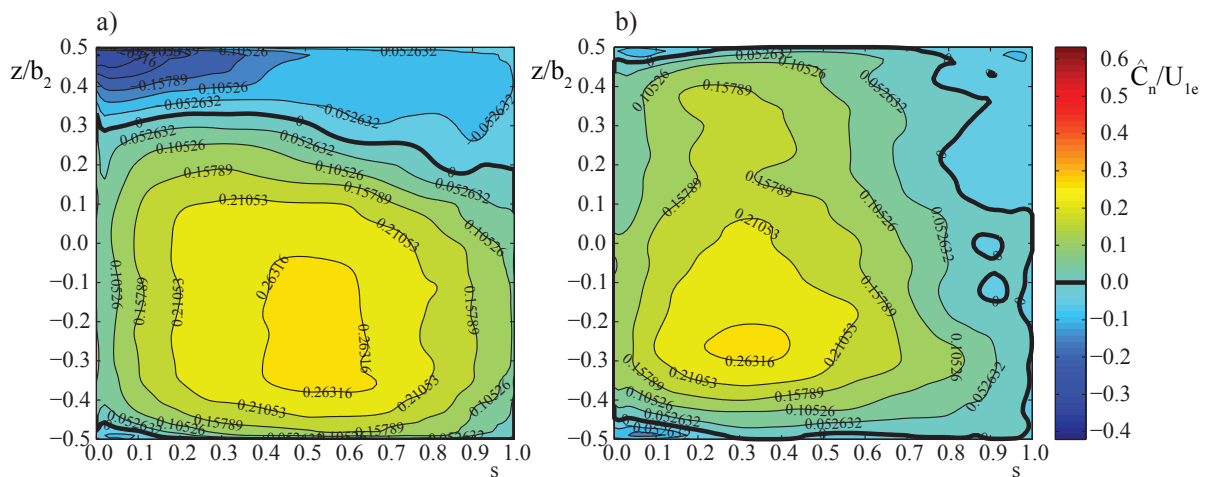
Figure 6.18: Comparison of the normal (streamwise direction) velocity in the guide vane throat section at the minimum flow rate: a) initial computation (Re/5), b) reduced Reynolds number computation (Re/25).

Kinetic Energy Spectrum

To estimate how the turbulence is capture by the computation, one can draw the kinetic energy spectra using the time history of the velocity at a specific location. The location selected is the one near the leading edge of the guide vane on the pressure side at the mid-span of the guide vane. The spectra obtained from the two computations are shown in Fig. 6.19 and three distinct ranges with a slope of -1, -5/3 and -7 can be seen. These ranges are, respectively, the production range, the inertial range and the dissipation range. The comparison of the two spectra does not show significant differences. However, in the case of the Re/5 computation, the inertial range is less pronounced than the Re/25 case and this could be attributed to a lack of dissipation. Because of the under-resolution of the flow the energy is not sufficiently dissipated and, therefore, get accumulated in the flow. However, such an estimation is only local and it is, therefore, difficult to draw a overall conclusion.

Flow pattern at the spanwise mid-plane of the diffuser

In Fig. 6.20 the velocity fields are shown in diffuser passages at maximum and minimum flow rates. At the maximum flow rate, the main difference is in the size of the recirculation zone. Both computations capture the recirculation, but in the case of the original calculation the size is smaller. It is worth mentioning that the flow rate is not identical, as the initial calculation has a 10 % higher flow rate. Furthermore, the distribution of the flow exiting the guide vane channel is different. From there, the flow can exit the machine through the stay vane channel or through the gap between the trailing edge of the guide vane and the leading edge of the stay vane. In standard operation of the pump, the distribution is near 50%. But in the case of the initial computation the flow is less likely to exit via the gap and most of the flow exiting the guide vane channel goes to the stay vane channel. The flow rate in the gap can decrease until a flow rate of
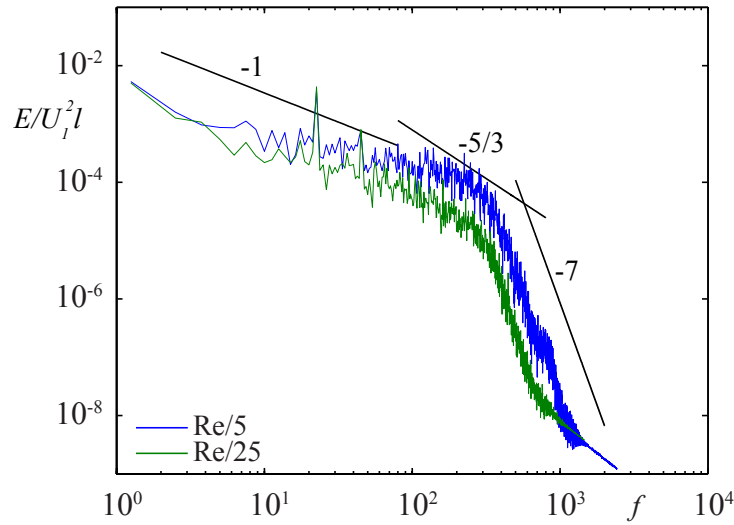
Figure 6.19: Comparison of the kinetic energy spectrum near the pressure side and the leading edge of the guide vane at the mid-spanwise.

$0.2Q_o$.

The situation where the channel is at its lowest flow rate shows that in both computations the minimum is reached when the stall cell occupies near the entire pitch of the guide vane channel. However, the distance from the trailing edge to the separation point is nearly the same. At that instant, it can be seen that the size of the recirculation zone on the downstream channel differs. Indeed, the size for the reduced Reynolds number computation is already bigger and, therefore, it modifies the flow in its vicinity. This confirms that the rate of growth of a stall cell determines the propagation speed of the stall cell.

6.6   Discussion

In this chapter, it was shown that the propagation mechanism of the rotating stall may be regarded as the local growth and decay of a stall cell. The rate of fluctuation of the stall cell governs the propagation speed. The growth of the stall cell reduces firstly the flow rate passing through the guide vane channel and almost blocks the channel when the stall cell reaches its maximum size, i.e. when it reaches the leading edge of the downstream guide vane. The growth and decay are governed by the variation of the adverse pressure gradient between the leading and the trailing edges of the guide vane and by the deviation of the flow near the leading edge of a guide vane. Furthermore, as the recirculation is located in a narrowed area, it induces a modification of the flow as soon as the recirculation zone grows. Therefore, any changes in the size of the recirculation zone change the flow pattern near the leading edge of the downstream guide vane. These changes are responsible for the switch between the favorable and the unfavorable conditions for a recirculation zone to grow. A schematic of the flow patterns in a guide vane channel is shown in Fig. 6.21.
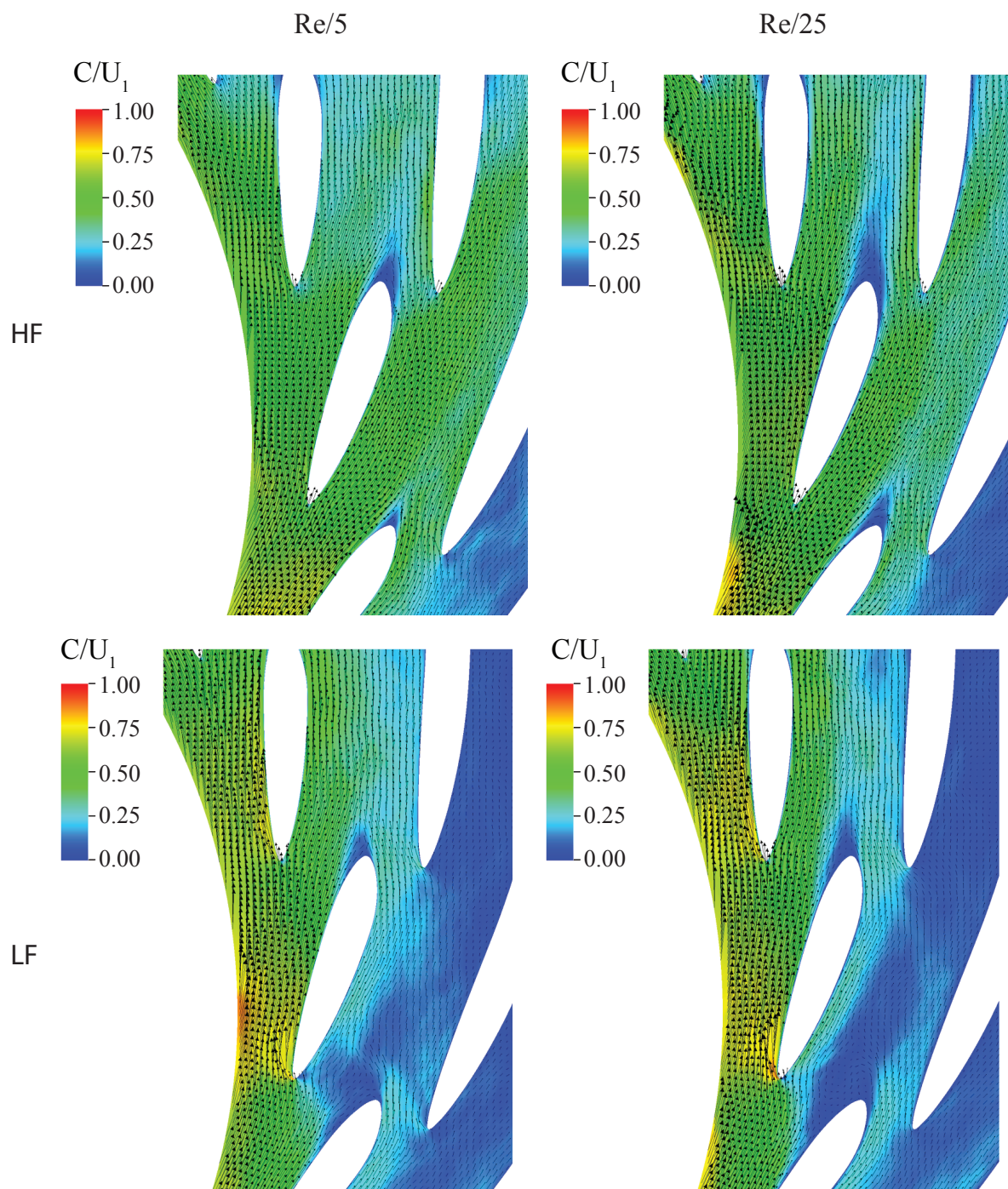
Figure 6.20: Comparison of the computed flow fields in the guide vane channels at maximum (HF) and minimum (LF) flow rate for the initial computation (Re/5) and the reduced Reynolds number computation (Re/25).
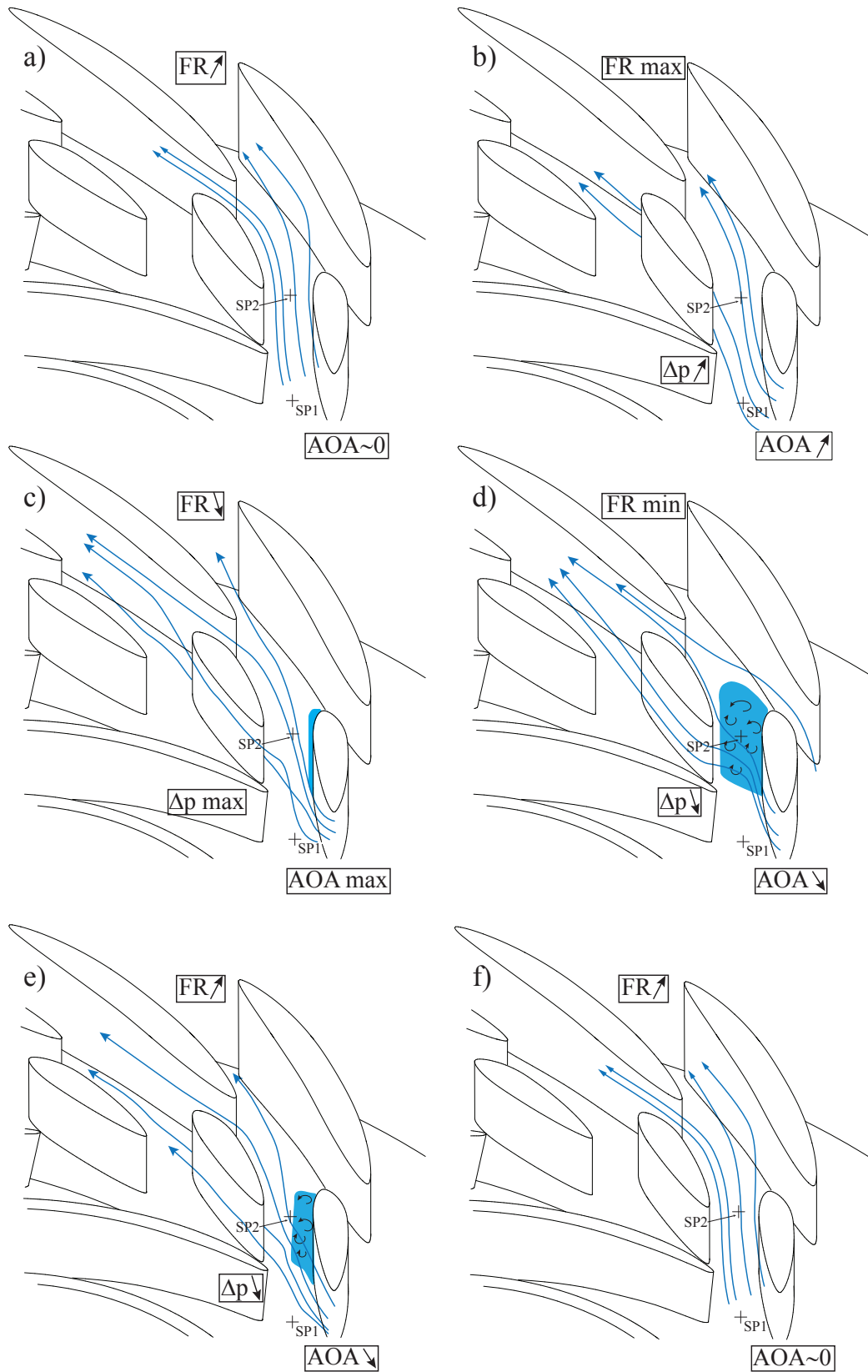
Figure 6.21: Schematic of the variation of the flow within a guide vane channel.

Part IV

Conclusions and Perspectives

Chapter 7

Conclusions and Perspectives

7.1 Conclusions

A large scale computation of the rotating stall phenomenon was performed for the first time using the Large Eddy Simulation technique. The case study selected is the reduced scale model HYDRODYNA pump-turbine operating at part load condition (76% BEP) in pumping mode. The computations were performed using the open source software FrontFlow/Blue and the PRIMEHPC FX10 supercomputer of the University of Tokyo. To ensure the viability of this investigation, a feasibility study was performed beforehand. It was concluded that, with the computing power currently available, such an investigation is feasible if the Reynolds number is reduced. If the reduction is by a factor 5 (Re/5) regarding the experiment, the required mesh features 7 billions of elements. If it is further reduced by a factor 5 (Re/25) the size of the required mesh reduced to 80 millions elements.

However, the flow initialization performed for the Re/5 case with a mesh composed of 85 million elements showed that the unsteady rotating stall phenomenon is already well captured. Four distinct zones, i.e. four guide vane channels experiencing high outward flows compared to the others, showed the presence of the instability. The estimation of the propagation speed of the stall cells was done by monitoring the instantaneous pressure in the clearance area between the impeller exit and the guide vane leading edge and by monitoring the flow rate through the guide vane channels. The results showed a propagation in the same direction as the impeller, where the propagation speed is approximately 60% slower than the measured value on the reduced scale model. Such a difference is associated to the grid resolution as a mesh of 7 billions elements is required to compute such a Reynolds number.

The simulation for the second Reynolds number reduction (Re/25) produced an accurate and satisfactory outcome. The number of stall cells was correctly captured and the propagation speed was only 3.4% slower than the measured value, compared to the 60% in the initial computation. Furthermore, with the difference of 0.36% regarding the measurements, the computed specific energy coefficient Ψ showed a better agreement than in the initial computation (3.35% difference). It is concluded that the LES approach is a powerful tool, where the traditional RANS approach reached its limit. Indeed, former studies indicated that the rotating stall is not accurately captured by a RANS computation with the $k - \omega$ SST model. For this investigation, the flow rate had to be increased by 23% in order to observe the presence of the stall cells. Furthermore, for this higher flow rate, the

computed propagation speed was 38% faster compared to the experiment. Despite the good agreement of the LES results with the measurement data at Re/25, the following inconsistencies are observed. The flow patterns in the diffuser displayed substantial differences with respect to the experiment; the size and the recirculation area were not well represented in the computation. On the other hand, the evolution of the flow rate within the guide-vane channels agrees well with the measurements. Therefore, the rotating stall phenomenon was globally well captured and the calculation could, therefore, be used for further investigations.

This analysis showed that the stall mechanism is driven by the growth and the decay of the stall cell. Furthermore, it was shown that both the rate of growth and the rate of decay are almost constant, where the rate of growth is higher than the rate of decay. The stall cell is located at the guide vane trailing edge on the suction side. As soon as it starts growing, the flow within the guide vane channel is deviated toward the downstream channel. The growth of the stall cell is such that at its maximum volume, the stall size occupies the entire guide vane pitch. However, the orientation of the flow at the guide vane inlet and the decrease of the adverse pressure gradient result in the impossibility for such a cell to sustain. The cell size decreases until the favorable conditions for flow recirculation are met again.

7.2 Perspectives

The recent development of computing power paves the way for the LES approach towards industrial applications. However, in the study, the proper mesh size is only reached through a reduction of the Reynolds number. However, on the way of the LES approach to become an industrial standard, further development is required. First of all, this approach depends upon a dense, high quality mesh in order to guarantee the stability and the accuracy of the results. This makes the mesh generation very time consuming. An existing alternative is the SPH method, which does not require a mesh generation but suffers from its high demand in CPUs. Therefore, a promising development in the future is the automatic grid generation. First step relies on a coarse Cartesian grid, which divides each cell into 4 or 8 sub-cells, depending on the 2D or 3D nature of the problem, for a better discretization of the geometry or a region with high gradient of the flow variables. This mesh is known as voxel mesh and the success of this approach would be a decisive breakthrough for the LES to be used as a standard tool in the industries.

Another issue combines both the computing resources and the storage capacity. To perform large-scale LES computations, the traditional local clusters accommodated by the industry to the present day are by far too small. These clusters consist of a few hundreds cores at maximum, whereas one to three order of magnitude more is be required. Therefore, specific HPC centers have to be built and dedicated to industrial and academic research. Such centers already exist and opened recently to the industry. Two examples are the K computer (RIKEN) in Japan and the Vulcan supercomputer (LLNL) in the USA, both being accessible to the industry and possessing two petaflops scale computing power. The industrial LES perspectives are thus encouraging. A further issue which remains to be solved concerns the data storage and the transport. A small LES computation features one million to 10 million grid points. Therefore, the data volume from the computation reaches easily the size of tera Bytes (TB). The present network capabilities may be used

to manage data of the size of a few GB. If the volume reaches a few TB, a portable hard disk drive may still be used. Above 4 TB, which is today the largest portable hard disk, it becomes increasingly complicated to move the data. Therefore, the analysis has to be done on-site of the HPC center, which is possible but for a limited amount of time.

Finally, further investigations should be performed to identify the reason for the two different propagation speeds resulting from the two computations. The reason probably lies within the computation of the boundary layer development. Finally, it would be interesting to evaluate the behavior of boundary layer for a fluctuating flow rate in both computations.

Bibliography

Bibliography

[1] ARNDT, N., ACOSTA, A. J., BRENNEN, C., AND CAUGHEY, T. K. Experimental investigation of rotor-stator interaction in a centrifugal pump with several vaned diffusers. *Journal of Turbomachinery 112*, 1 (1990), 98–108.

[2] ARNDT, N., ACOSTA, A. J., BRENNEN, C. E., AND CAUGHEY, T. K. Rotor-stator interaction in a diffuser pump. *Journal of Turbomachinery 111* (1988), 213–221.

[3] BRAUN, O. *Part Load Flow in Radial Centrifugal Pumps*. PhD thesis, EPFL, 2009.

[4] BYSKOV, R. K., JACOBSEN, C. B., AND PEDERSEN, N. Flow in a Centrifugal Pump Impeller at Design and Off-Design Conditions—Part II: Large Eddy Simulations. *Journal of Fluids Engineering 125*, 1 (Jan. 2003), 73–83.

[5] CHAPMAN, D. K. Computational aerodynamics development and outlook. *AIAA journal 17*, 12 (1979), 1293–1313.

[6] CHOI, H., AND MOIN, P. Grid-point requirements for large eddy simulation: Chapman's estimates revisited. *Physics of Fluids 24*, 1 (2012), 011702.

[7] CLARK, R. A., FERZIGER, J. H., AND REYNOLDS, W. C. Evaluation of subgrid-scale models using an accurately simulated turbulent flow. *Journal of Fluid Mechanics 91*, 01 (1979), 1–16.

[8] DA SILVA, C., AND MÉTAIS, O. On the influence of coherent structures upon interscale interactions in turbulent plane jets. *Journal of Fluid Mechanics 473*, 1 (2002), 103–145.

[9] DE JAGER, B. Rotating stall and surge control: A survey. In *34th IEEE Conference on Decision and Control* (1995), vol. 2, IEEE, pp. 1857–1862.

[10] DEARDORFF, J. A numerical study of three-dimensional turbulent channel flow at large Reynolds numbers. *Journal of Fluid Mechanics 41*, 2 (1970), 453–480.

[11] DENNARD, R., AND GAENSSLEN, F. Design of ion-implanted MOSFET's with very small physical dimensions. *IEEE Journal of Solid-State Circuits 9*, 5 (1974), 256–268.

[12] DESAI, D. M., BRADICICH, T. M., CHAMPION, D., HOLLAND, W. G., AND KREUZ, B. M. BladeCenter system overview. *IBM Journal of Research and Development 49*, 6 (2005), 809–821.

[13] DONGARRA, J. The LINPACK benchmark: past, present and future. *Concurrency and Computation: practice and experience 15*, 9 (2003), 803–820.

[14] EMMONS, H. W. A survey of stall propagation: experiment and theory. *Journal of Basic Engineering 81* (1959), 409–416.

[15] FUJITSU. A new Generation 16-core Processor for Supercomputing SPARC64 IXfx. 2011.

[16] GERMANO, M., PIOMELLI, U., AND MOIN, P. A dynamic subgrid-scale eddy viscosity model. *Physics of Fluids 3*, 7 (1991), 1760–1765.

[17] GROPP, W., LUSK, E., AND SKJELLUM, A. *Using MPI: portable parallel programming with the message-passing interface.* the MIT Press, 1999.

[18] GU, G., SPARKS, A., AND BANDA, S. S. An overview of rotating stall and surge control for axial flow compressors. *IEEE Transactions on Control Systems Technology 7*, 6 (1999), 639–647.

[19] GUO, Y., KATO, C., WANG, H., AND YAMADE, Y. A Fractional-Step Large-Eddy Simulation Method in Overset Finite-Element Mesh and Its Application to Turbomachinery. *Nihon Kikai Gakkai Ryutai Kogaku Bumon Koenkai Koen Ronbunshu (CD-ROM) 82* (2004), 120–123.

[20] HASMATUCHI, V., FARHAT, M., AND AVELLAN, F. *Hydrodynamics of a Pump-Turbine Operating at Off-Design Conditions in Generating Mode.* PhD thesis, EPFL, 2012.

[21] HUNT, J. C., AND MORRISON, J. F. Eddy structure in turbulent boundary layers. *European Journal of Mechanics - B/Fluids 19*, 5 (2000), 673–694.

[22] IBM BLUE GENE TEAM. Overview of the IBM Blue Gene/P project. *IBM Journal of Research and Development 52*, 1.2 (2008), 199–220.

[23] INOUE, M., AND CUMPSTY, N. A. Experimental study of centrifugal impeller discharge flow in vaneless and vaned diffusers. *Journal of engineering for power 106*, 2 (1984), 455–467.

[24] JONES, W., AND LAUNDER, B. The prediction of laminarization with a two-equation model of turbulence. *International Journal of Heat and Mass Transfer 15*, 2 (Feb. 1972), 301–314.

[25] KARYPIS, G., AND KUMAR, V. A parallel algorithm for multilevel graph partitioning and sparse matrix ordering. *Journal of Parallel and Distributed Computing 48*, 1 (1998), 71–95.

[26] KATO, C., KAIHO, M., AND MANABE, A. An Overset Finite-Element Large-Eddy Simulation Method With Applications to Turbomachinery and Aeroacoustics. *Journal of Applied Mechanics 70*, 1 (2003), 32–43.

[27] KATO, C., MUKAI, H., AND MANABE, A. Large-eddy simulation of unsteady flow in a mixed-flow pump. *International Journal of Rotating Machinery 9*, 5 (2003), 345–351.

[28] KERR, R., DOMARADZKI, J., AND BARBIER, G. Small-scale properties of nonlinear interactions and subgrid-scale energy transfer in isotropic turbulence. *Physics of Fluids 8*, 1 (1996), 197–208.

[29] KLINE, S. On the nature of stall. *Journal of Basic Engineering 81*, 3 (1959), 305–320.

[30] KLINE, S. J., REYNOLDS, W. C., SCHRAUB, F. A., AND RUNSTADLER, P. W. The structure of turbulent boundary layers. *Journal of Fluid Mechanics 30*, 04 (1967), 741–773.

[31] KOLMOGOROV, A. N. The local structure of turbulence in incompressible viscous fluid for very large Reynolds number. *Dokl. Akad. Nauk SSSR 30*, 4 (1941), 301–305.

[32] KOSEFF, J. R., AND STREET, R. L. The Lid-Driven Cavity Flow: A Synthesis of Qualitative and Quantitative Observations. *Journal of Fluids Engineering 106*, 4 (1984), 390–398.

[33] KRAIN, H. A study on centrifugal impeller and diffuser flow. *Journal of Engineering Power 103* (1981), 688–697.

[34] KRAUSE, N., ZÄHRINGER, K., AND PAP, E. Time-resolved particle imaging velocimetry for the investigation of rotating stall in a radial pump. *Experiments in Fluids 39*, 2 (2005), 192–201.

[35] LAUNDER, B., AND SHARMA, B. Application of the energy-dissipation model of turbulence to the calculation of flow near a spinning disc. *Letters in Heat and Mass Transfer 1*, 2 (1974), 131–137.

[36] LESIEUR, M., AND METAIS, O. New trends in large-eddy simulations of turbulence. *Annual Review of Fluid Mechanics 28* (1996), 45–82.

[37] LILLY, D. A proposed modification of the Germano subgrid-scale closure method. *Physics of Fluids 4*, 3 (1992), 633–635.

[38] LUCIUS, A., AND BRENNER, G. Unsteady cfd simulations of a pump in part load conditions using scale-adaptive simulation. *International Journal of Heat and Fluid Flow 31*, 6 (2010), 1113–1118.

[39] MENEVEAU, C. Statistics of turbulence subgrid-scale stresses: Necessary conditions and experimental tests. *Physics of Fluids 6*, 2 (1994), 815–833.

[40] MENTER, F. R. Zonal Two Equation k-ω Turbulence Models for Aerodynamic Flows. *AIAA Paper 1993-2906* (1993).

[41] MENTER, F. R. Two-Equation Eddy-Viscosity Turbulence Models for Engineering Applications. *AIAA Journal 32*, 8 (1994), 1598–1605.

[42] MOORE, G. Cramming more components onto integrated circuits.

[43] MOORE, G. Progress in Digital Integrated Electronics. *IEEE Int. Electron Devices Meeting Tech. Dig. 21* (1975), 11–13.

[44] O'NEIL, J., AND MENEVEAU, C. Subgrid-scale stresses and their modelling in a turbulent plane wake. *Journal of Fluid Mechanics 349* (1997), 253–293.

[45] PEDERSEN, N., LARSEN, P. S., AND JACOBSEN, C. B. Flow in a Centrifugal Pump Impeller at Design and Off-Design Conditions—Part I: Particle Image Velocimetry (PIV) and Laser Doppler Velocimetry (LDV) Measurements. *Journal of Fluids Engineering 125*, 1 (Jan. 2003), 61–72.

[46] PIOMELLI, U., AND BALARAS, E. Wall-layer models for large-eddy simulations. *Annual review of fluid mechanics 34*, 1 (2002), 349–374.

[47] POPE, S. B. *Turbulent Flows.* Cambridge university press, 2000.

[48] ROBINSON, S. Coherent motions in the turbulent boundary layer. *Annual Review of Fluid Mechanics 23*, 1 (1991), 601–639.

[49] ROTH, S., FARHAT, M., AND AVELLAN, F. *Fluid-Structure Coupling Effects on the Dynamic Response of Pump-Turbine Guide Vanes.* PhD thesis, EPFL, 2012.

[50] SAGAUT, P. *Large Eddy Simulation for Incompressible Flows: An Introduction.* Springer, 2006.

[51] SANO, T., AND NAKAMURA, Y. Alternate blade stall and rotating stall in a vaned diffuser. *JSME International Journal Series B 45*, 4 (2002), 810–819.

[52] SANO, T., YOSHIDA, Y., TSUJIMOTO, Y., NAKAMURA, Y., AND MATSUSHIMA, T. Numerical Study of Rotating Stall in a Pump Vaned Diffuser. *Journal of Fluids Engineering 124*, 2 (June 2002), 363–370.

[53] SCHLICHTING, H., AND KESTIN, J. *Boundary-layer theory.* McGraw-Hill New York, 1968.

[54] SINHA, M., AND KATZ, J. The onset and development of rotating stall within a centrifugal pump with a vaned diffuser. *Paper FEDSM99-7314, The 3rd ASME/JSME Joint Fluid Engineering Conference* (1999), 1–7.

[55] SINHA, M., AND KATZ, J. Quantitative Visualization of the Flow in a Centrifugal Pump With Diffuser Vanes—I: On Flow Structures and Turbulence. *Journal of Fluids Engineering 122*, 1 (Mar. 2000), 97–107.

[56] SINHA, M., PINARBASI, A., AND KATZ, J. The Flow Structure During Onset and Developed States of Rotating Stall Within a Vaned Diffuser of a Centrifugal Pump. *Journal of Fluids Engineering 123*, 3 (Sept. 2001), 490–499.

[57] SMAGORINSKY, J. General circulation experiments with the primitive equations. *Monthly weather review 91*, 3 (1963), 99–164.

[58] TAMURA, A., KIKUCHI, K., AND TAKAHASHI, T. Residual cutting method for elliptic boundary value problems. *Journal of Computational Physics 137*, 2 (1997), 247–264.

[59] TORBERGSEN, E. A. *Impeller/Diffuser Interaction forces in Centrifugal Pumps.* PhD thesis, Norwegian University of Science and Technology, 1998.

[60] UZUN, A., BLAISDELL, G., AND LYRINTZIS, A. Sensitivity to the Smagorinsky constant in turbulent jet simulations. *AIAA journal 41*, 10 (2003), 2077–2079.

[61] VAN DER VORST, H. A. Bi-CGSTAB: A fast and smoothly converging variant of Bi-CG for solution of non-symmetric linear systems. *SIAM J. Sci. Stat. Comput. 13*, 2 (1992), 631–644.

[62] WILCOX, D. C. Reassessment of the scale-determining equation for advanced turbulence models. *AIAA Journal 26*, 11 (1988), 1299–1310.

[63] WILCOX, D. C. *Turbulence modeling for CFD*, vol. 3. DCW industries La Canada, 2006.

[64] WUIBAUT, G., DUPONT, P., CAIGNAERT, G., AND STANISLAS, M. PIV measurements in the impeller and the vaneless diffuser of a radial flow pump in design and off-design operating conditions. *Journal of Fluids Engineering 124*, 3 (2002), 791–797.

[65] ZANG, Y., AND STREET, R. L. A composite multigrid method for calculating unsteady incompressible flows in geometrically complex domains. *International Journal for Numerical Methods in Fluids 20*, 5 (1995), 341–361.

[66] ZOBEIRI, A., AND AVELLAN, F. *Investigations of time dependent flow phenomena in a turbine and a pump-turbine of Francis type: rotor-stator interactions and precessing vortex rope.* PhD thesis, EPFL, 2009.

Biography

Olivier PACOT

LMH - EPFL
Av. de Cour, 33 bis
CH-1007 Lausanne (VD)

Tél. prof.:	+41 21 693 2563	
Portable:	+41 78 681 3526	Né le 22 janvier 1983
E-mail prof.:	olivier.pacot@a3.epfl.ch	Nationalité franco-suisse
E-mail privé:	olivier.pacot@infomaniak.ch	Célibataire

FORMATION

2010-2014:	**Doctorat ès sciences techniques**
	École polytechnique fédérale de Lausanne (EPFL), Suisse
2003-2009:	**Dipl.-Ing. Mécanicien**
	École polytechnique fédérale de Lausanne (EPFL), Suisse
1998-2003:	**Collège Madame de Staël, Suisse**
	Maturité fédérale

EXPÉRIENCES

2009-2014:	**École polytechnique fédérale de Lausanne (EPFL), Suisse.**
	Assistant doctorant au Laboratoire de Machines Hydrauliques
2012-2014:	**The University of Tokyo, Japon.**
	Visiting Researcher Associate
2007:	**Bobst SA, Roseland NJ, USA**
	Stage de 3 mois
	Création d'une base de données répertoriant tout essai sur machine
	Elaboration d'un protocol pour test de performance
	Test d'un matériau démagnétisant les feuilles plastiques

COMPÉTENCES INFORMATIQUES

Systèmes:	Windows, Linux.
Program.:	C, C++, Fortran, Python, Shell, MATLAB, Labview
CFD:	FFB, CFX, Fluent, ICEM, OpenFoam, VisIt, Paraview.
Bureautique:	MS-Office, LaTeX.
Multimédia:	Adobe Illustrator

BREVETS

Ski:	Instructeur suisse
Aviation (PPL):	En cours
Parapente:	En cours

SPORTS & LOISIRS

Sports:	Kitesurf, Parapente, Télémark, Volley, aviron.
Loisirs:	Lecture, Cuisine, Aviation.

LANGUES

Français	Langue maternelle.
Allemand	Intermédiaire.
Anglais	Avancé.